

PARAMETRIC CONTINUOUS CRACK TIP  
BOUNDARY ELEMENTS IN LINEAR  
ELASTIC FRACTURE MECHANICS

By

HAROLD GRAYSON WALTERS

Bachelor of Science in Mechanical Engineering  
Louisiana State University  
Baton Rouge, Louisiana  
1984

Master of Science in Mechanical Engineering  
Louisiana State University  
Baton Rouge, Louisiana  
1986

Submitted to the Faculty of the Graduate College  
of the Oklahoma State University  
in partial fulfillment of the requirements  
for the Degree of  
DOCTOR OF PHILOSOPHY  
May, 1990

thesis  
1990D  
W235p  
cop. 2

COPYRIGHT

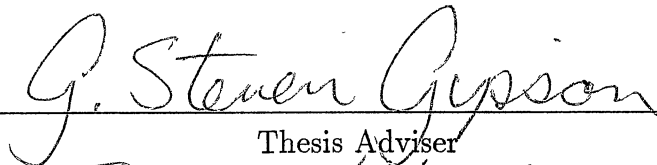
by

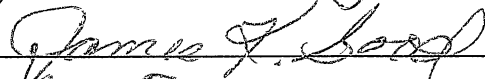
Harold Grayson Walters

May, 1990


PARAMETRIC CONTINUOUS CRACK TIP  
BOUNDARY ELEMENTS IN LINEAR  
ELASTIC FRACTURE MECHANICS

Thesis Approved:

  
\_\_\_\_\_  
Thesis Adviser

  
\_\_\_\_\_

  
\_\_\_\_\_

  
\_\_\_\_\_

  
\_\_\_\_\_

Dean of the Graduate College

## ACKNOWLEDGMENTS

The author would like to express his appreciation to his major professor, Dr. G. Steven Gipson, and his graduate committee members, Dr. Rex C. Donahey, Dr. Allen E. Kelly, and Dr. James K. Good. Financial support at various times during the author's Ph.D. program was provided by the U.S.A.E. Waterways Experiment Station at Vicksburg, Mississippi, and the School of Civil Engineering and the College of Engineering, Architecture and Technology at Oklahoma State University. Thanks also to Juan C. Ortiz and Charles V. Camp for their comradeship during his graduate school career and to Ms. Charlene Fries for her proofreading this manuscript.

This work is dedicated to my wife, Leigh Beaulieu Walters, my parents, Patricia Ann and Harold Leon Walters, and my dog, Carlye, for their love and understanding over the years.

# TABLE OF CONTENTS

Chapter	Page
<b>I. INTRODUCTION . . . . .</b>	<b>1</b>
<b>II. LITERATURE REVIEW . . . . .</b>	<b>3</b>
Numerical Methods in Linear Elastic Fracture Mechanics . . . . .	3
Evaluation of Stress Intensity Factors . . . . .	5
Crack Tip Elements . . . . .	6
<b>III. BOUNDARY ELEMENT FORMULATION FOR LINEAR ELASTIC FRACTURE MECHANICS . . . . .</b>	<b>9</b>
Linear Elastostatics . . . . .	9
Fundamental Solutions . . . . .	12
Boundary Integral Formulation . . . . .	14
Boundary Discretization . . . . .	17
Subregions . . . . .	18
Linear Elastic Fracture Mechanics . . . . .	19
Two Dimensional LEFM . . . . .	20
Three Dimensional LEFM . . . . .	22
<b>IV. TWO DIMENSIONAL BOUNDARY ELEMENTS . . . . .</b>	<b>24</b>
Derivation . . . . .	25
Linear (LINE) Element . . . . .	26
Quadratic (QUAD) Element . . . . .	28
Cubic (CUBIC) Element . . . . .	29
Overhauser (OVER) Element . . . . .	31
Right Corner Overhauser (OVR) Element . . . . .	38
Left Corner Overhauser (OVL) Element . . . . .	42
Integration . . . . .	44
Singular Integration . . . . .	46

<b>V.</b>	<b>TWO DIMENSIONAL CRACK TIP BOUNDARY ELEMENTS</b>	<b>51</b>
	Quadratic Quarter Point Crack Tip (CTQQ) Element	52
	Quadratic Traction Singular Quarter Point Crack Tip (CTQT) Element	53
	Quadratic Crack Tip (CTQUA) Element	55
	Overhauser Crack Tip (CTOVR) Element	59
	Integration	66
	Singular Integration	67
	Stress Intensity Factor Calculation	73
	Displacement SIF	73
	Traction SIF	75
<b>VI.</b>	<b>THREE DIMENSIONAL BOUNDARY ELEMENTS</b>	<b>79</b>
	Derivation	79
	Rectangular Linear (RLIN) Element	82
	Rectangular Quadratic (RQUA) Element	85
	Rectangular Cubic (RCUB) Element	90
	Rectangular Overhauser (ROVR) Element	94
	Rectangular Side Overhauser (ROVRS) Element	98
	Rectangular Corner Overhauser (ROVRC) Element	101
	Rectangular Corner Overhauser Variant (ROVRCV) Element	104
	Integration	106
	Singular Integration	108
<b>VII.</b>	<b>THREE DIMENSIONAL CRACK TIP BOUNDARY ELEMENTS</b>	<b>117</b>
	Derivation	117
	Rectangular Side Overhauser Crack Tip (CTROVRS) Element	118
	Rectangular Corner Overhauser Crack Tip (CTROVRC) Element	122
	Rectangular Corner Overhauser Crack Tip Variant (CTROVRCV) Element	127
	Integration	132
	Singular Integration	134
	Stress Intensity Factor Calculation	143
<b>VIII.</b>	<b>EXAMPLE ANALYSES</b>	<b>145</b>
	Double Edge Cracked Plate	145
	Center Cracked Plate	151

Full Model Center Cracked Plate . . . . .	156
Center Slant Crack in an Infinite Domain . . . . .	157
Elliptical Crack in an Infinite Region . . . . .	159
Compact Tension Specimen . . . . .	162
<b>IX. CONCLUSIONS . . . . .</b>	<b>168</b>
<b>BIBLIOGRAPHY . . . . .</b>	<b>172</b>



## LIST OF TABLES

Table	Page
1. 2D Singular Integration Mapping Summary . . . . .	72
2. Comparison of Selected Results between the Full and Quarter Model Center Cracked Plate . . . . .	157
3. Comparison of Stress Intensity Factors for the Center Slant Crack in an Infinite Domain . . . . .	158
4. Compact Tension Specimen SIF Comparison With the Plane Strain Value of $K_I = 6.73 \text{ ksi} \cdot \text{in}^{1/2}$ . . . . .	166

## LIST OF FIGURES

Figure	Page
1. Notation for an Elastic Body . . . . .	10
2. Two Subregion BEM Model . . . . .	19
3. Three Basic Loading Modes for a Cracked Body: $K_I$ – Crack Opening Mode, $K_{II}$ – Crack Sliding Mode, and $K_{III}$ – Crack Tearing Mode . . . . .	20
4. Crack Tip Coordinates for 2D . . . . .	21
5. Crack Tip Coordinates for 3D . . . . .	23
6. LINE Element Geometry and Parametric Mapping . . . . .	27
7. LINE Element Shape Functions . . . . .	28
8. QUAD Element Geometry and Parametric Mapping . . . . .	29
9. QUAD Element Shape Functions . . . . .	30
10. CUBIC Element Geometry and Parametric Mapping . . . . .	31
11. CUBIC Element Shape Functions . . . . .	32
12. OVER Element Geometry and Parametric Mapping . . . . .	33
13. OVER Element Shape Functions . . . . .	36
14. OVRR Element Geometry and Parametric Mapping . . . . .	39
15. OVRR Element Shape Functions . . . . .	40
16. OVRL Element Geometry and Parametric Mapping . . . . .	42
17. OVRL Element Shape Functions . . . . .	43

18.	CTQT Element Traction Shape Functions . . . . .	54
19.	CTQUA Element Geometry and Parametric Mapping . . . . .	56
20.	CTQUA Displacement Shape Functions . . . . .	57
21.	CTQUA Traction Shape Functions . . . . .	58
22.	CTOVR Element Geometry and Parametric Mapping . . . . .	60
23.	CTOVR Geometry Shape Functions . . . . .	61
24.	CTOVR Displacement Shape Functions . . . . .	62
25.	CTOVR Traction Shape Functions . . . . .	65
26.	2D Singular Integration Configuration . . . . .	71
27.	2D SIF Configuration . . . . .	73
28.	Coons Surface Configuration . . . . .	80
29.	RLIN Element Geometry . . . . .	82
30.	RLIN $N_0$ Shape Function . . . . .	84
31.	RQUA Element Geometry . . . . .	85
32.	RQUA $N_0$ Shape Function . . . . .	88
33.	RQUA $N_1$ Shape Function . . . . .	89
34.	RCUB Element Geometry . . . . .	90
35.	RCUB $N_0$ Shape Function . . . . .	92
36.	RCUB $N_1$ Shape Function . . . . .	93
37.	ROVR Element Geometry . . . . .	94
38.	ROVR $N_0$ Shape Function . . . . .	96
39.	ROVR $N_3$ Shape Function . . . . .	97
40.	ROVRS Element Geometry . . . . .	98

41.	ROVRS $N_2$ Shape Function . . . . .	100
42.	ROVRC Element Geometry . . . . .	101
43.	ROVRC $N_0$ Shape Function . . . . .	103
44.	ROVRCV Element Geometry . . . . .	104
45.	Triangle to Square Transformation . . . . .	109
46.	RLIN Singular Integration With Source at Node $x_{0j}$ . . . . .	111
47.	RQUA Singular Integration With Source at Node $x_{7j}$ . . . . .	113
48.	Crack Tip Coons Surface Configuration . . . . .	118
49.	CTROVRS Element Geometry . . . . .	119
50.	CTROVRS $N_2^p(s, t)$ Shape Function . . . . .	123
51.	CTROVRS $N_3^p(s, t)$ Shape Function . . . . .	124
52.	CTROVRC Element Geometry . . . . .	125
53.	CTROVRC $N_0^p(s, t)$ Shape Function . . . . .	127
54.	CTROVRC $N_1^p(s, t)$ Shape Function . . . . .	128
55.	CTROVRCV Element Geometry . . . . .	129
56.	CTROVRCV $N_0^p(s, t)$ Shape Function . . . . .	132
57.	CTROVRCV $N_1^p(s, t)$ Shape Function . . . . .	133
58.	Quadratic Shape Functions for Singular Integration . . . . .	136
59.	Shape Function Derivation for Triangle to Square Transformation for Crack Tip Overhauser Type Elements . . . . .	137
60.	Shape Function Derivation for Triangle to Square Transformation for the CTROVRS and CTROVRC Element . . . . .	138
61.	Shape Function Derivation for Triangle to Square Transformation for the CTROVRCV Element . . . . .	139

62.	Double Edge Cracked Plate . . . . .	146
63.	Cracked Plate BEM Mesh . . . . .	147
64.	Percent Error in $K_I$ for Double Edge Cracked Plate With CTQQ and CTQT Elements . . . . .	148
65.	Percent Error in $K_I$ for Double Edge Cracked Plate With CTQUA Elements . . . . .	149
66.	Percent Error in $K_I$ for Double Edge Cracked Plate With CTOVR Elements . . . . .	150
67.	Comparison of Percent Errors in $K_I$ Calculated by the Traction Method for Double Edge Cracked Plate . . . . .	151
68.	Center Cracked Plate . . . . .	152
69.	Percent Error in $K_I$ for Center Cracked Plate With CTQQ and CTQT Elements . . . . .	153
70.	Percent Error in $K_I$ for Center Cracked Plate With CTQUA Elements . . . . .	154
71.	Percent Error in $K_I$ for Center Cracked Plate With CTOVR Elements . . . . .	155
72.	Comparison of Percent Errors in $K_I$ Calculated by the Traction Method for Center Cracked Plate . . . . .	156
73.	Center Slant Crack in an Infinite Domain . . . . .	158
74.	Elliptical Crack in an Infinite Region . . . . .	159
75.	Crack Face Close Up for the Elliptical Crack in an Infinite Region . . . . .	160
76.	Elliptical Crack BEM Mesh . . . . .	161
77.	Elliptical Crack Overall BEM Mesh . . . . .	162
78.	Percent Error in $K_I$ for the Elliptical Crack in an Infinite Region . . . . .	163
79.	Standard Compact Tension Specimen (after Luchi and Rizzuti, 1987) . . . . .	164
80.	Compact Tension Specimen Model . . . . .	165

81. Compact Tension Specimen BEM Mesh . . . . .	166
82. Compact Tension Specimen SIF Variation Along the Crack Front . . . .	167

# Chapter I

## INTRODUCTION

For those not familiar with fracture mechanics, perhaps a broad definition might be in order.

Fracture mechanics is an engineering discipline that quantifies the conditions under which a load-bearing solid body can fail due to the enlargement of a dominant crack contained in that body. [37]

Engineers have always been concerned with fracture since it often has unexpected and tragic consequences. More recently, lightweight designs and small factors of safety have contributed to the interest in fracture mechanics and given rise to the concept of damage tolerance. Nondestructive evaluation allows for determination of crack-like flaws and their severity. Using fracture mechanics, the flawed part is then evaluated as to whether it should be removed from service or not.

Linear elastic fracture mechanics (LEFM) is conceptually similar to an elastic analysis. An analysis is made of a geometric configuration giving some sort of maximum stress. That maximum stress is compared in some manner to an experimentally determined yield stress. For example, the calculated octahedral shear stress is compared to the yield stress for the material through the von Mises theory of failure. Similarly, in LEFM, a mathematical analysis of a geometric configuration is made

to determine the stress intensity factor (SIF),  $K$ . The fracture toughness  $K_c$  is then independently determined for a particular material, and  $K$  and  $K_c$  are compared. There are other material parameters that play a similar role in fracture mechanics, such as the  $J$  integral. These parameters will be more completely defined in later chapters.

While there are nonlinear fracture mechanics analyses, LEFM plays a major part in them, just as elasticity plays a major part in a plasticity analysis. Advances in LEFM will therefore often translate into advances in nonlinear fracture mechanics.

Stress intensity factors can be determined in a number of ways. For a few simple geometries, an analytic solution is possible. Large scale testing is also possible, although not practical in most situations. Today, much work is done numerically, primarily using the finite element method (FEM) and the boundary element method (BEM).

The objective of this dissertation is to better represent the geometry of a crack through the use of parametric continuous boundary elements in both two and three dimensions and thus enhance the accuracy of the boundary element method in the solution of linear elastic fracture mechanics problems. Methods will be introduced for evaluating the stress intensity factors most appropriate for the boundary element method along with integration procedures for the new elements.



# Chapter II

## LITERATURE REVIEW

### Numerical Methods in Linear Elastic

### Fracture Mechanics

This section will give a very brief outline of finite elements and boundary elements as applied to LEFM and then a more detailed background on the development of crack tip elements and the evaluation of fracture mechanics parameters.

Chan, Tuba, and Wilson [15] were some of the first investigators to use the finite element method to determine stress intensity factors. A number of researchers then developed special elements that contained the singularity at the crack tip. Isoparametric elements that had the singularity were developed independently by Henshell and Shaw [30] and Barsoum [6]. Stress intensity factors are then typically calculated using the  $J$  integral developed by Rice [53].

There are a number of ways that the solution of fracture mechanics problems can be approached with the BEM. The first approach was to use Kelvin's fundamental solution with many Lagrangian isoparametric elements to model the crack [18,24]. There have been some advances with higher-order elements and self-adaptive meshes using this approach. For a detailed review of advancements of the boundary element

method in fracture mechanics, the reader is referred to References [21] and [55].

There are also modified boundary element methods. Snyder and Cruse [56] developed a new complex Green's function for a straight center crack in an infinite anisotropic plate that eliminated the need to model the crack at all. The method was later improved by Cruse [20]. Mews [48] extended the method to straight and angled center and edge cracks in isotropic materials. The subtraction of the singularity technique was introduced by Symm for potential problems [60] and Aliabadi for elasticity problems [1]. The weight function method involves calculating the strain energy release by means of an integral over the crack surface. This method was originated by Bueckner [14]. The displacement discontinuity method [17] typically models only the crack and solutions are the differences in tractions [22] or displacements [59] across the crack surface. Stress intensity factors are then calculated from the solution. The method is typically applied in infinite regions and early results in finite regions are not promising [27].

Another approach is to use special crack tip elements with the standard Kelvin's fundamental solution in multiple regions. This approach is very general, as any straight or curved crack can be modeled in two or three dimensions. Two areas must be investigated when working LEFM problems by the BEM using crack tip elements. The first is the numerical evaluation of the stress intensity factors or related material parameters, and the second is the modeling of the crack itself with various crack tip elements.

## Evaluation of Stress Intensity Factors

Methods for the evaluation of stress intensity factors can be roughly broken into two categories. The first method is an integral equation method. The second method uses information from the nodes near the crack tip.

The path independent contour integral,  $J$ , developed by Rice [53], is one manner of characterizing the crack. It has the advantage in that it is valid for both linear and nonlinear fracture mechanics. There are other invariant integrals as well [40,13]. Snyder and Cruse [56] developed path independent integrals for determining stress intensity factors for a center cracked anisotropic infinite plate. Kishitani, Hirai, and Murakami [39] calculated the  $J$  integral by specifying a separate path through the domain of the problem. While they achieved good results for some problems, this approach is not in the "spirit" of the BEM. There are also serious numerical problems with this approach. As the internal points get closer to an element, the fundamental BEM solution gets more singular, resulting in poor answers. While these numerical difficulties may be overcome in some instances, a practical approach has not yet been developed. Therefore, this approach will not be considered further.

At first, the stress intensity factor,  $K$ , was extrapolated from the displacements of a sequence of nodes near the crack tip [15,24]. This gave way to what is called the single-point, first-order displacement formula for calculating  $K$ , and later to the two-point formula [8]. Martínez and Domínguez [46] developed a traction nodal value formula which gives the stress intensity factor based on the traction nodal values at the crack tip. For the problems they examined, the traction nodal value formula gave

the best results and is relatively independent of the crack element size. Jia, Shippy, and Rizzo [35,36] confirmed their results. This approach also takes advantage of the traction solution that is unique to the BEM. For these reasons, the one and two point displacement formulas and the traction formulas will be used in this work, with a concentration on the latter.

## Crack Tip Elements

Crack tip elements originated in the context of the FEM. Although some special hybrid crack tip finite elements had been developed previously, Henshell and Shaw [30] showed that isoparametric quadratic quadrilateral finite elements displayed the appropriate square root singularity ( $\sqrt{r}$ ) at the crack tip by moving the mid-side nodes to the quarter point position, where  $r$  is the distance from the crack tip. Concurrently, Barsoum [6] developed quadratic triangular, quadrilateral, prism, and brick crack tip elements. He also showed that the quadratic triangular element has the appropriate  $\sqrt{r}$  singularity along all rays emanating from the crack tip. Shih, deLorenzi, and German [54] make a correction to the formula for  $K$  developed by Barsoum and compare the calculation of  $K$  versus the calculation of the  $J$  integral. Because Barsoum obtained better results with quadratic triangular elements than quadratic quadrilateral elements, Hibbitt [31] suggested the strain energy of the quadratic quadrilateral elements was unbounded. Ying [69] showed this to be incorrect. However, the tendency to use triangular elements persists today. Lynn and Ingraffea [45] developed quadratic transition elements, and Hussain, Vasilakis,

and Pu [33] developed cubic transition elements that go between the standard elements and the crack tip elements in order to improve on the solution accuracy. Murti and Valliappan [50] made several corrections in the derivation of transition elements. Bank-Sills and Bortman reviewed the use of quadratic quadrilaterals [4]. Bank-Sills [3] expanded on her previous work and concluded that quadratic quadrilaterals must be rectangular and quadratic triangles may be any shape as long as the edges are straight for the element to have the proper  $\sqrt{r}$  singularity along all rays emanating from the crack tip.

Crack tip elements were introduced into the BEM by Cruse and Wilson [25] where they employed symmetry in the analysis. In the BEM, unlike the FEM, the same shape functions are typically used for both the displacements and the tractions. Therefore, the traction shape functions must be modified to obtain the proper  $1/\sqrt{r}$  singularity at the crack tip. Blandford, Ingraffea, and Liggett [8] expanded on the two dimensional portion of Cruse and Wilson's work and employed transition elements that were not corrected for the  $1/\sqrt{r}$  singularity for the tractions. They also introduced the idea of using multiple regions, one on each side of a crack. Mason and Smith [47] compare the one and two point displacement formulae for curved crack problems. Van Der Weeën [62] employed quadratic and cubic crack tip and transition elements, each with proper singularities, in the solution of anisotropic plates. He obtained the best results with cubic crack tip and transition elements. This would seem to indicate that higher order elements give better solutions.

Three dimensional crack problems were solved using constant boundary elements

by Cruse and Vanburen [24] and using linear triangular elements by Cruse and Meyers [23]. Tan and Fenner [61] used standard quadratic quadrilateral boundary elements to solve several crack problems. Luchi and Poggialini [42] were apparently the first to properly model the  $1/\sqrt{r}$  singularity in the tractions with the use of a set of special shape functions they developed. Luchi and Rizzuti [44] expanded on Reference [42] by employing the stress intensity factor calculation approach of Martínez and Domínguez [46] and a special series of mappings for singular element integrations. Jia, Shippy, and Rizzo [36] use a multi-domain method to solve a number of crack problems. They used shape functions of Reference [42] and a combination of Cartesian and polar mappings for singular element integrations.

# Chapter III

## BOUNDARY ELEMENT FORMULATION FOR LINEAR ELASTIC FRACTURE MECHANICS

### Linear Elastostatics

The basic theory for applying the BEM to linear elastostatic problems is well developed and can be found in numerous texts [2,11,10,29,49]. The basic equations are developed here for completeness and use the same notation as [10]. Indicial notation will be used throughout this development, where repeated indices indicate a sum and a comma indicates a derivative.

A linear elastic, isotropic, homogeneous, three-dimensional body  $\Omega$  is bounded by a surface  $\Gamma$  which consists of the sum of its two parts  $\Gamma_1$  and  $\Gamma_2$  (Figure 1). The governing differential equations of equilibrium for a differential element of the body  $\Omega$  are

$$\sigma_{ij,j} + b_i = 0 \quad \text{in } \Omega \quad (1)$$

in which  $\sigma_{ij}$  are the stress components, and  $b_i$  are the components of the body force

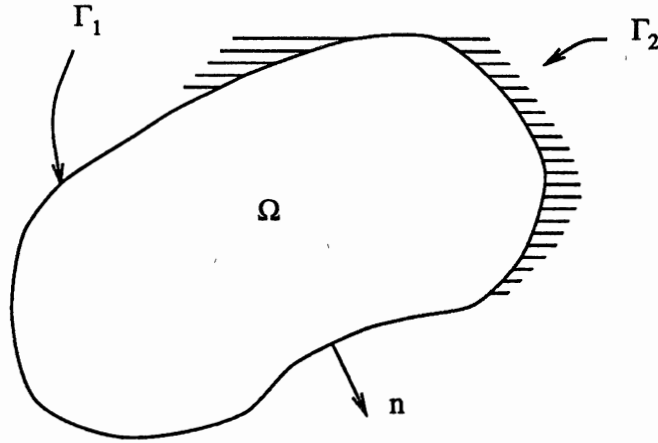


Figure 1. Notation for an Elastic Body

per unit volume. The surface tractions  $p_i$  are related to the surface stress components by

$$p_i = \sigma_{ij}n_j \quad \text{on } \Gamma \quad (2)$$

where  $n_j$  is the outward directed unit surface normal. In order for the problem to be well posed, the boundary conditions must be one of two types

$$u_i = \bar{u}_i \quad \text{on } \Gamma_1 \quad (3)$$

where  $u_i$  are the displacements and  $\bar{u}_i$  are the specified displacements or

$$p_i = \sigma_{ij}n_j = \bar{p}_i \quad \text{on } \Gamma_2 \quad (4)$$

where  $\bar{p}_i$  are the specified tractions.



The kinematic equations assuming small strains and displacements are

$$\varepsilon_{ij} = \frac{1}{2}(u_{i,j} + u_{j,i}) \quad (5)$$

in which  $\varepsilon_{ij}$  are the components of the strain.

The constitutive relations may be written in terms of the modulus of elasticity,  $E$ , and Poisson's ratio,  $\nu$ ,

$$\varepsilon_{ij} = -\frac{\nu}{E}\sigma_{kk}\delta_{ij} + \frac{1+\nu}{E}\sigma_{ij} \quad (6)$$

or

$$\sigma_{ij} = \frac{E}{1+\nu} \left[ \frac{\nu}{1-2\nu}\delta_{ij}\varepsilon_{kk} + \varepsilon_{ij} \right] \quad (7)$$

where  $\delta_{ij}$  is the Kronecker delta. Of course, the shear modulus,  $\mu$ , can be written in terms of  $E$  and  $\nu$

$$\mu = \frac{E}{2(1+\nu)} \quad (8)$$

Substituting the kinematic equations (Equation 5) and the constitutive relations (Equation 7) into the equilibrium equations (Equation 1) yields Navier's equations (the equilibrium equations in terms of the displacements instead of the stresses):

$$\frac{1}{1-2\nu}u_{j,jl} + u_{l,jj} + \frac{1}{\mu}b_l = 0 \quad (9)$$

## Fundamental Solutions

The Kelvin fundamental solution of the effect of a unit load applied at the source or load point  $m$  on the field point in the direction of the unit vector  $e_i$

$$b_i = \Delta^m e_i \quad (10)$$

may be obtained from Navier's equations (Equation 9) using the Galerkin vector approach [19,32,10]. Displacements and tractions at any point in the domain due to this point load at  $m$  acting in the  $i$  direction are given by

$$u_j^* = u_{ij}^* e_i \quad (11)$$

$$p_j^* = p_{ij}^* e_i \quad (12)$$

Fundamental solutions are displacements or tractions in the  $j$  direction due to a unit load at the source point  $m$  or  $\zeta$  acting in the  $i$  direction. They are, for two dimensional displacements

$$u_{ij}^*(\zeta, \eta) = \frac{-1}{8\pi(1-\nu)\mu} [(3-4\nu)\ln(r)\delta_{ij} - r_{,i}r_{,j}] \quad (13)$$

for three dimensional displacements

$$u_{ij}^*(\zeta, \eta) = \frac{1}{16\pi(1-\nu)\mu r} [(3-4\nu)\delta_{ij} + r_{,i}r_{,j}] \quad (14)$$

and for two and three dimensional tractions

$$p_{ij}^*(\zeta, \eta) = \frac{-1}{4\alpha\pi(1-\nu)r^\alpha} \left[ \frac{\partial r}{\partial n} ((1-2\nu)\delta_{ij} + \beta r_{,i}r_{,j}) - (1-2\nu)(r_{,i}n_{,j} - r_{,j}n_{,i}) \right] \quad (15)$$

where  $\alpha = 1$  and  $\beta = 2$  for two dimensions, and  $\alpha = 2$  and  $\beta = 3$  for three dimensions. For two dimensional plane strain problems,  $\nu = \nu'$ , and for plane stress  $\nu = \nu'/(1 + \nu')$ . In the above equations

$$r_i = x_i(\eta) - x_i(\zeta) \quad (16)$$

$$r = \sqrt{r_i r_i} \quad (17)$$

$$r_{,i} = \frac{\partial r}{\partial x_i(\eta)} = \frac{r_i}{r} \quad (18)$$

$$\frac{\partial r}{\partial n} = \bar{\nabla} r \cdot \bar{n} = \frac{\partial r}{\partial x_i(\eta)} n_i = r_{,i} n_i \quad (19)$$

where  $\eta$  represents the field point and  $\zeta$  represents the source point.

Displacement and traction equations may be differentiated with respect to the source point to obtain

$$u_{,ijk}^* = \frac{1}{4\alpha\pi(1-\nu)r^\beta} [(1-2\nu)(r_{,j}\delta_{ki} + r_{,i}\delta_{jk} + r_{,k}\delta_{ij}) + \beta r_{,k}r_{,i}r_{,j}] \quad (20)$$

$$\begin{aligned}
p_{ijk}^* = \frac{\mu}{2\alpha\pi(1-\nu)r^\beta} \left\{ \beta \frac{\partial r}{\partial n} [(1-2\nu)\delta_{ij}r_{,k} \right. \\
+ \nu(\delta_{ik}r_{,j} + \delta_{jk}r_{,i}) - \gamma r_{,i}r_{,j}r_{,k}] \\
+ \beta\nu(n_i r_{,j}r_{,k} + n_j r_{,i}r_{,k}) - (1-4\nu)n_k \delta_{ij} \\
\left. + (1-2\nu)(\beta n_k r_{,i}r_{,j} + n_j \delta_{ik} + n_i \delta_{jk}) \right\}
\end{aligned} \tag{21}$$

where  $\alpha = 1$ ,  $\beta = 2$ , and  $\gamma = 4$  for two dimensions, and  $\alpha = 2$ ,  $\beta = 3$ , and  $\gamma = 5$  for three dimensions.

## Boundary Integral Formulation

The boundary integral formulation for elastostatics will be derived using the weighted residual approach. The formulation's relation to a derivation from Betti's reciprocal law will also be shown.

It is desired to minimize the error in the equilibrium equation (Equation 1) by multiplying it by an appropriate weighting function  $u_j^*$  and integrating over  $\Omega$ :

$$\int_{\Omega} (\sigma_{jk,j} + b_j) u_j^* d\Omega = 0 \tag{22}$$

Integrating by parts twice yields the adjoint of the Equation 1:

$$\int_{\Omega} \sigma_{jk,j}^* u_j d\Omega + \int_{\Omega} b_j u_j^* d\Omega = - \int_{\Gamma} p_j u_j^* d\Gamma + \int_{\Gamma} p_j^* u_j d\Gamma \tag{23}$$

If Equation 1 is substituted here, Betti's reciprocal theorem will result. Applying the boundary conditions to Equation 23 and integrating its first term by parts twice, the

generalized weighted residual statement results.

$$\int_{\Omega} (\sigma_{jk,j}^* u_j + b_j) d\Omega = \int_{\Gamma_2} (p_j - \bar{p}_j) u_j^* d\Gamma - \int_{\Gamma_1} (u_j - \bar{u}_j) p_j^* d\Gamma \quad (24)$$

The choice of weighting functions should be one that removes the domain integral of the stresses. By letting

$$\begin{aligned} b_i &= \Delta^m e_i \\ \sigma_{ik,k}^* + \Delta^m e_i &= 0 \\ u_j^* &= u_{ij}^* e_i \\ p_j^* &= p_{ij}^* e_i \end{aligned} \quad (25)$$

the domain integral of the stresses is transformed to

$$\int_{\Omega} \sigma_{jk,j}^* u_j d\Omega = \int_{\Omega} \sigma_{ik,k}^* u_i d\Omega = - \int_{\Omega} \Delta^m u_i e_i d\Omega = -u_i^m e_i \quad (26)$$

If the boundary conditions are applied at a later stage, Equation 24 simplifies to Somigliana's identity, which gives displacements of internal points in terms of boundary values and body forces:

$$u_i^m + \int_{\Gamma} p_{ij}^* u_j d\Gamma = \int_{\Gamma} u_{ij}^* p_j d\Gamma + \int_{\Omega} u_{ij}^* b_j d\Omega \quad (27)$$

Somigliana's identity cannot be evaluated directly when the source point is on the boundary. Therefore, let the source point be surrounded by a small hemispherical region. Taking the limit as the volume of the small hemispherical region goes to zero,

the following equation is obtained:

$$c_{ij}^m u_i^m + \int_{\Gamma} p_{ij}^* u_j d\Gamma = \int_{\Gamma} u_{ij}^* p_j d\Gamma + \int_{\Omega} u_{ij}^* b_j d\Omega \quad (28)$$

where the  $c_{ij}$  term depends on the boundary geometry. It is most commonly evaluated using the rigid body motion auxiliary equation

$$c_{ij}^m = \int_{\Gamma} p_{ij}^* d\Gamma \quad (29)$$

Displacements at points internal to the body may be found from Somigliana's identity (Equation 28) with  $c_{ij} = \delta_{ij}$ . Stresses at internal points may be found from Equation 27 differentiation with respect to the source point:

$$\sigma_{ik} = \int_{\Gamma} p_{ijk}^* u_i d\Gamma - \int_{\Gamma} u_{ijk}^* p_i d\Gamma + \int_{\Omega} u_{ijk}^* b_i d\Omega \quad (30)$$

where  $u_{ijk}^*$  and  $p_{ijk}^*$  are given in Equations 20 and 21. From this point on, we will not be concerned with body forces and therefore those terms of Equations 28 and 30 will be dropped.

## Boundary Discretization

The boundary of the domain is discretized into a series of elements, hence the name "boundary elements." The variation of the geometry, displacements, and tractions may be *independently* approximated in the following manner:

$$\begin{aligned} x_j &= N_l^g x_{lj} \\ u_j &= N_l^u u_{lj} \\ p_j &= N_l^p p_{lj} \end{aligned} \tag{31}$$

where  $N_l^g$  are the geometry shape functions corresponding to node  $l$  on the element, and  $x_{lj}$  is the coordinate in direction  $j$  of node  $l$  of the element. The displacements and tractions are similar. Normally the same set of shape functions is used for all approximations; but as we shall see, they are different for crack tip elements.

Substituting the above approximation into Equation 28 and factoring out the boundary values yields

$$c_{ij}^m u_i^m + u_{lj} \int_{\Gamma} p_{ij}^* N_l^u d\Gamma = p_{lj} \int_{\Gamma} u_{ij}^* N_l^p d\Gamma \tag{32}$$

By forming this equation from every source node  $m$  in the boundary element mesh, a system of simultaneous equations relating the known and unknown boundary displacements and tractions results and has the form

$$[H] \{u\} = [G] \{p\} \tag{33}$$

The well posed boundary value problem has either a displacement or a traction specified at every node in every direction on the boundary. This implies Equation 33 can be rearranged such that

$$[A]\{x\} = \{y\} \quad (34)$$

where all unknown displacements and tractions are in the  $x$  vector and all known displacements and tractions are in the  $y$  vector. This system of equations is fully populated for single-region problems and is in general neither symmetric nor positive definite. Once the system of equations is solved, both the displacements and tractions are known at all points on the boundary and they can be employed to find the displacements and stresses at internal points using Equation 30.

Equation 32 can be further broken down into integrals over each boundary element in the mesh:

$$H_{ijl}^e = \int_{\Gamma^e} p_{ij}^* N_l^u d\Gamma^e \quad (35)$$

$$G_{ijl}^e = \int_{\Gamma^e} u_{ij}^* N_l^p d\Gamma^e \quad (36)$$

Shape functions and methods for integration and their respective derivations are examined in the next several chapters and constitute the major portion and innovation of this work.

## Subregions

In some cases the boundary element model may be piecewise homogeneous as shown in Figure 2. In that case, the boundary element procedure may be applied to



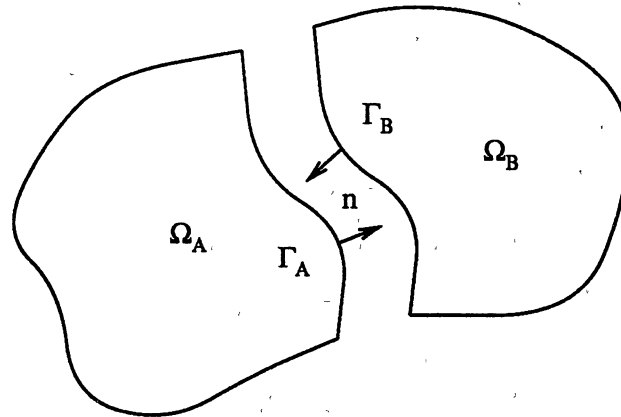


Figure 2. Two Subregion BEM Model

each region independently and the regions tied together with Equation 37 applied to the nodes along the interface between the regions.

$$u_A = u_B \quad (37)$$

$$p_A = -p_B$$

This approach is particularly useful when modeling crack problems. The interface on either side of a crack is “stitched” together, while the crack surface is left traction-free.

## Linear Elastic Fracture Mechanics

Linear elastic fracture mechanics analysis is based on the concept of small scale yielding. The region of inelastic deformation at the crack tip must be small with respect to the size of the crack or any other characteristic length [37]. LEFM neglects the localized effects at the crack tip such as plasticity and microcracking, and relates the stress field directly to the geometry and applied stresses.

## Two Dimensional LEFM

Irwin [34] largely developed the idea of stress intensity factors which is shown in Figure 3 The crack tip geometry and stresses for two dimensional problems is defined

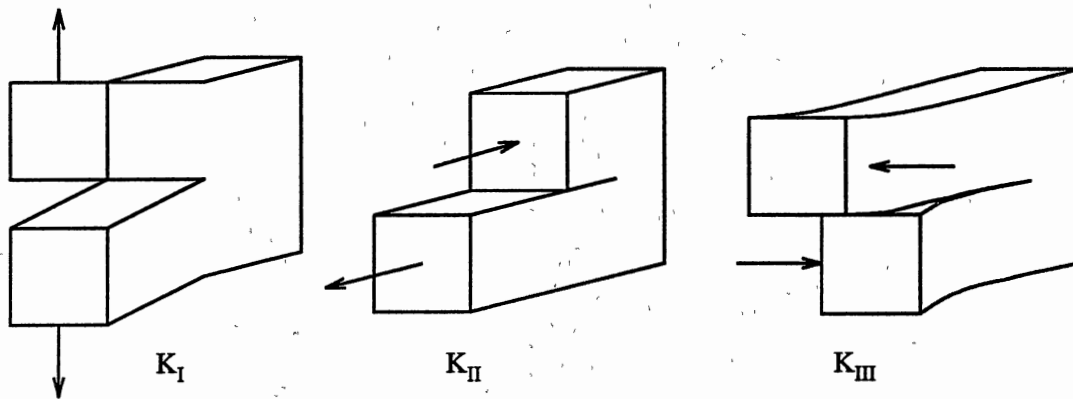


Figure 3. Three Basic Loading Modes for a Cracked Body:  $K_I$  – Crack Opening Mode,  $K_{II}$  – Crack Sliding Mode, and  $K_{III}$  – Crack Tearing Mode

in Figure 4.

Irwin determined that a geometry dependent factor (the stress intensity factor),  $K$ , may be used to characterize stresses at the crack tip. For a crack of length  $2a$  in an infinite plate subjected to a uniform tension  $\sigma$ ,  $K_I$  has a value  $\sigma\sqrt{\pi a}$ . In a more general setting, substitution of Irwin's definition of  $K$  into William's [67] eigenfunction expansion for stresses of a traction-free crack in an infinite domain yields stresses defined in terms of the stress intensity factors. For  $r$  much smaller

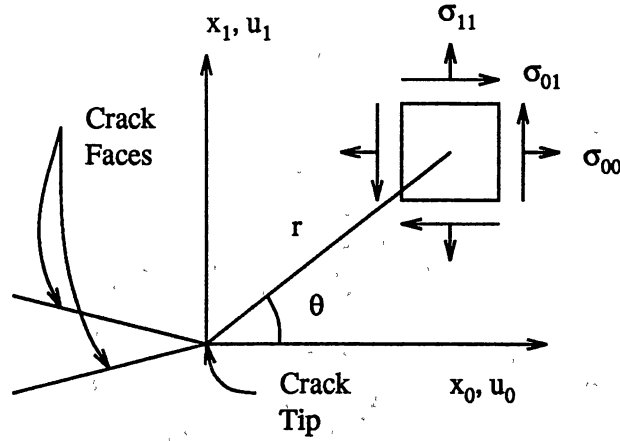


Figure 4. Crack Tip Coordinates for 2D

than the size of the crack and neglecting higher order terms, the expansions are

$$\sigma_{00} = \frac{K_I}{\sqrt{2\pi r}} \cos \frac{\theta}{2} \left( 1 - \sin \frac{\theta}{2} \sin \frac{3\theta}{2} \right) - \frac{K_{II}}{\sqrt{2\pi r}} \sin \frac{\theta}{2} \left( 2 + \cos \frac{\theta}{2} \cos \frac{3\theta}{2} \right) \quad (38)$$

$$\sigma_{11} = \frac{K_I}{\sqrt{2\pi r}} \cos \frac{\theta}{2} \left( 1 + \sin \frac{\theta}{2} \sin \frac{3\theta}{2} \right) + \frac{K_{II}}{\sqrt{2\pi r}} \sin \frac{\theta}{2} \cos \frac{\theta}{2} \cos \frac{3\theta}{2} \quad (39)$$

$$\sigma_{01} = \frac{K_I}{\sqrt{2\pi r}} \cos \frac{\theta}{2} \sin \frac{\theta}{2} \cos \frac{3\theta}{2} + \frac{K_{II}}{\sqrt{2\pi r}} \cos \frac{\theta}{2} \left( 1 - \sin \frac{\theta}{2} \sin \frac{3\theta}{2} \right) \quad (40)$$

The displacements near the crack tip are

$$u_0 = \frac{K_I}{\mu} \sqrt{\frac{r}{2\pi}} \cos \frac{\theta}{2} \left( 1 - 2\nu + \sin^2 \frac{\theta}{2} \right) + \frac{K_{II}}{\mu} \sqrt{\frac{r}{2\pi}} \sin \frac{\theta}{2} \left( 2 - 2\nu + \cos^2 \frac{\theta}{2} \right) \quad (41)$$

$$u_1 = \frac{K_I}{\mu} \sqrt{\frac{r}{2\pi}} \sin \frac{\theta}{2} \left( 2 - 2\nu - \cos^2 \frac{\theta}{2} \right) + \frac{K_{II}}{\mu} \sqrt{\frac{r}{2\pi}} \cos \frac{\theta}{2} \left( -1 + 2\nu + \sin^2 \frac{\theta}{2} \right) \quad (42)$$

When crack tip boundary elements are employed, the displacement and tractions

at the crack tip are properly modeled and the stress intensity factors may be directly obtained from the displacement and traction solution. The so-called one point displacement formula may be found by equating displacements at one point on the crack tip element with  $u_1$  and  $u_2$  and solving for the stress intensity factors. The two point displacement formula may be found for symmetric problems by equating the coefficients of  $\sqrt{r}$  in Equation 41 or 42 with the coefficients of  $\sqrt{r}$  in the displacement shape functions of the element type in question. The traction formula is derived by taking the limit of the product of the coefficient of the stress intensity factors in Equations 38, 39 and 40 with the traction shape function at the crack tip. These operations need to be performed for each type of crack tip boundary element that properly models the tractions and will be covered in more detail in Chapter V. The traction formula has special significance in boundary element analysis because it depends only on the traction solution values at the crack tip which are obtained directly from the boundary element formulation and it is relatively insensitive to the element length.

### **Three Dimensional LEFM**

The crack tip geometry and stresses for three dimensional problems are defined in Figure 5.

The relations between the stresses and displacements and stress intensity factors are the same in three dimensions as they are in two dimensions with the following

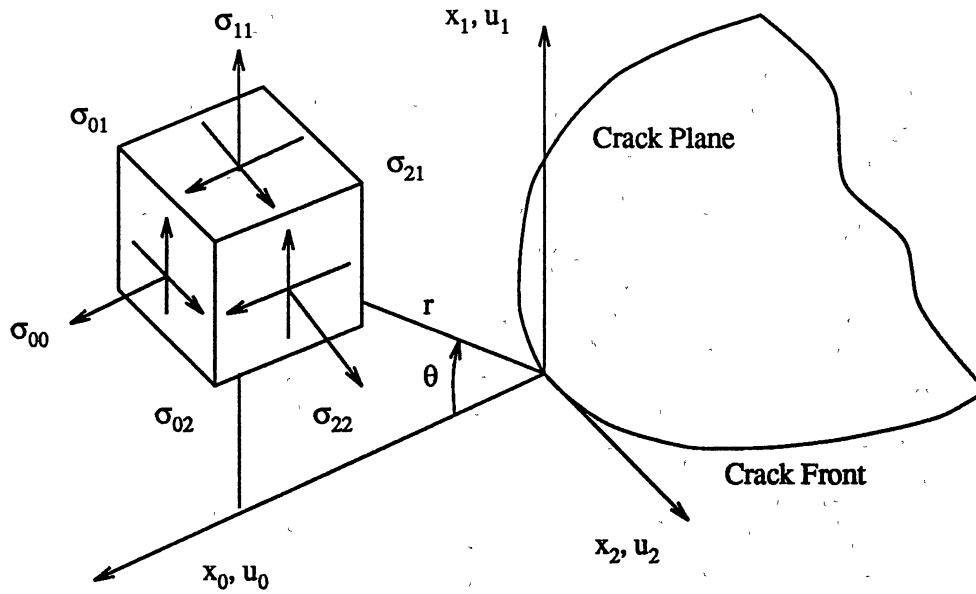


Figure 5. Crack Tip Coordinates for 3D

additions:

$$\sigma_{22} = 2\nu \frac{K_I}{\sqrt{2\pi r}} \cos \frac{\theta}{2} - 2\nu \frac{K_{II}}{\sqrt{2\pi r}} \sin \frac{\theta}{2} \quad (43)$$

$$\sigma_{21} = \frac{K_{III}}{\sqrt{2\pi r}} \cos \frac{\theta}{2} \quad (44)$$

$$\sigma_{02} = -\frac{K_{III}}{\sqrt{2\pi r}} \sin \frac{\theta}{2} \quad (45)$$

$$u_2 = \frac{2K_{III}}{\mu} \sqrt{\frac{r}{2\pi}} \sin \frac{\theta}{2} \quad (46)$$

Stress intensity factors can be determined in a manner similar to those in two dimensions and will be derived for the three dimensional crack tip elements in Chapter VII.

# Chapter IV

## TWO DIMENSIONAL BOUNDARY ELEMENTS

In this chapter, the noncrack tip two dimensional shape functions will be derived and their application in the boundary element method examined. As discussed in Chapter III, the variation of geometry, displacements, and tractions over an element may be approximated by a series of shape functions. Each element is comprised of a series of nodes where the geometry, displacements, and tractions may be specified. In general, these shape functions must form an interpolating curve, one that passes through all of the nodes. There are other shape functions that generate approximating curves. These shape functions form curves that may or may not actually pass through the nodes. However, for shape functions to be useful in the most common boundary elements formulation, the curve must be of the interpolating type and therefore has the same number of shape functions as nodes on the elements.

All of the elements discussed in this chapter will have the isoparametric formulation: shape functions for the geometry, displacements, and tractions will be the same.

## Derivation

The shape functions for the standard parametric two dimensional elements can be derived in one of several ways [52]:

- Inspection
- Simultaneous Equations
- Lagrange Interpolating Polynomials
- Divided Differences

The last three approaches should yield the the same results when only positional ( $C^0$ ) information is used. They will each be used where it is most appropriate in derivations for various element types, which will be described later in their respective sections.

The shape functions may be found directly from the Lagrange polynomial

$$N_l(\xi) = L_l^n(\xi) = \prod_{\substack{m=0 \\ m \neq l}}^n \frac{\xi - \xi_m}{\xi_l - \xi_m} \quad (47)$$

where  $n$  is the degree of the polynomial (i.e., for a quadratic  $n = 2$ ),  $\xi$  is the parameter along the element, and  $\xi_l$  and  $\xi_m$  are the values of the parameter at the positions corresponding to  $l$  and  $m$ , respectively. Shape functions derived in this manner are often called Lagrangian shape functions.

It is often desirable that shape functions have one or more of the following properties. The first property is positivity:

$$N_I(\xi_m) \geq 0 \quad \text{for } \xi_m \in [0, 1] \quad (48)$$

This property assures that the curve segment formed by these shape functions lies completely within the convex hull of the points forming the curve. Another property similar to this one, but only concerned with the shape function values at the nodes, is given in Equation 49:

$$N_I(\xi_m) = \delta_{Im} \quad (49)$$

The second property is the partition of unity:

$$\sum_{l=0}^n N_l(\xi) = 1 \quad (50)$$

This property ensures that the curve is invariant under affine transformations.

It shall be seen that crack tip boundary elements often do not satisfy either Equation 49 or 50. However, all shape functions considered in this work will have the property of affine transformation invariance.

## **Linear (LINE) Element**

The simplest and least accurate of the two dimensional element types is the linear element, which is defined by two nodes, one at each end of the element. The **LINEar**



element type will be abbreviated LINE. The geometry and parametric mapping for the LINE element is shown in Figure 6. The LINE shape functions are easily derived

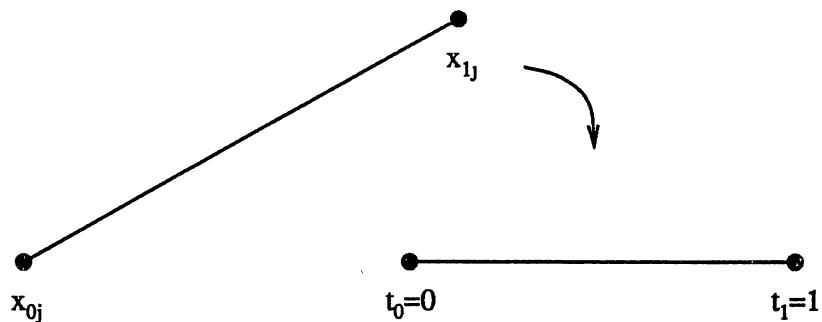


Figure 6. LINE Element Geometry and Parametric Mapping

using Equations 47 and 51:

$$n = 1 \quad \text{and} \quad t_m = \langle 0 \quad 1 \rangle \quad (51)$$

The LINE shape functions are given in Equation 52 and are plotted in Figure 7. Since the displacement and traction shape functions are same as the geometry shape functions, only the geometry shape functions are given and the superscript  $g$  has been dropped:

$$\begin{aligned} N_0(t) &= 1 - t \\ N_1(t) &= t \end{aligned} \quad (52)$$

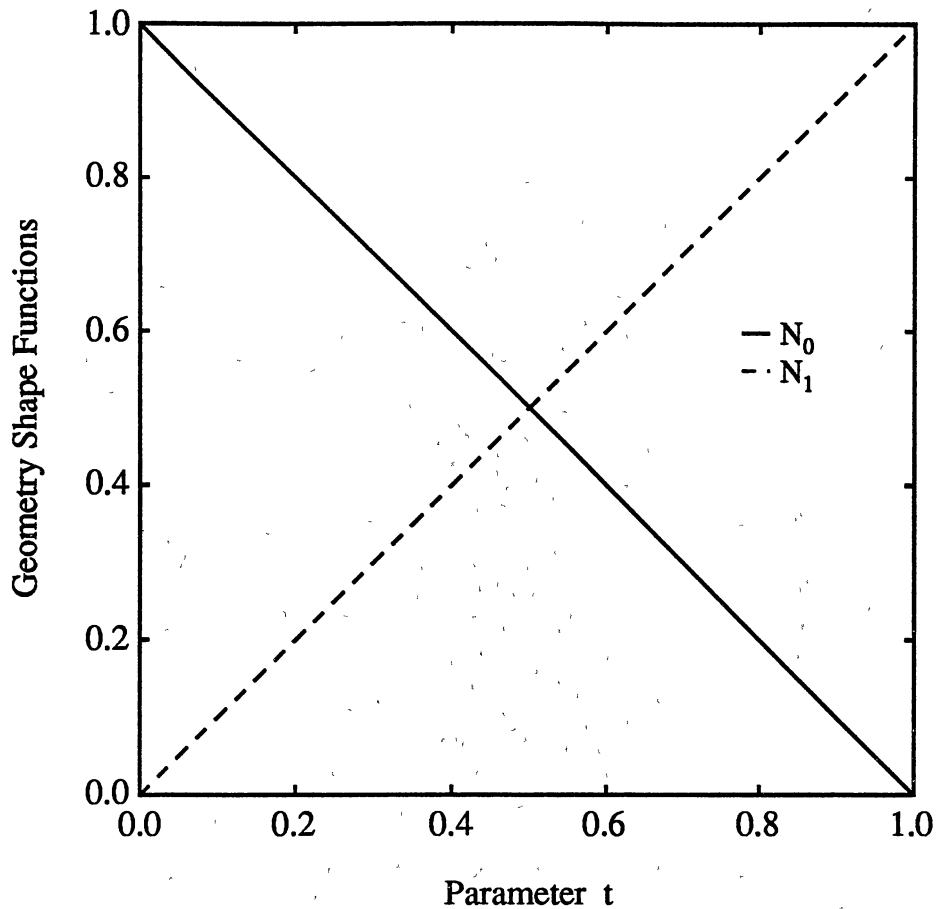


Figure 7. LINE Element Shape Functions

### Quadratic (QUAD) Element

The quadratic element is the simplest element that is of practical use in elastostatics, since it can properly model bending. The QUADdratic element type will be abbreviated QUAD. It is defined by three nodes as shown in Figure 8. The QUAD shape functions are easily derived using Equations 47 and 53:

$$n = 2 \quad \text{and} \quad t_m = \langle 0 \quad 1/2 \quad 1 \rangle \quad (53)$$

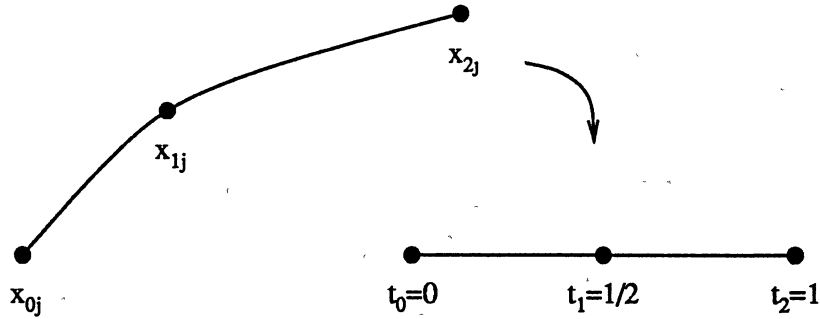


Figure 8. QUAD Element Geometry and Parametric Mapping

The QUAD shape functions are given in Equation 54

$$\begin{aligned}
 N_0(t) &= (t-1)(2t-1) \\
 N_1(t) &= -4(t-1)t \\
 N_2(t) &= t(2t-1)
 \end{aligned}
 \tag{54}$$

and are plotted in Figure 9.

### Cubic (CUBIC) Element

The next higher order element is the cubic element. The **CUBIC** element type will be represented by CUBIC. It is defined by four nodes as shown in Figure 10.

The CUBIC shape functions are easily derived using Equations 47 and 55:

$$n = 3 \quad \text{and} \quad t_m = \langle 0 \quad 1/3 \quad 2/3 \quad 1 \rangle
 \tag{55}$$

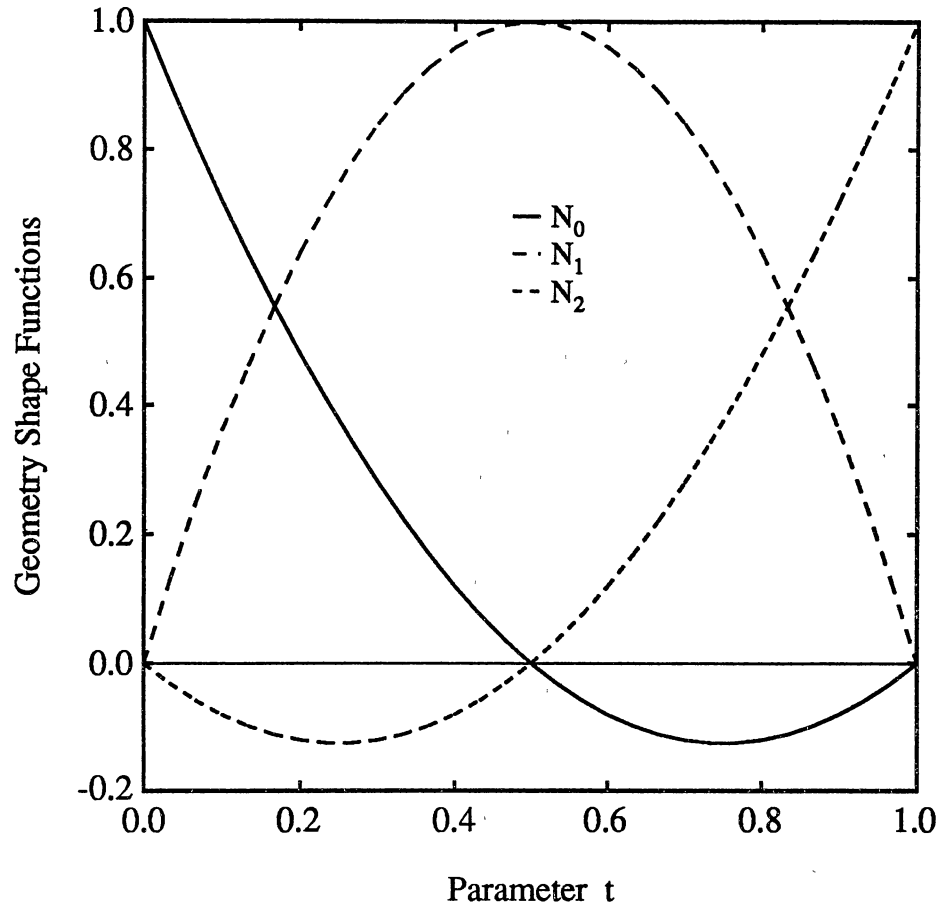


Figure 9. QUAD Element Shape Functions

The CUBIC shape functions are given in Equation 56 and are plotted in Figure 11:

$$\begin{aligned}
 N_0(t) &= \frac{-(t-1)(3t-2)(3t-1)}{2} \\
 N_1(t) &= \frac{9(t-1)t(3t-2)}{2} \\
 N_2(t) &= \frac{-9(t-1)t(3t-1)}{2} \\
 N_3(t) &= \frac{t(3t-2)(3t-1)}{2}
 \end{aligned}
 \tag{56}$$

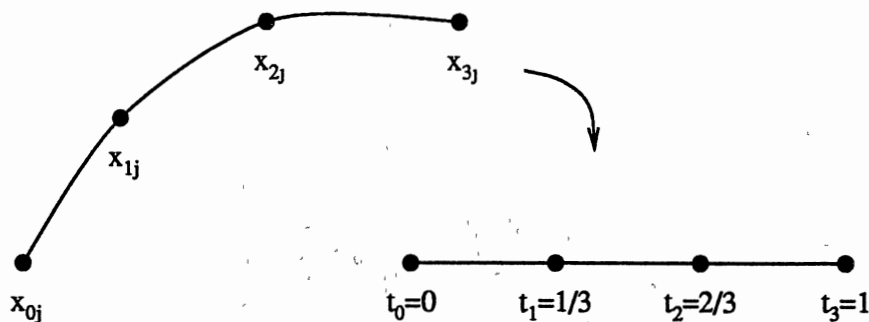


Figure 10. CUBIC Element Geometry and Parametric Mapping

### Overhauser (OVER) Element

As described in the previous sections, Lagrangian linear, quadratic, and cubic elements are commonly used in elastostatics. They provide only parametric positional ( $C^0$ ) continuity between elements. When the boundary geometry is linear, parametric derivative continuity ( $C^1$ ) between elements is satisfied; however, this is not the case when the boundary geometry is curved. The approximation of the displacements and tractions may also require derivative continuity between elements for accuracy. This is especially important in elastostatics because of its inherent dependence on a continuous strain field.  $C^1$  continuity is also desirable since the normal direction and hence the boundary stresses are the same as a node is approached from two different elements.

$C^1$  continuous curves have long been a subject of interest for many researchers, often in the context of computer-aided design. However, much of the research has

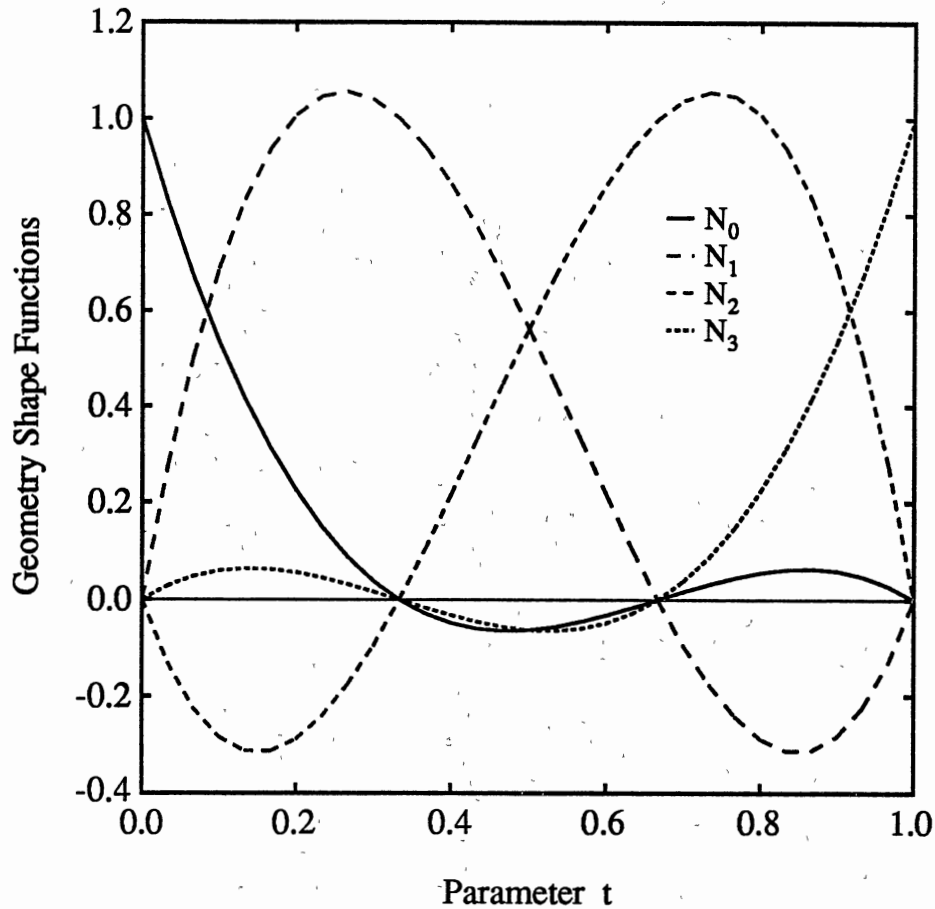


Figure 11. CUBIC Element Shape Functions

gone into developing  $C^1$  approximating curves [7] which produced surfaces for design. Watson [65,66] developed a hermitian cubic boundary element which requires the specification of positional and derivative data at each node. This requires the recasting of the boundary integrals described in Chapter III to include the derivative data. The  $C^1$  continuous curve should be an interpolating curve that requires only positional data. Overhauser [51] developed such a curve based on a parabolic blending technique which forms an interpolating parametric cubic by blending parametric

quadratics. Brewer and Anderson [12] developed a formulation for rapid computation which is described below. The use of the Overhauser element is described more extensively in [63]. The **OVER**hauser element will be abbreviated **OVER**.

The Overhauser curve  $c_j(t)$ , shown in Figure 12, is a linear blend of two overlapping parametric parabolas. The first parabola  $p_j(r)$  is defined by the three points,

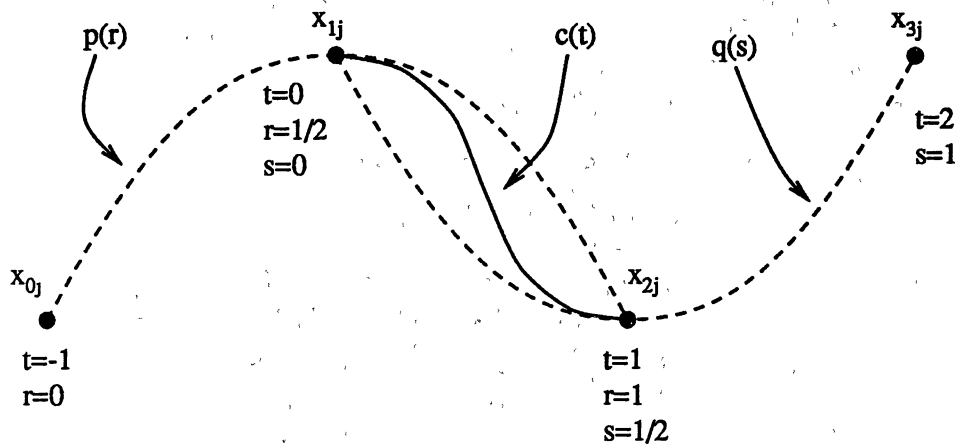


Figure 12. **OVER** Element Geometry and Parametric Mapping

$x_{0j}$ ,  $x_{1j}$ , and  $x_{2j}$ . The second parabola  $q_j(s)$  is defined by the three points,  $x_{1j}$ ,  $x_{2j}$ , and  $x_{3j}$ . If  $r$ ,  $s$ , and  $t$  are related in a linear manner

$$r = k_1 t + k_2 \quad (57)$$

$$s = k_3 t + k_4 \quad (58)$$

then  $c_j(t)$  is given by

$$c_j(t) = (1 - t)p_j(r) + tq_j(s) \quad (59)$$

$p_j(r)$  and  $q_j(s)$  are the quadratic curves

$$p_j(r) = N_0(r)x_{0j} + N_1(r)x_{1j} + N_2(r)x_{2j} \quad (60)$$

$$q_j(s) = N_1(s)x_{1j} + N_2(s)x_{2j} + N_3(s)x_{3j} \quad (61)$$

where the  $N_l$  are the quadratic shape functions

$$N_0(r) = (r - 1)(2r - 1) \quad N_1(r) = -4(r - 1)r \quad N_2(r) = r(2r - 1) \quad (62)$$

$$N_1(s) = (s - 1)(2s - 1) \quad N_2(s) = -4(s - 1)s \quad N_3(s) = s(2s - 1) \quad (63)$$

The relationship between  $r$  and  $t$  may be determined by evaluating Equation 57 at points  $x_{1j}$  and  $x_{2j}$

$$\frac{1}{2} = k_1 0 + k_2 \quad \text{and} \quad 1 = k_1 1 + k_2 \quad (64)$$

which yields

$$r = \frac{1}{2}t + \frac{1}{2} \quad (65)$$

The relationship between  $s$  and  $t$  may be determined by evaluating Equation 58 at points  $x_{1j}$  and  $x_{2j}$

$$0 = k_1 0 + k_2 \quad \text{and} \quad \frac{1}{2} = k_1 1 + k_2 \quad (66)$$



which yields

$$s = \frac{1}{2}t \quad (67)$$

Substituting Equations 60, 61, 62, 63, 65, and 67 into Equation 59 and simplifying yields the OVER element written in terms of shape functions

$$x_j(t) = N_0(t)x_{0j} + N_1(t)x_{1j} + N_2(t)x_{2j} + N_3(t)x_{3j} \quad (68)$$

where

$$\begin{aligned} N_0(t) &= \frac{-(t-1)^2t}{2} \\ N_1(t) &= \frac{(t-1)(3t^2 - 2t - 2)}{2} \\ N_2(t) &= \frac{-t(3t^2 - 4t - 1)}{2} \\ N_3(t) &= \frac{(t-1)t^2}{2} \end{aligned} \quad (69)$$

Note that the OVER element is only defined between  $x_{1j}$  and  $x_{2j}$ , as indicated by the solid line in Figure 12. However,  $x_{0j}$  and  $x_{3j}$  do give contributions to the element assembly matrix when the element is integrated. These shape functions are evaluated at the values of the parameter  $t$  corresponding to the node locations in Equation 70. Since the element is only defined over the interval  $0 \leq t \leq 1$ , the OVER shape

functions satisfy Equation 49. They also satisfy Equation 50.

$$\begin{aligned}
 t &= & -1 & 0 & 1 & 2 \\
 N_0(t) &= & 2 & 0 & 0 & -1 \\
 N_1(t) &= & -3 & 1 & 0 & 3 \\
 N_2(t) &= & 3 & 0 & 1 & -3 \\
 N_3(t) &= & -1 & 0 & 0 & 2
 \end{aligned}
 \tag{70}$$

The shape functions are plotted in Figure 13.

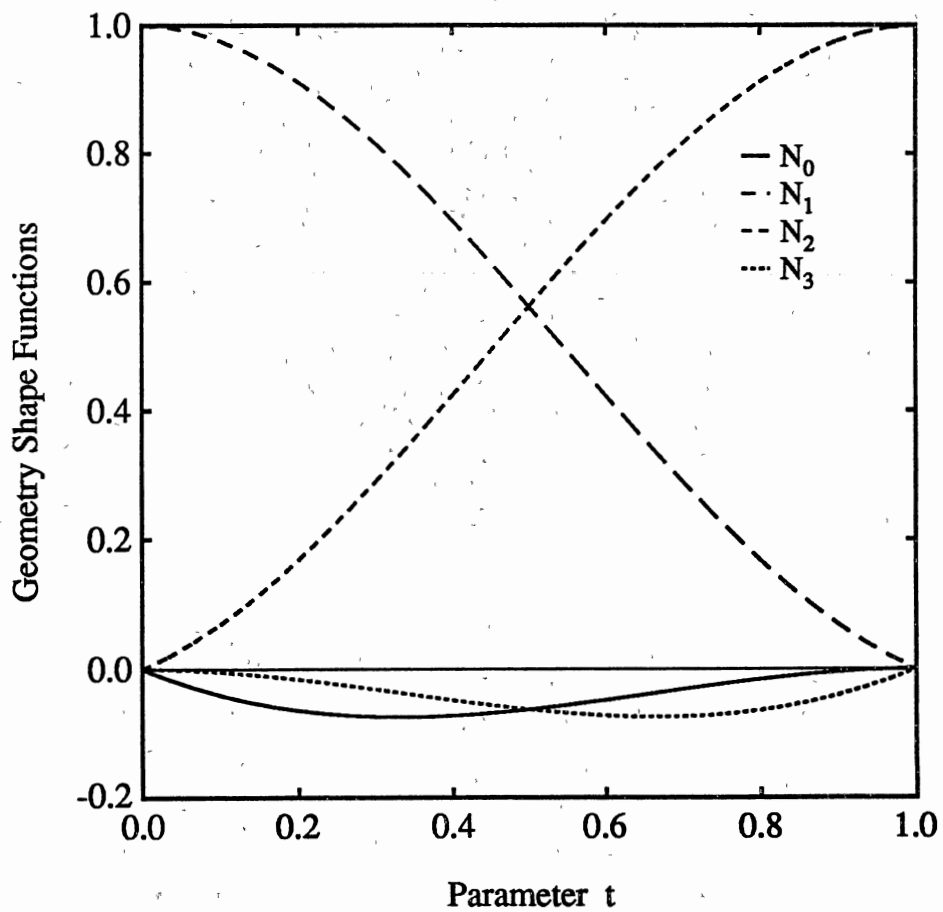


Figure 13. OVER Element Shape Functions

Derivative continuity between elements can be shown as follows. The curve may be differentiated with respect to  $t$ :

$$x'_j(t) = \frac{dx_j(t)}{dt} = N'_i(t)x_{i,j} = \frac{dN_i(t)}{dt}x_{i,j} \quad (71)$$

where

$$\begin{aligned} N'_0(t) &= \frac{-(t-1)(3t-1)}{2} \\ N'_1(t) &= \frac{t(9t-10)}{2} \\ N'_2(t) &= \frac{-(t-1)(9t+1)}{2} \\ N'_3(t) &= \frac{t(3t-2)}{2} \end{aligned} \quad (72)$$

Evaluating Equation 72 at the values of  $t$  corresponding to the node locations gives

$$\begin{aligned} t &= \quad -1 \quad 0 \quad 1 \quad 2 \\ N'_0(t) &= \quad -4 \quad \frac{-1}{2} \quad 0 \quad \frac{-5}{2} \\ N'_1(t) &= \quad \frac{19}{2} \quad 0 \quad \frac{-1}{2} \quad 8 \\ N'_2(t) &= \quad -8 \quad \frac{1}{2} \quad 0 \quad \frac{-19}{2} \\ N'_3(t) &= \quad \frac{5}{2} \quad 0 \quad \frac{1}{2} \quad 4 \end{aligned} \quad (73)$$

Given two overlapping OVER elements,  $A_j(t)$  defined by nodes  $x_{0j}$ ,  $x_{1j}$ ,  $x_{2j}$ , and  $x_{3j}$ , and  $B_j(t)$  defined by nodes  $x_{1j}$ ,  $x_{2j}$ ,  $x_{3j}$ , and  $x_{4j}$ , if  $A_j(t)$  is evaluated at  $t = 1$  and  $B_j(t)$  is evaluated at  $t = 0$ , we find that

$$A'_j(t = 1) = B'_j(t = 0) = -\frac{1}{2}x_{1j} + \frac{1}{2}x_{3j} \quad (74)$$

showing  $C^1$  continuity at node  $x_{2j}$  between elements  $A_j(t)$  and  $B_j(t)$ .

## Right Corner Overhauser

### (OVRR) Element

Since the OVER element is designed to have first derivative continuity between elements, problems occur when attempting to model the region near a corner (a geometric singularity). One method of modeling a corner is to make the nodes on one side of the element coincident. Unfortunately, excessive error is introduced into the element integration by this approach, since the element integration is nearly singular for the last node. Another approach taken in References [63,64] is to use cubic elements in the corners. However,  $C^1$  continuity is lost at the point where the OVER and CUBIC elements met.

The approach implemented here was originated by Hibbs [32]. Hibbs developed a corner element that has  $C^1$  continuity on one side and  $C^0$  continuity on the other. This can be achieved by performing a quadratic extrapolation for the point  $x_{3j}$  which is "missing" when compared to the OVER element (see Figure 14). This new element will be named OVRR which is short for OVeRhauser Right since the element terminates at its right-hand side. Referring to Figure 12, node  $x_{3j}$  may be extrapolated

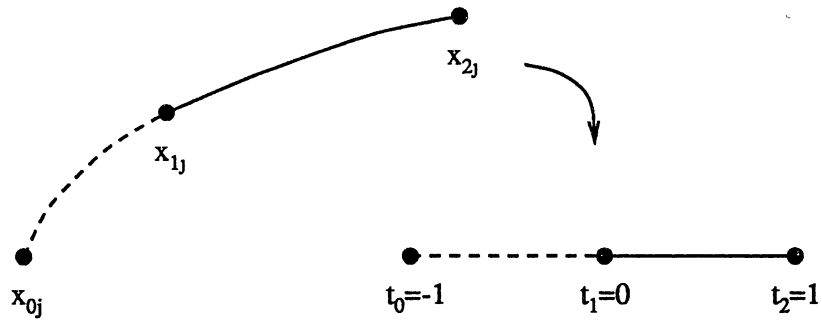


Figure 14. OVR Element Geometry and Parametric Mapping

by constructing a difference table:

$$\begin{array}{r}
 x_{0j} \\
 \\
 x_{1j} - x_{0j} \\
 \\
 x_{1j} \qquad x_{2j} - 2x_{1j} + x_{0j} \\
 \\
 x_{2j} - x_{1j} \qquad x_{3j} - 3x_{2j} + 3x_{1j} - x_{0j} \\
 \\
 x_{2j} \qquad x_{3j} - 2x_{2j} + x_{1j} \\
 \\
 x_{3j} - x_{2j} \\
 \\
 x_{3j}
 \end{array} \tag{75}$$

By assuming a zero difference,  $x_{3j}$  becomes

$$x_{3j} = 3x_{2j} - 3x_{1j} + x_{0j} \tag{76}$$

Substituting into Equations 68 and 69 and simplifying yields the new shape functions

$$\begin{aligned} N_0(t) &= \frac{(t-1)t}{2} \\ N_1(t) &= -(t-1)(t+1) \\ N_2(t) &= \frac{t(t+1)}{2} \end{aligned} \quad (77)$$

The shape functions are plotted in Figure 15. The shape functions may be evaluated

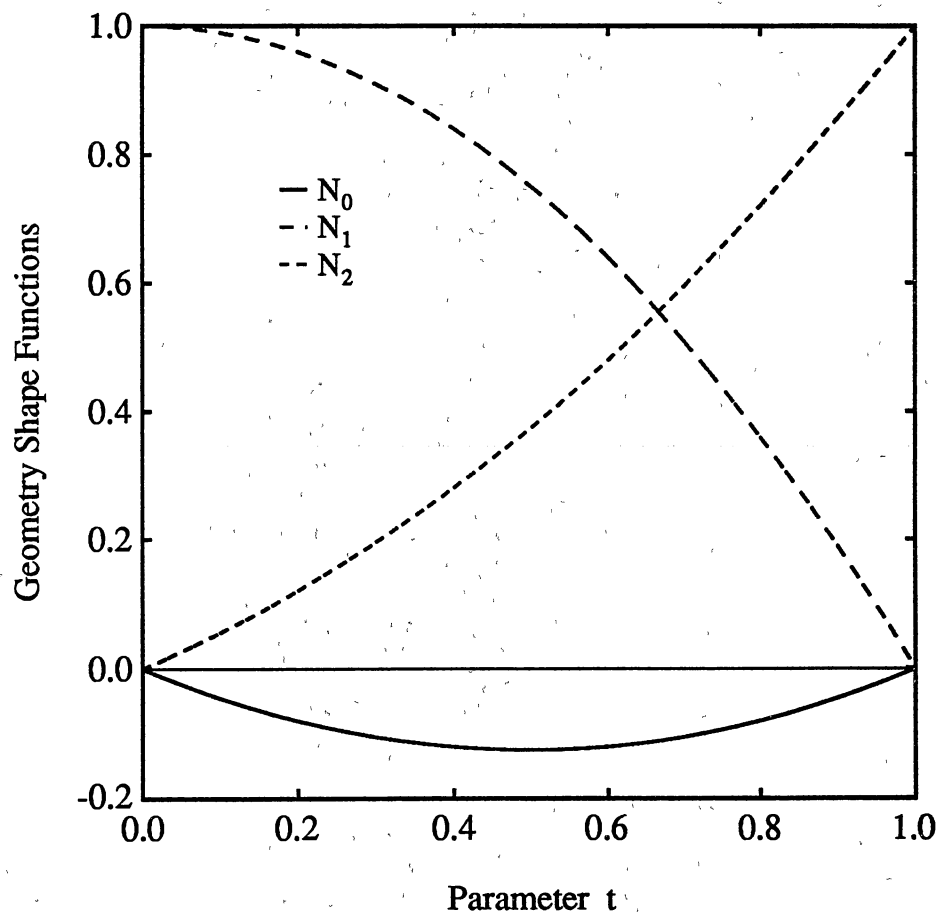


Figure 15. OVR Element Shape Functions

at the values of the parameter  $t$  which corresponds the the node locations.

$$\begin{aligned}
 t &= \quad -1 \quad 0 \quad 1 \\
 N_0(t) &= \quad 1 \quad 0 \quad 0 \\
 N_1(t) &= \quad 0 \quad 1 \quad 0 \\
 N_2(t) &= \quad 0 \quad 0 \quad 1
 \end{aligned} \tag{78}$$

Derivative continuity between the OVER element and the OVR element may be shown as follows. Differentiating the shape functions with respect to  $t$ ,

$$\begin{aligned}
 N'_0(t) &= \frac{(2t-1)}{2} \\
 N'_1(t) &= -2t \\
 N'_2(t) &= \frac{(2t+1)}{2}
 \end{aligned} \tag{79}$$

The shape functions may then be evaluated at the values of the parameter  $t$  which corresponds to the node locations.

$$\begin{aligned}
 t &= \quad -1 \quad 0 \quad 1 \\
 N'_0(t) &= \quad \frac{-3}{2} \quad \frac{-1}{2} \quad \frac{1}{2} \\
 N'_1(t) &= \quad 2 \quad 0 \quad -2 \\
 N'_2(t) &= \quad \frac{-1}{2} \quad \frac{1}{2} \quad \frac{3}{2}
 \end{aligned} \tag{80}$$

Given an OVER element  $A_j(t)$  defined by nodes  $x_{0j}$ ,  $x_{1j}$ ,  $x_{2j}$ , and  $x_{3j}$ , and an OVR element  $B_j(t)$  defined by nodes  $x_{1j}$ ,  $x_{2j}$ , and  $x_{3j}$ , if  $A_j(t)$  is evaluated at  $t = 1$  and

$B_j(t)$  is evaluated at  $t = 0$ , we find that

$$A'_j(t = 1) = B'_j(t = 0) = -\frac{1}{2}x_{1j} + \frac{1}{2}x_{3j}, \quad (81)$$

showing  $C^1$  continuity at node  $x_{2j}$  between elements  $A_j(t)$  and  $B_j(t)$ .

## Left Corner Overhauser

### (OVR) Element

The left corner Overhauser is similar to the OVR element with the exception that it has its  $C^0$  and  $C^1$  positions reversed. This element will be named OVR which is short for **O**Ver**R**hauser **L**eft since the element terminates at its left-hand side. The OVR element geometry and parametric mapping is shown in Figure 16. The OVR element may be derived in a manner similar to that of the OVR element.

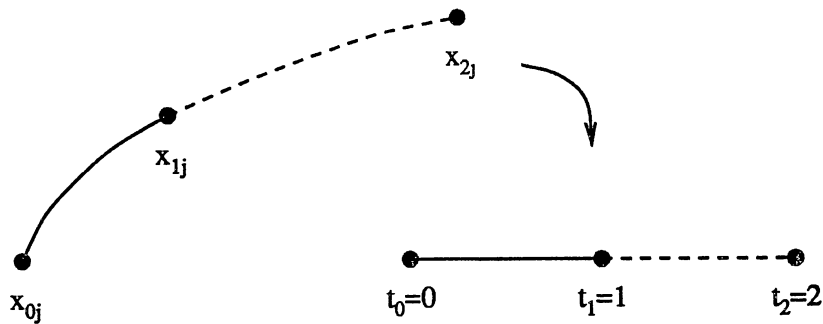


Figure 16. OVR Element Geometry and Parametric Mapping



The OVRL shape functions are given in Equation 82 and plotted in Figure 17:

$$\begin{aligned} N_0(t) &= \frac{(t-2)(t-1)}{2} \\ N_1(t) &= -(t-2)t \\ N_2(t) &= \frac{(t-1)t}{2} \end{aligned} \quad (82)$$

The shape functions may be evaluated at the values of the parameter  $t$  which corre-

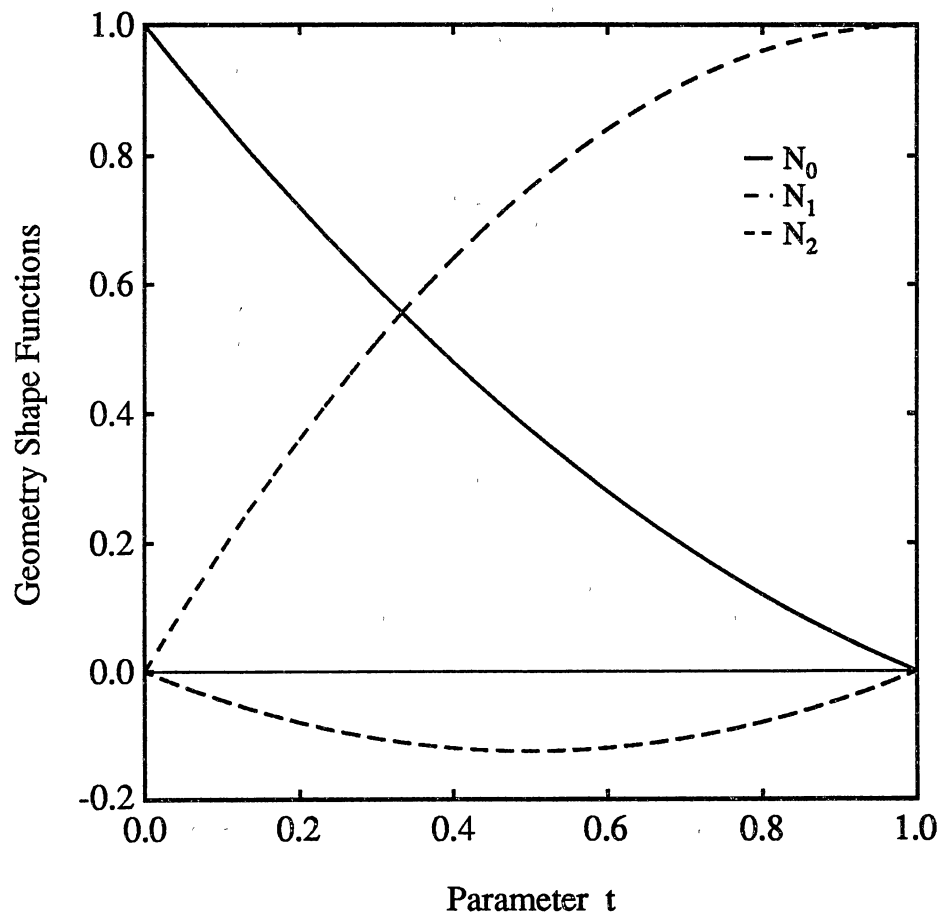


Figure 17. OVRL Element Shape Functions

sponds the the node locations.

$$\begin{aligned}
 t &= \quad 0 \quad 1 \quad 2 \\
 N_0(t) &= \quad 1 \quad 0 \quad 0 \\
 N_1(t) &= \quad 0 \quad 1 \quad 0 \\
 N_2(t) &= \quad 0 \quad 0 \quad 1
 \end{aligned} \tag{83}$$

$C^1$  continuity between OVER and OVRL element may be shown in a manner similar to that of OVER and OVRP by employing the following equations:

$$\begin{aligned}
 N'_0(t) &= \frac{(2t-3)}{2} \\
 N'_1(t) &= -2(t-1) \\
 N'_2(t) &= \frac{(2t-1)}{2}
 \end{aligned} \tag{84}$$

$$\begin{aligned}
 t &= \quad 0 \quad 1 \quad 2 \\
 N'_0(t) &= \quad \frac{-3}{2} \quad \frac{-1}{2} \quad \frac{1}{2} \\
 N'_1(t) &= \quad 2 \quad 0 \quad -2 \\
 N'_2(t) &= \quad \frac{-1}{2} \quad \frac{1}{2} \quad \frac{3}{2}
 \end{aligned} \tag{85}$$

### Integration

The integrations that must be performed over a single boundary element are

$$H_{ij}^e(\zeta, \eta) = \int_{\Gamma^e} p_{ij}^*(\zeta, \eta) N_i^u(\eta) d\Gamma^e \tag{86}$$

$$G_{ijl}^e(\zeta, \eta) = \int_{\Gamma^e} u_{ij}^*(\zeta, \eta) N_l^p(\eta) d\Gamma^e \quad (87)$$

These integrals are evaluated in the local coordinate system of the element. This may be accomplished with the Jacobian transformation

$$d\Gamma^e = J(t) dt \quad (88)$$

$$J(t) = \sqrt{\frac{dx_j(t)}{dt} \frac{dx_j(t)}{dt}} \quad (89)$$

$$\frac{dx_j(t)}{dt} = \frac{dN_l^g(t)}{dt} x_{lj} \quad (90)$$

where  $t$  is the local parametric coordinate which varies from 0 to 1 along the element.

The normal to the element is calculated by

$$\begin{aligned} n_0 &= \frac{dx_1(t)}{dt} / J(t) \\ n_1 &= -\frac{dx_0(t)}{dt} / J(t) \end{aligned} \quad (91)$$

Substituting

$$H_{ijl}^e(\zeta, t) = \int_0^1 p_{ij}^*(r_j(\zeta, t)) N_l^u(t) J(t) dt \quad (92)$$

$$G_{ijl}^e(\zeta, t) = \int_0^1 u_{ij}^*(r_j(\zeta, t)) N_l^p(t) J(t) dt \quad (93)$$

where the  $\zeta$  shows that the fundamental solution is also a function of the source node position. The radius vector is calculated by

$$r_j(\zeta, t) = x_j(t) - x_j(\zeta) \quad (94)$$

$$x_j(t) = N_l^g(t) x_{lj} \quad (95)$$

These integrations can be performed using standard Gaussian quadrature formulas [58]:

$$H_{ijl}^e(\zeta, t) \approx \sum_{q=1}^Q p_{ij}^*(r_j(\zeta, t_q)) N_l^u(t_q) J(t_q) w_q \quad (96)$$

$$G_{ijl}^e(\zeta, t) \approx \sum_{q=1}^Q u_{ij}^*(r_j(\zeta, t_q)) N_l^p(t_q) J(t_q) w_q \quad (97)$$

where  $t_q$  are the quadrature points,  $w_q$  are the quadrature weights, and  $Q$  is the number of quadrature points and weights.

### Singular Integration

If the source node belongs to the element which is being integrated, then the two dimensional fundamental solution becomes singular when  $r(\zeta, t) = 0$  (i.e., when  $x_j(t) = x_j(\zeta)$  the source node and field node are the same). Equation 92 then has a singularity on the order of

$$H_{ijl}^e(\zeta, t) = O\left(\int \frac{1}{r(\zeta, t)} N_l^u(t) J(t) dt\right) \quad (98)$$

The shape functions which do not correspond to the source node are zero at the singular point, thereby canceling the singularity in the denominator. The shape function which corresponds to the source node has a value of one at the singular point and the singularity is not canceled. But this term can be calculated by the rigid body motion equation (Equation 29) and is therefore not needed. Equation 93

has a singular integrand on the order of

$$G_{iji}^e(\zeta, t) = O \left( \int \ln(r(\zeta, t)) N_i^p(t) J(t) dt \right) \quad (99)$$

and it must be calculated. One approach is to break the integral up into a sum of a singular part and a nonsingular part. The nonsingular part is integrated using standard quadrature as outlined in the previous section.

The key to the singular integration is recognizing that if  $r(\zeta, t)$  is expanded in terms of the shape functions and  $t$ , the result will be a function in which all powers of  $t$  are greater than or equal to  $t^2$ . A  $t^2$  can be factored out of the expression for  $r$  and  $\ln(r)$ , then broken into a sum. The  $\ln(t)$  term is integrated using a special natural log quadrature [58] and the remainder using standard quadrature as outlined in the previous section.

A general approach, for any element type, to singular integration is as follows. After mapping the shape function of the element to one or more sections such that  $t = 0$  at the source node, the shape functions may be factored such that

$$N_i^q(t) = T_m(t) M_{mi} \quad (100)$$

where  $T_m(t)$  is a vector that contains powers of  $t$ , and  $M_{mi}$  is a matrix of constant coefficients. The coordinates of the field node may then be written

$$x_j(t) = T_m(t) M_{mj} x_{lj} \quad (101)$$

and  $r_j$  becomes, with  $B_{mj} = M_{mi}x_{lj}$

$$r_j(\zeta, t) = T_m(t)B_{mj} - 1 x_j(\zeta) \quad (102)$$

Recognizing that  $T_m$  always has a constant 1 in its  $m$  position, we can perform the source node subtraction from the  $m$  position only of  $B_{mj}$

$$C_{mj}(\zeta) = B_{mj} - x_j(\zeta) \quad \textit{position m only} \quad (103)$$

Let

$$P_j(\zeta, t) = T_m(t)C_{mj}(\zeta) \quad (104)$$

be the resultant polynomial in  $t$ . The square of the radius vector becomes

$$[r_j(\zeta, t)]^2 = [P_j(\zeta, t)]^2 = t^2[P'_j(\zeta, t)]^2 \quad (105)$$

and  $[P'_j(\zeta, t)]^2$  may be evaluated in the following manner. The square of the polynomial is performed by a general polynomial multiplication scheme [41], which multiplies the coefficients of the polynomial and does not require its actual evaluation. The scheme is as follows where the subscripts in the following three equations indicate polynomial coefficients and not summation indices. If there are two polynomials

$$u(t) = u_r t^r + \dots + u_1 t + u_0 \quad \textit{and} \quad v(t) = v_s t^s + \dots + v_1 t + v_0 \quad (106)$$

then their product is

$$u(t)v(t) = w_{r+s}t^{r+s} + \dots + w_0 \quad (107)$$

where

$$w_k = u_0v_k + u_1v_{k-1} + \dots + u_{k-1}v_1 + u_kv_0 \quad (108)$$

and  $u_i$  or  $v_j$  are treated as zero if  $i > r$  or  $j > s$ . Hence we can perform the square of the coefficients of a polynomial and delay evaluating at powers of  $t$  until a later step. Since

$$r^2 = r_j r_j \quad (109)$$

and the powers of  $t$  in  $P'_j(\zeta, t)$  are the same for all coordinate directions, the squared polynomial coefficients from the general polynomial multiplication for each coordinate direction may be added together to get  $P'(\zeta, t)$ . By Horner's rule, the polynomial evaluation in powers of  $t$  must be performed only once. While this singular log quadrature approach is fairly common, the general approach, for any element type, taken here is fairly unique.

Finally, we can rewrite Equations 13 and 93 as

$$u_{ij}^*(\zeta, t) = u_{i_j A}^*(\zeta, t) + u_{i_j B}^*(t) \quad (110)$$

where

$$u_{i_j A}^*(\zeta, t) = \frac{-1}{8\pi(1-\nu)\mu} \left[ (3-4\nu)\frac{1}{2} \ln(P'(\zeta, t))\delta_{ij} - r_{,i}(\zeta, t)r_{,j}(\zeta, t) \right] \quad (111)$$

$$u_{i_j B}^*(t) = \frac{-1}{8\pi(1-\nu)\mu} (3-4\nu) \ln(t) \delta_{ij} \quad (112)$$

and

$$G_{i_j l}^e(\zeta, t) = \int_0^1 u_{i_j A}^*(r_j(\zeta, t)) N_l^p(t) J(t) dt + \int_0^1 u_{i_j B}^*(t) N_l^p(t) J(t) dt \quad (113)$$



# Chapter V

## TWO DIMENSIONAL CRACK TIP BOUNDARY ELEMENTS

All of the two dimensional crack tip boundary elements will be derived in this chapter. The methods for integration and stress intensity factor calculation will also be examined. The following element types will be examined

- Quadratic Quarter Point Crack Tip (CTQQ)
- Quadratic Traction Singular Quarter Point Crack Tip (CTQT)
- Quadratic Crack Tip (CTQUA)
- Overhauser Crack Tip (CTOVR)

The first element types, CTQQ and CTQT, which are based on the QUAD element shape functions, achieve their modeling of the stress singularity at the crack tip by moving the middle node from its normal  $t = \frac{1}{2}$  position to the  $t = \frac{1}{4}$  position. The CTQT element type models the  $1/\sqrt{r}$  traction singularity while the CTQQ element type does not. The last element types, CTQUA and CTOVR, model the singularity properly in the shape functions themselves. The normal and singular integrations and SIF of the various elements will be described after all elements have been described.

## Quadratic Quarter Point Crack Tip

### (CTQQ) Element

The Quadratic Quarter point Crack Tip element will be abbreviated CTQQ. The geometry, displacement, and traction shape functions and shape function plots for the CTQQ element are the same as those for the QUAD element. The  $\sqrt{r}$  singularity in the displacement shape functions at the crack tip is achieved by moving the middle node to the  $t = \frac{1}{4}$  position from its typical  $t = \frac{1}{2}$  position, where  $t$  is the parameter along the element. Hence, this is the simplest crack tip element, since no additional programming is required. The  $\sqrt{r}$  singularity may be shown in the following manner.

Evaluation of the QUAD element shape functions

$$u_j(t) = N_i^u(t)u_{i_j} \quad (114)$$

$$N_0^u(t) = (t-1)(2t-1)$$

$$N_1^u(t) = -4(t-1)t \quad (115)$$

$$N_2^u(t) = t(2t-1)$$

at

$$u_{0j} = \langle 0 \quad 0 \rangle$$

$$u_{1j} = \langle \frac{L}{4} \quad 0 \rangle \quad (116)$$

$$u_{2j} = \langle L \quad 0 \rangle$$

where  $L$  is the length of the element in real space, yields

$$u = -4(t-1)t\frac{L}{4} + t(2t-1)L \quad (117)$$

which simplifies to

$$t = \sqrt{\frac{u}{L}} \quad \text{or} \quad u = t^2L \quad (118)$$

Finally, the Jacobian vanishes at  $t = 0$  (or equivalently at  $u = 0$ )

$$J(t) = \frac{du}{dt} = 2tL = 2\sqrt{uL} \quad (119)$$

## Quadratic Traction Singular Quarter

### Point Crack Tip (CTQT) Element

The Quadratic Traction singular quarter point Crack Tip element will be abbreviated CTQT. The geometry and displacement shape functions and shape function plots for the CTQT element are the same as those for the QUAD element. The  $\sqrt{r}$  singularity in the displacement shape functions is achieved in the same manner as that for the CTQQ element, by moving the middle node to the  $t = \frac{1}{4}$  position from its typical  $t = \frac{1}{2}$  position. The traction shape functions need a  $1/\sqrt{r}$  singularity at the crack tip. Dividing Equation 115 by

$$t = \sqrt{\frac{P}{L}} \quad (120)$$

the proper singularity is achieved:

$$\begin{aligned} N_0^P(t) &= 2t + \frac{1}{t} - 3 \\ N_1^P(t) &= -4(t - 1) \\ N_2^P(t) &= 2t - 1 \end{aligned} \tag{121}$$

The traction shape functions are plotted in Figure 18. Evaluating the shape functions

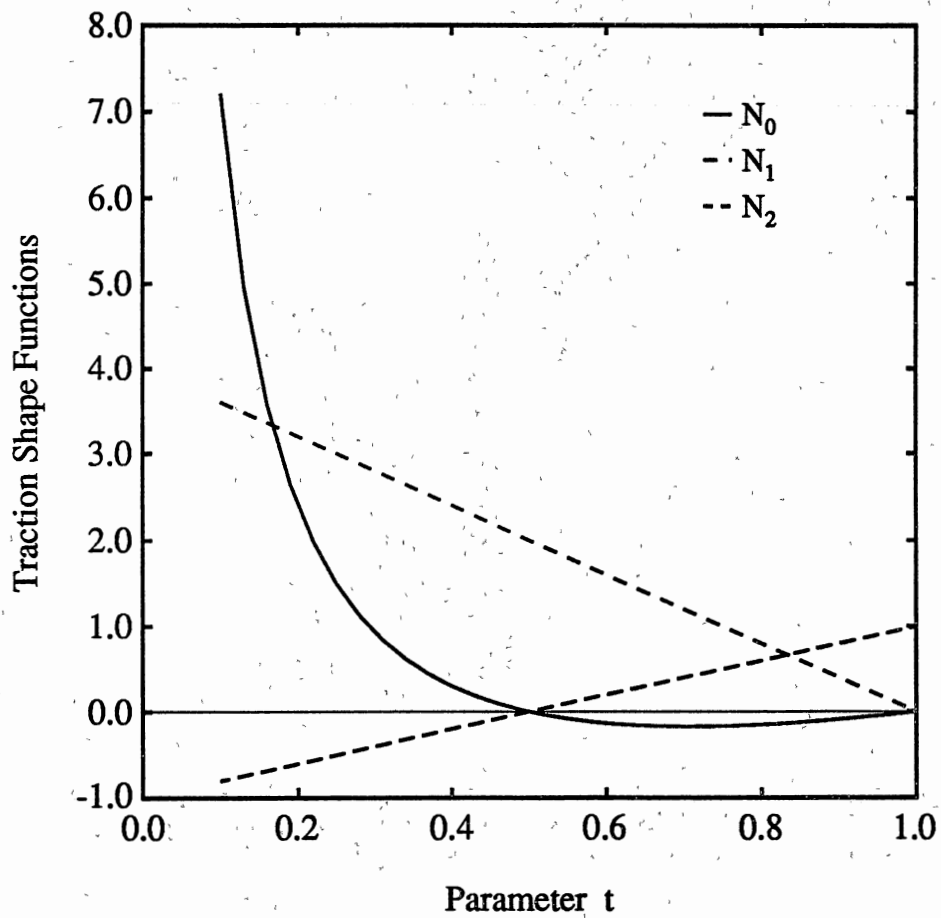


Figure 18. CTQT Element Traction Shape Functions

at several values of  $t$  corresponding to the nodes  $x_{0j}$ ,  $x_{1j}$  and  $x_{2j}$  (of course  $N_0^P(0) =$

$\infty$ , therefore a value is chosen that is close to  $t = 0$ )

$$\begin{aligned}
 t &= \quad \frac{1}{100} \quad \frac{1}{2} \quad 1 \\
 N_0^p(t) &= \quad 97.02 \quad 0.0 \quad 0.0 \\
 N_1^p(t) &= \quad 3.96 \quad 2.0 \quad 0.0 \\
 N_2^p(t) &= \quad -0.98 \quad 0.0 \quad 1.0
 \end{aligned} \tag{122}$$

From this evaluation, it can be seen that the shape functions satisfy Equation 49 only at node 2. Also, as shown in Equation 123, Equation 50 is no longer satisfied

$$\sum_{l=0}^n N_l^p(t) = \frac{1}{t} \tag{123}$$

## Quadratic Crack Tip (CTQUA) Element

The QUAdratic Crack Tip element will be abbreviated CTQUA. This type of shape function was originated by Luchi and Poggialini [42] and used in a two dimensional context by Jia, Shippy, and Rizzo [35]. Their innovation was to build the proper modeling of the  $\sqrt{r}$  singularity into the displacement shape functions and  $1/\sqrt{r}$  into the traction shape functions while leaving the middle node in its usual  $t = \frac{1}{2}$  position. The geometry shape functions are the same as the ones for the QUAD element. The element is defined by three nodes as shown in Figure 19 where the crack tip is at the  $x_{0j}$  node. When the crack tip is at node  $x_{2j}$ , the nodes may be mapped in real space prior to their integration. Essentially, this entails reversing

the order of the nodes within the element and changing the sign of the normal.

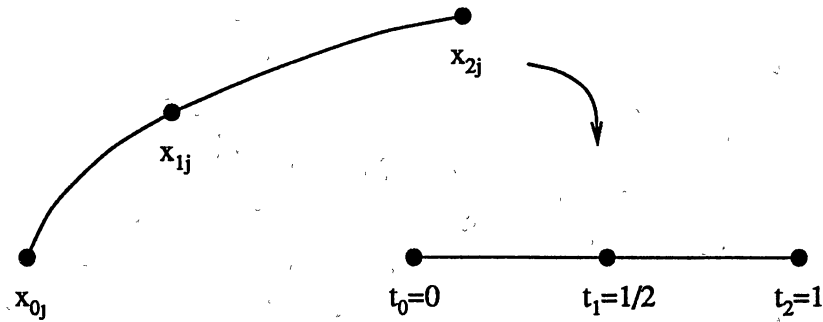


Figure 19. CTQUA Element Geometry and Parametric Mapping

The CTQUA displacement shape functions are derived directly using Equations 47 and 124.

$$n = 2$$

$$\xi = \sqrt{t} \quad (124)$$

$$\xi_m = \sqrt{t_m} = \langle 0 \quad \frac{1}{\sqrt{2}} \quad 1 \rangle$$

The CTQUA shape functions are given in Equation 125 and plotted in Figure 20.

They satisfy Equations 49 and 50.

$$\begin{aligned} N_0^u(t) &= \sqrt{2}t - (\sqrt{2} + 1)\sqrt{t} + 1 \\ N_1^u(t) &= 2(\sqrt{2} + 1)\sqrt{t} - 2(\sqrt{2} + 1)t \\ N_2^u(t) &= (\sqrt{2} + 2)t - (\sqrt{2} + 1)\sqrt{t} \end{aligned} \quad (125)$$

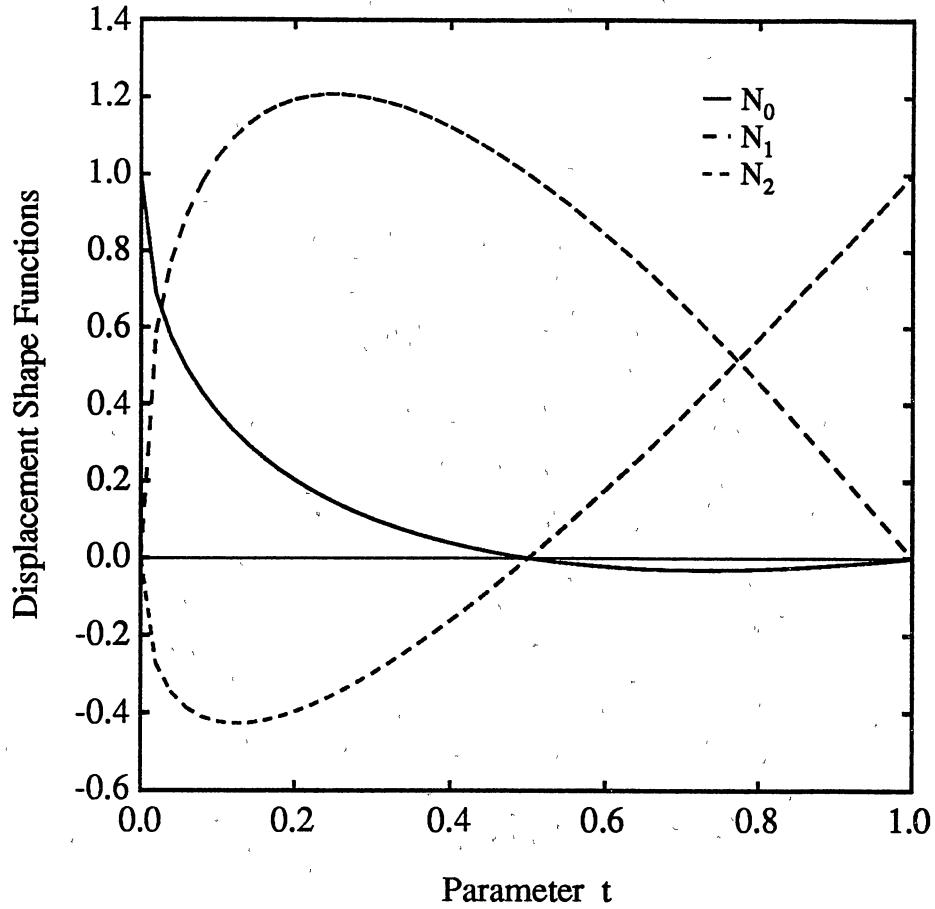


Figure 20. CTQUA Displacement Shape Functions

The CTQUA traction shape functions may be derived from the CTQUA displacement shape functions by dividing them by  $\sqrt{ct}$ , where  $c$  is a constant. Note that the only requirement on these shape functions is that they have the  $1/\sqrt{r}$  singularity:

$$\begin{aligned}
 N_0^p(t) &= N_0^u(t)/\sqrt{2t} \\
 N_1^p(t) &= N_1^u(t)/\sqrt{2t} \\
 N_2^p(t) &= N_2^u(t)/\sqrt{t}
 \end{aligned}
 \tag{126}$$

The CTQUA traction shape functions are given in Equation 127 and are plotted in

Figure 21:

$$\begin{aligned}
 N_0^p(t) &= \sqrt{t} + \frac{1}{(\sqrt{2t})} - \frac{(\sqrt{2} + 1)}{\sqrt{2}} \\
 N_1^p(t) &= \sqrt{2}(\sqrt{2} + 1)(1 - \sqrt{t}) \\
 N_2^p(t) &= (\sqrt{2} + 2)\sqrt{t} - \sqrt{2} - 1
 \end{aligned}
 \tag{127}$$

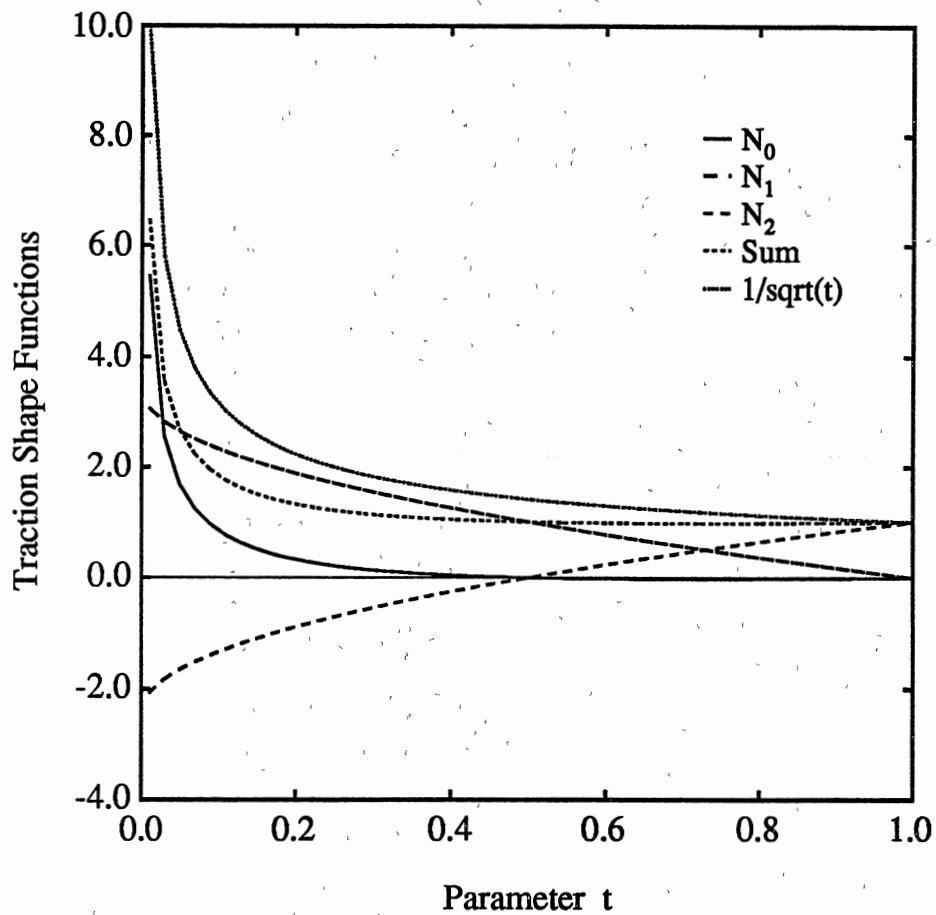


Figure 21. CTQUA Traction Shape Functions

Evaluation at various values of the parameter  $t$  shows that the traction shape functions satisfy Equation 49 at nodes  $x_{1j}$  and  $x_{2j}$ , and that Equation 50 is no longer



satisfied.

$$\begin{aligned}
 t &= \quad \frac{1}{100} \quad \frac{1}{2} \quad 1 \\
 N_0^p(t) &= \quad 5.464 \quad 0.0 \quad 0.0 \\
 N_1^p(t) &= \quad 3.073 \quad 1.0 \quad 0.0 \\
 N_2^p(t) &= \quad -2.073 \quad 0.0 \quad 1.0
 \end{aligned} \tag{128}$$

$$\sum_{i=0}^n N_i^p(t) = \sqrt{t} + \frac{1}{\sqrt{2t}} - \frac{1}{\sqrt{2}} \tag{129}$$

### Overhauser Crack Tip (CTOVR) Element

The OVerhauser Crack Tip element will be abbreviated CTOVR. The idea was to build the proper modeling of the  $\sqrt{r}$  singularity into the displacement shape functions and  $1/\sqrt{r}$  singularity into the traction shape functions at the crack tip end of the element. At the same time, the CTOVR element leaves the middle node in its usual position and provides  $C^1$  continuity at the other end with all of the other Overhauser element types. The CTOVR element also lays the foundation for the three dimensional elements derived from this type.

The element is defined by three nodes as shown in Figure 22 where the crack tip is at the  $x_{0j}$  node. The geometry shape functions are the same as the ones for the OVR element and are repeated here for convenience in Equation 130. The geometry

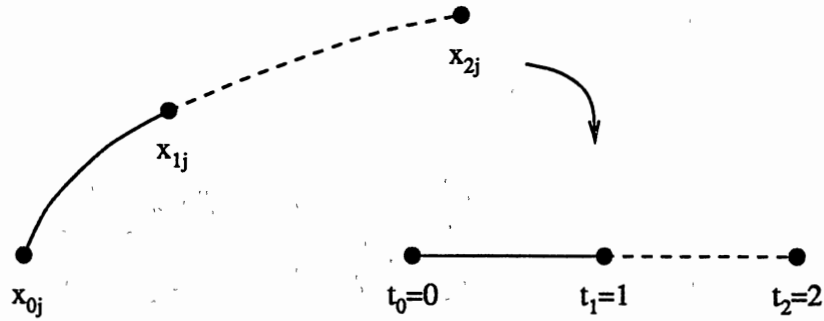


Figure 22. CTOVR Element Geometry and Parametric Mapping

shape functions are plotted in Figure 23.

$$\begin{aligned}
 N_0^g(t) &= \frac{(t-2)(t-1)}{2} \\
 N_1^g(t) &= -(t-2)t \\
 N_2^g(t) &= \frac{(t-1)t}{2}
 \end{aligned} \tag{130}$$

The CTOVR displacement shape functions could be derived using a simultaneous equation approach by evaluating Equation 131 at the desired values of  $t$ :

$$\begin{aligned}
 N_i^u(t) &= a_3 t^{\left(\frac{3}{2}\right)} + a_2 t + a_1 \sqrt{t} + a_0 \\
 N_i^{u'}(t) &= \frac{dN_i^u(t)}{dt} = 3 \frac{a_3 \sqrt{t}}{2} + \frac{a_1}{(2\sqrt{t})} + a_2
 \end{aligned} \tag{131}$$

However, the derivative equation is undefined at  $t = 0$ ; therefore, the coefficients will be solved for in the range of  $1 \leq t \leq 2$  as shown in Equation 132 and then the shape

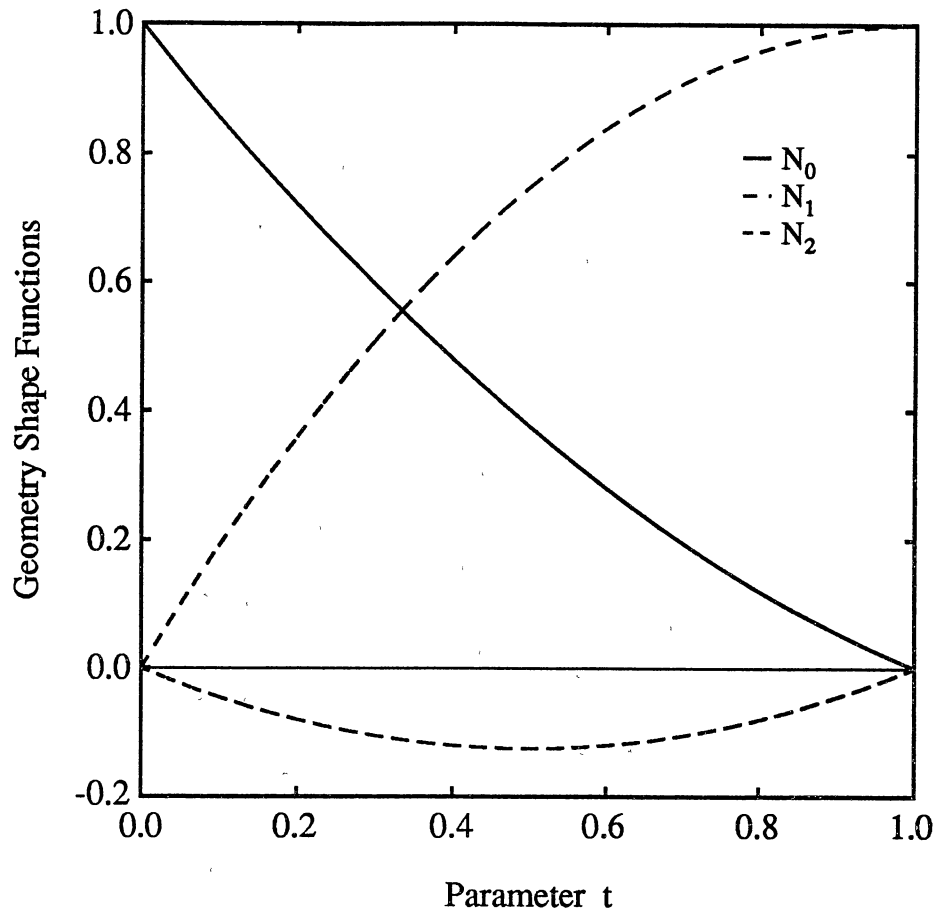


Figure 23. CTOVR Geometry Shape Functions

functions will be mapped back into the desired range of  $0 \leq t \leq 1$  by letting  $t = t+1$ .

$$\begin{aligned}
 t &= & 1 & 2 \\
 N_0^u(t) &= & 1 & 0 \\
 N_1^u(t) &= & 0 & 1 \\
 N_2^u(t) &= & 0 & 0 \\
 N_0^{u'}(t) &= & -\frac{3}{2} & -\frac{1}{2} \\
 N_1^{u'}(t) &= & 2 & 0 \\
 N_2^{u'}(t) &= & -\frac{1}{2} & \frac{1}{2}
 \end{aligned} \tag{132}$$

which, after solution and substitution of  $t = t + 1$ , yield the CTOVR displacement shape functions, given in Equation 133 and plotted in Figure 24:

$$\begin{aligned}
 N_0^u(t) &= \sqrt{t+1}((\sqrt{2}+1)(t+1) + \sqrt{2}+2) - 2(\sqrt{2}+2)(t+1) + 2 \\
 N_1^u(t) &= \sqrt{t+1}(-2(\sqrt{2}+1)(t+1) - 2(\sqrt{2}+2)) + (4\sqrt{2}+7)(t+1) - 1 \quad (133) \\
 N_2^u(t) &= \sqrt{t+1}((\sqrt{2}+1)(t+1) + \sqrt{2}+2) - (2\sqrt{2}+3)(t+1)
 \end{aligned}$$

An evaluation at several values of  $t$  shows that  $N_0^u(t)$  and  $N_1^u(t)$  satisfy Equation 50;

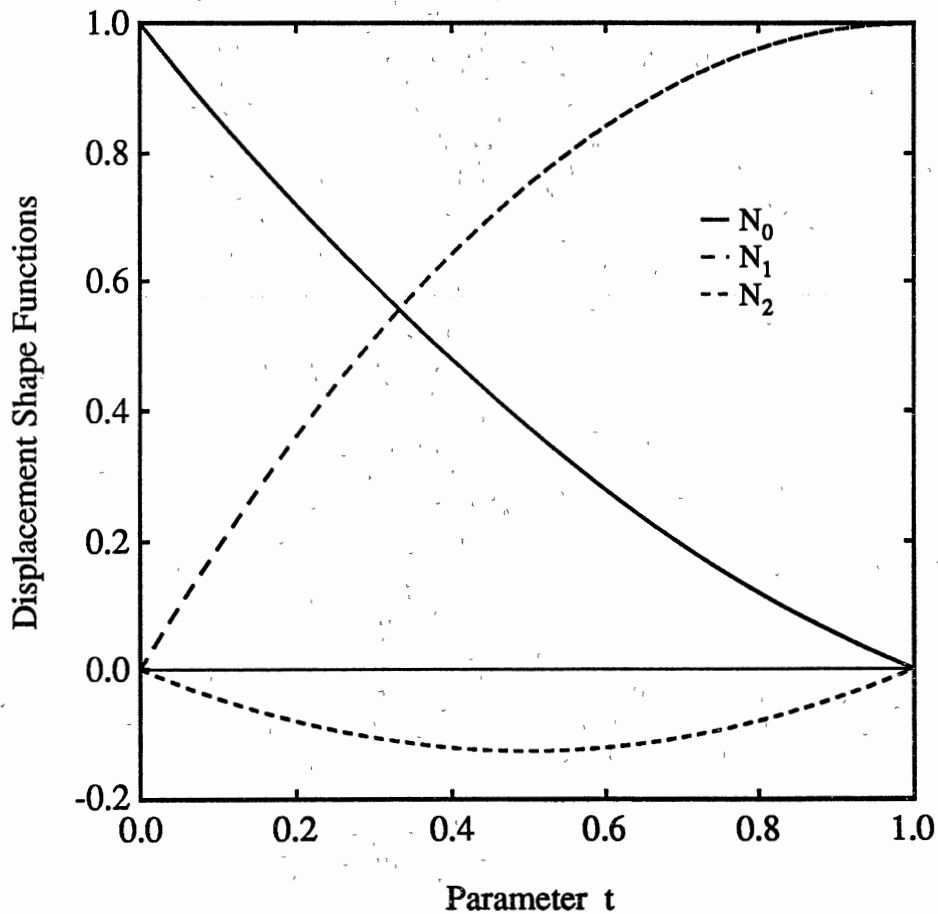


Figure 24. CTOVR Displacement Shape Functions

however,  $N_2^u(t)$  does not. They also satisfy Equation 49.

$$\begin{aligned}
 t = & \quad 0 \quad 1 \quad 2 \\
 N_0^u(t) = & \quad 1.0 \quad 0.0 \quad -2.707 \times 10^{-2} \\
 N_1^u(t) = & \quad 0.0 \quad 1.0 \quad 5.414 \times 10^{-2} \\
 N_2^u(t) = & \quad 0.0 \quad 0.0 \quad 0.9729
 \end{aligned} \tag{134}$$

After differentiating Equation 133 and evaluating at several values of  $t$ , it can be seen that the CTOVR displacement shape functions have first derivative continuity with the Overhauser family of elements in Equations 74 and 81 at the position  $t = 1$ :

$$\begin{aligned}
 t = & \quad 0 \quad 1 \quad 2 \\
 N_0^{u'}(t) = & \quad -1.5 \quad -0.5 \quad 0.4295 \\
 N_1^{u'}(t) = & \quad 2.0 \quad 0.0 \quad -1.859 \\
 N_2^{u'}(t) = & \quad -0.5 \quad 0.5 \quad 1.43
 \end{aligned} \tag{135}$$

The CTOVR traction shape functions may be derived in a manner similar to that used for derivation of the CTOVR displacement shape functions as shown in

Equation 136.

$$\begin{aligned}
 t &= & 1 & 2 \\
 N_0^u(t) &= & 1 & 0 \\
 N_1^u(t) &= & 0 & 1 \\
 N_2^u(t) &= & 0 & 0 \\
 N_0^{u'}(t) &= & -\frac{3}{2} & -\frac{1}{2} \\
 N_1^{u'}(t) &= & 2 & \frac{1}{2} \\
 N_2^{u'}(t) &= & -\frac{1}{2} & \frac{1}{2}
 \end{aligned} \tag{136}$$

After solution and substitution of  $t = t + 1$ , the displacement shape functions yield the CTOVR traction shape functions, given in Equation 137 and plotted in Figure 25.

$$\begin{aligned}
 N_0^p(t) &= \frac{(\sqrt{t+1}((\sqrt{2}+1)(t+1) + \sqrt{2}+2) - 2(\sqrt{2}+2)(t+1) + 2)}{\sqrt{t}} \\
 N_1^p(t) &= \frac{(\sqrt{t+1}((\sqrt{2}+2)(t+1) + 3(3\sqrt{2}+4)) - (6\sqrt{2}+7)(t+1) - 4\sqrt{2}-7)}{\sqrt{t}} \\
 N_2^p(t) &= \frac{(\sqrt{t+1}((\sqrt{2}+1)(t+1) + \sqrt{2}+2) - (2\sqrt{2}+3)(t+1))}{\sqrt{t}}
 \end{aligned} \tag{137}$$

Evaluation at various values of the parameter  $t$  shows that the traction shape functions satisfy Equation 49 at nodes  $x_{1j}$  and  $x_{2j}$  and that Equation 50 is no longer satisfied.

$$\begin{aligned}
 t &= & \frac{1}{100} & 1 & 2 \\
 N_0^p(t) &= & 9.851 & 0.0 & -1.914 \times 10^{-2} \\
 N_1^p(t) &= & 0.1982 & 1.0 & 1.031 \\
 N_2^p(t) &= & -4.952 \times 10^{-2} & 0.0 & 0.688
 \end{aligned} \tag{138}$$

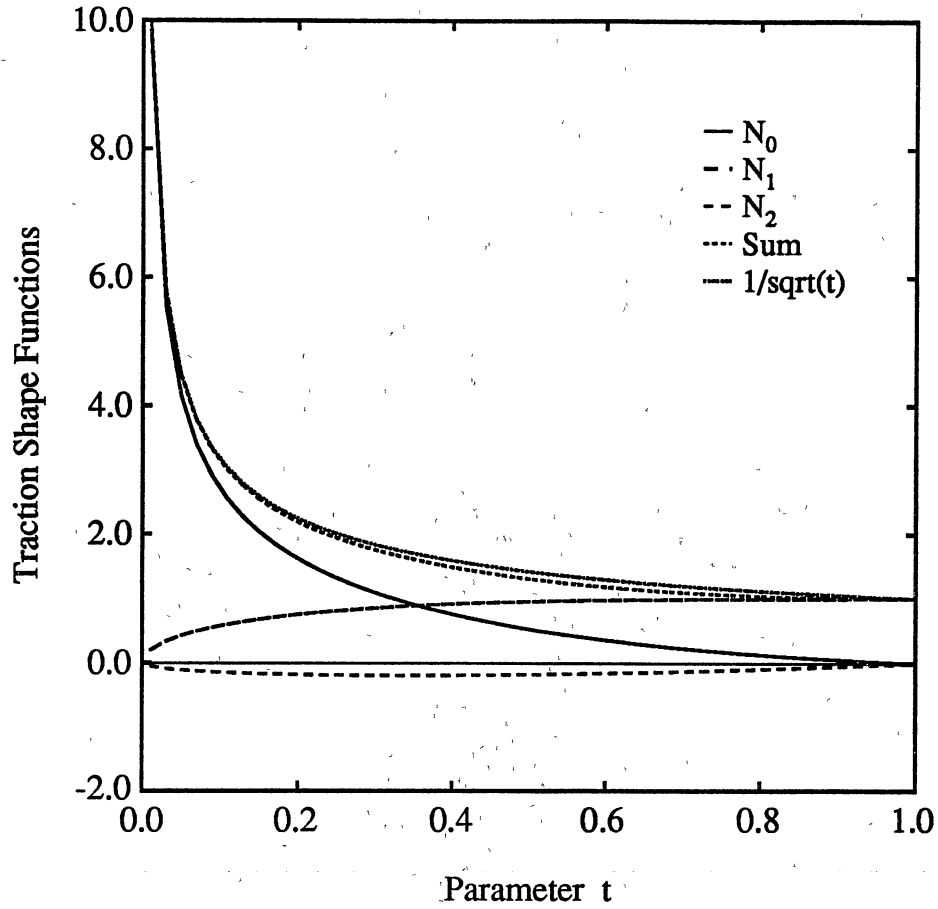


Figure 25. CTOVR Traction Shape Functions

$$\sum_{i=0}^n N_i^p(t) = (\sqrt{t+1}((3\sqrt{2}+4)t + 14\sqrt{2} + 20) + (-10\sqrt{2} - 14)t - 14\sqrt{2} - 19) \quad (139)$$

After differentiating Equation 137 and evaluating at several values of  $t$ , it can be seen that the CTOVR traction shape functions have first derivative continuity with

the Overhauser family of elements in Equations 74 and 81 at the position  $t = 1$ .

$$\begin{aligned}
 t &= && \frac{1}{100} & 1 & 2 \\
 N_0^p(t) &= && -507.4 & -0.5 & 0.3085 \\
 N_1^p(t) &= && 9.732 & 0.0 & 0.1124 \\
 N_2^p(t) &= && -2.428 & 0.5 & 0.8388
 \end{aligned} \tag{140}$$

### Integration

The integrations for the two dimensional crack tip boundary elements are generally performed in the same manner as those for the standard two dimensional boundary elements (Chapter IV). However, Equation 93 has a singular integrand at  $t = 0$  on the order of  $\frac{1}{\sqrt{t}}$  as shown ( $r(\zeta, t)$  does not go to zero here).

$$G_{i,jl}^e(\zeta, t) = O \left( \int_0^1 \frac{\ln(r(\zeta, t))}{\sqrt{t}} N_l^p(t) J(t) dt \right) \tag{141}$$

Because the integral itself exists in the ordinary sense, the singularity may be eliminated by an appropriate mapping of  $t$ . The required mapping is

$$t = \xi^4 \quad dt = 4\xi^3 d\xi \tag{142}$$

This same mapping may be applied to Equation 92 without detrimental effect. The integration for the right type crack tip elements may be performed by reversing the nodes within the element and changing the direction of the normal to the element.



## Singular Integration

Singular integrations for the CTQQ and CTQT element types are performed in the same manner as those for standard two dimensional boundary elements (Chapter IV). Although this is incorrect for the CTQT element, the error introduced was apparently ignored in several early works [25,8,46]. The singular integrations for the two dimensional crack tip boundary elements CTQUA and CTOVR, are *much* more involved than those for the standard two dimensional boundary elements.

The traction shape functions may be broken up

$$N_i^p(t) = N_{i_S}^p(t) + N_{i_N}^p(t) \quad (143)$$

where  $N_{i_S}^p(t)$  contains the  $1/\sqrt{t}$  terms and  $N_{i_N}^p(t)$  contains the remainder. Equation 113 may now be written

$$\begin{aligned} G_{ijl}^e(\zeta, t) &= I_1(\zeta, t) + I_2(t) + I_L(t) \\ I_1(\zeta, t) &= \int_0^1 u_{ij_A}^*(r_j(\zeta, t)) N_i^p(t) J(t) dt \\ I_2(t) &= \int_0^1 u_{ij_B}^*(t) N_{i_S}^p(t) J(t) dt \\ I_L(t) &= \int_0^1 u_{ij_B}^*(t) N_{i_N}^p(t) J(t) dt \end{aligned} \quad (144)$$

and for completeness

$$H_{ijl}^e(\zeta, t) = \int_0^1 p_{ij}^*(r_j(\zeta, t)) N_i^u(t) J(t) dt \quad (145)$$

Recalling that

$$u_{ij_A}^*(\zeta, t) = \frac{-1}{8\pi(1-\nu)\mu} \left[ (3-4\nu)\frac{1}{2} \ln(P'(\zeta, t))\delta_{ij} - r_{,i}(\zeta, t)r_{,j}(\zeta, t) \right] \quad (146)$$

$$u_{ij_B}^*(t) = \frac{-1}{8\pi(1-\nu)\mu} (3-4\nu) \ln(t)\delta_{ij} \quad (147)$$

and  $P'(\zeta, t)$  does not go to zero, it can be shown that  $I_1(\zeta, t)$  has a singular integrand at  $t = 0$  on the order of  $\frac{1}{\sqrt{t}}$ . When the source node is at the  $t = 1$  position,  $I_1(\zeta, t)$  is mapped such that the integrand becomes singular at  $t = 1$  and is on the order of  $\frac{1}{\sqrt{1-t}}$ .  $I_2(t)$  has a singular integrand at  $t = 0$  on the order of  $\frac{\ln(t)}{\sqrt{t}}$ . When the source node is at the  $t = 1$  position,  $I_2(t)$  is mapped such that the integrand becomes singular at both  $t = 0$  and  $t = 1$  and is on the order of  $\frac{\ln(t)}{\sqrt{1-t}}$ . In both cases, the integral itself exists and the singularity may be eliminated by an appropriate mapping of  $t$ .  $I_L(t)$  has a simple  $\ln(t)$  singularity and is integrated using a logarithmic quadrature. The mapping for  $I_1(\zeta, t)$  may be applied to Equation 145 without detrimental effect.

Recalling from Chapter IV that  $r(\zeta, t)$  and  $J(t)$  are calculated after a "splitting" mapping such that  $t = t(s)$ ,  $I_1(\zeta, t)$  and  $I_2(t)$  can be rewritten and simplified for easier manipulation.

$$\begin{aligned} I_1 &= \int_0^1 r(s) \frac{N(t)}{\sqrt{t}} J(s) ds \\ I_2 &= \int_0^1 \ln(s) \frac{N(t)}{\sqrt{t}} J(s) ds \end{aligned} \quad (148)$$

For the case when there is a mapping of the type

$$t = s \quad dt = ds \quad (149)$$

the singularity may be removed for both  $I_1(t)$  and  $I_2(t)$  with

$$s = \xi^4 \quad ds = 4\xi^3 d\xi \quad (150)$$

For example

$$\begin{aligned} I_1 &= \int_0^1 r(s) \frac{N(s)}{\sqrt{s}} J(s) ds \\ &= \int_0^1 r(\xi^4) \frac{N(\xi^4)}{\sqrt{\xi^4}} 4\xi^3 J(\xi^4) d\xi \\ &= \int_0^1 4\xi r(\xi^4) N(\xi^4) J(\xi^4) d\xi \end{aligned} \quad (151)$$

and

$$\begin{aligned} I_2 &= \int_0^1 \ln(s) \frac{N(s)}{\sqrt{s}} J(s) ds \\ &= \int_0^1 \ln(\xi^4) \frac{N(\xi^4)}{\sqrt{\xi^4}} 4\xi^3 J(\xi^4) d\xi \\ &= \int_0^1 16\xi \ln(\xi) N(\xi^4) J(\xi^4) d\xi \end{aligned} \quad (152)$$

For the case when there is a mapping of the type

$$t = 1 - s \quad dt = -1 ds \quad (153)$$

the singularity may be removed for  $I_1(t)$  with

$$s = 1 - (1 - \xi)^4 \quad ds = 4(1 - \xi)^3 d\xi \quad (154)$$

Substituting

$$\begin{aligned}
I_1 &= \int_0^1 r(1-s) \frac{N(1-s)}{\sqrt{1-s}} J(1-s) ds \\
&= \int_0^1 r((1-\xi)^4) \frac{N((1-\xi)^4)}{\sqrt{(1-\xi)^4}} 4(1-\xi)^3 J((1-\xi)^4) d\xi \\
&= \int_0^1 4(1-\xi) r((1-\xi)^4) N((1-\xi)^4) J((1-\xi)^4) d\xi
\end{aligned} \tag{155}$$

For the case when there is a mapping of the type

$$t = 1 - s \quad dt = -1 ds \tag{156}$$

the singularity may be removed for  $I_2(t)$  with

$$\begin{aligned}
s = \sin^2 \xi \quad ds = 2 \sin \xi \cos \xi d\xi \quad 1 - \sin^2 \xi = \cos^2 \xi \\
\xi = \frac{\pi}{2} \eta \quad d\xi = \frac{\pi}{2} d\eta
\end{aligned} \tag{157}$$

Substituting

$$\begin{aligned}
I_2 &= \int_0^1 \ln(1-s) \frac{N(1-s)}{\sqrt{1-s}} J(1-s) ds \\
&= \int_0^{\pi/2} \ln(1 - \sin^2 \xi) \frac{N(1 - \sin^2 \xi)}{\sqrt{\cos^2 \xi}} 2 \sin \xi \cos \xi J(1 - \sin^2 \xi) d\xi \\
&= \int_0^1 \frac{\pi}{2} \ln(1 - \sin^2(\frac{\pi}{2}\eta)) N(1 - \sin^2(\frac{\pi}{2}\eta)) 2 \sin(\frac{\pi}{2}\eta) J(1 - \sin^2(\frac{\pi}{2}\eta)) d\eta
\end{aligned} \tag{158}$$

The various mappings are summarized in Table 1, for both left-type and right-type crack elements as shown in Figure 26, where “Section” denotes the section of the element, “Lwr Up” denotes the lower and upper limits of integration over that section, “Reverse” denotes reversal of the element’s nodes, and “Normal” denotes the

coefficient that the calculated normal is multiplied by. The mappings applied to the CTQUA and CTOVR elements may also be applied to the CTQT element singular integrations yielding more consistent results than if the mappings are not applied.

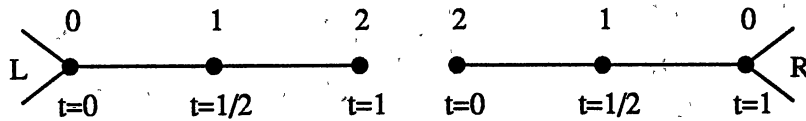


Figure 26. 2D Singular Integration Configuration

Table 1. 2D Singular Integration Mapping Summary

	Left Crack Element	Right Crack Element
Src Node	0	0
Section	0	0
Lwr Upr	0 1	1 0
Reverse	No	Yes
Normal	+1	+1
Split Map	$t = s \quad dt = ds$	$t = 1 - s \quad dt = -1 ds$
$I_1$ Map	$s = \xi^4 \quad ds = 4\xi^3 d\xi$	$s = 1 - (1 - \xi)^4 \quad ds = 4(1 - \xi)^3 d\xi$
$I_2$ Map	$s = \xi^4 \quad ds = 4\xi^3 d\xi$	$s = \sin^2 \xi \quad ds = 2 \sin \xi \cos \xi d\xi$
$I_2$ Map		$\xi = \frac{\pi}{2} \eta \quad d\xi = \frac{\pi}{2} d\eta$
Src Node	1	1
Section	0	0
Lwr Upr	1/2 1	1/2 0
Reverse	No	Yes
Normal	+1	+1
Split Map	$t = \frac{1+s}{2} \quad dt = \frac{1}{2} ds$	$t = \frac{1-s}{2} \quad dt = -\frac{1}{2} ds$
$I_1$ Map		$s = 1 - (1 - \xi)^4 \quad ds = 4(1 - \xi)^3 d\xi$
$I_2$ Map		$s = \sin^2 \xi \quad ds = 2 \sin \xi \cos \xi d\xi$
$I_2$ Map		$\xi = \frac{\pi}{2} \eta \quad d\xi = \frac{\pi}{2} d\eta$
Src Node	1	1
Section	1	1
Lwr Upr	0 1/2	1 1/2
Reverse	No	Yes
Normal	-1	-1
Split Map	$t = \frac{1-s}{2} \quad dt = -\frac{1}{2} ds$	$t = \frac{1+s}{2} \quad dt = \frac{1}{2} ds$
$I_1$ Map	$s = 1 - (1 - \xi)^4 \quad ds = 4(1 - \xi)^3 d\xi$	
$I_2$ Map	$s = \sin^2 \xi \quad ds = 2 \sin \xi \cos \xi d\xi$	
$I_2$ Map	$\xi = \frac{\pi}{2} \eta \quad d\xi = \frac{\pi}{2} d\eta$	
Src Node	2	2
Section	0	0
Lwr Upr	1 0	0 1
Reverse	No	Yes
Normal	-1	-1
Split Map	$t = 1 - s \quad dt = -1 ds$	$t = s \quad dt = ds$
$I_1$ Map	$s = 1 - (1 - \xi)^4 \quad ds = 4(1 - \xi)^3 d\xi$	$s = \xi^4 \quad ds = 4\xi^3 d\xi$
$I_2$ Map	$s = \sin^2 \xi \quad ds = 2 \sin \xi \cos \xi d\xi$	$s = \xi^4 \quad ds = 4\xi^3 d\xi$
$I_2$ Map	$\xi = \frac{\pi}{2} \eta \quad d\xi = \frac{\pi}{2} d\eta$	

## Stress Intensity Factor Calculation

The two dimensional stress intensity factors that may be derived for use in boundary elements fall into two categories, those that use crack tip displacement values and those that use crack tip traction values. The configuration that will be used in this section is shown in Figure 27.

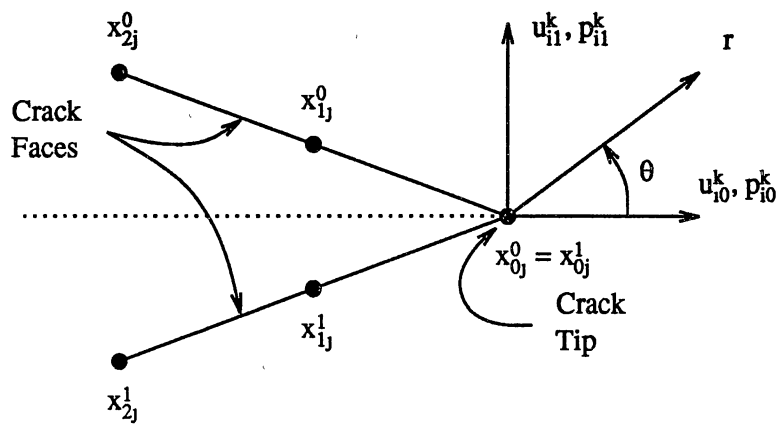


Figure 27. 2D SIF Configuration

### Displacement SIF

Since the CTQQ element type does not model the tractions properly, only the SIF derived from the displacements will be useful. Evaluation of

$$u_j^0 = N_l^u u_{lj}^0 \quad (159)$$

where  $N_i^u$  are given in Equation 115 at

$$t = \sqrt{\frac{r}{L}} \quad (160)$$

yields

$$u_j^0 = u_{0j}^0 + (-3u_{0j}^0 + 4u_{1j}^0 - u_{2j}^0)\sqrt{\frac{r}{L}} + (2u_{0j}^0 - 4u_{1j}^0 + 2u_{2j}^0)\frac{r}{L} \quad (161)$$

For a symmetric crack problem (i.e.,  $x_{i1}^0 = -x_{i1}^1$ ),  $u_{i0} = u_{01} = 0$  and Equation 161 reduces to

$$u_1^0 = (4u_{11}^0 - u_{21}^0)\sqrt{\frac{r}{L}} + (4u_{11}^0 + 2u_{21}^0)\frac{r}{L} \quad (162)$$

The one point displacement formula is found by equating Equation 42 with  $u_{11}^0$  for  $\theta = \pi$  yielding

$$K_I = \frac{\mu}{2(1-\nu)}\sqrt{\frac{2\pi}{r}}u_{11}^0 \quad (163)$$

Evaluating for the case  $r = L/4$ , yields

$$K_I = \frac{\mu}{1-\nu}\sqrt{\frac{2\pi}{L}}u_{11}^0 \quad (164)$$

The two point displacement formula is found by equating the coefficients of  $\sqrt{r}$  in Equations 42 and 162 for  $\theta = \pi$  and  $r = L/4$  yields

$$K_I = \frac{\mu}{2(1-\nu)}\sqrt{\frac{2\pi}{L}}(4u_{11}^0 - u_{21}^0) \quad (165)$$

For the more general nonsymmetric (mixed mode) crack with  $\theta = \pi$ , and  $r = L/4$ ,



the SIF in Equations 41 and 42 uncouple and the one point (Equation 166) and two point (Equation 167) displacement formulas are found in a manner similar that above.

$$\begin{aligned} K_I &= \frac{\mu}{4(1-\nu)} \sqrt{\frac{2\pi}{L}} (u_{11}^0 - u_{11}^1) \\ K_{II} &= \frac{\mu}{4(1-\nu)} \sqrt{\frac{2\pi}{L}} (u_{10}^0 - u_{10}^1) \end{aligned} \quad (166)$$

$$\begin{aligned} K_I &= \frac{\mu}{4(1-\nu)} \sqrt{\frac{2\pi}{L}} [4(u_{11}^0 - u_{11}^1) + (u_{21}^0 - u_{21}^1)] \\ K_{II} &= \frac{\mu}{4(1-\nu)} \sqrt{\frac{2\pi}{L}} [4(u_{10}^0 - u_{10}^1) + (u_{20}^0 - u_{20}^1)] \end{aligned} \quad (167)$$

### Traction SIF

The CTQT, CTQUA, and CTOVR, elements properly model the  $1/\sqrt{r}$  singularity in the tractions. We can therefore employ the traction values directly to find the SIF. Note that since the displacement shape functions are still quadratic, the one and two point displacement SIF formulas are still valid. Recall that the geometry is represented by

$$x_j(t) = N_l^q(t) x_{lj} \quad (168)$$

the tractions by

$$p_j(t) = N_l^p(t) p_{lj} \quad (169)$$

and the radius vector for two dimensions by

$$r(t) = [(x_0(t) - x_{00})^2 + (x_1(t) - x_{10})^2]^{\frac{1}{2}} \quad (170)$$

Boundary discretization can always be done such that  $\theta = \pi$ . This yields, from Equations 38, 39 and 40

$$\begin{aligned}\sigma_{00}(t) = \sigma_{11}(t) &= \frac{K_I}{\sqrt{2\pi r(t)}} \\ \sigma_{01}(t) &= \frac{K_{II}}{\sqrt{2\pi r(t)}}\end{aligned}\quad (171)$$

Let  $\bar{p}_j$  be defined as follows

$$\bar{p}_j = \lim_{t \rightarrow 0} p_j(t) = \lim_{t \rightarrow 0} N_I^P(t) p_{Ij} \quad (172)$$

where

$$p_j(t) = \sigma_{j,1}(t) n_i \quad (173)$$

Combining these equations with  $n_0 = 0$  and  $n_1 = 1$  for a symmetric crack yields

$$\begin{aligned}\bar{p}_1 &= \lim_{t \rightarrow 0} N_I^P(t) p_{I1} = \lim_{t \rightarrow 0} \frac{K_I}{\sqrt{2\pi r(t)}} \\ \bar{p}_0 &= \lim_{t \rightarrow 0} N_I^P(t) p_{I0} = \lim_{t \rightarrow 0} \frac{K_{II}}{\sqrt{2\pi r(t)}}\end{aligned}\quad (174)$$

Rearranging

$$\begin{aligned}K_I &= \sqrt{2\pi} \lim_{t \rightarrow 0} \sqrt{r(t)} N_I^P(t) p_{I1} \\ K_{II} &= \sqrt{2\pi} \lim_{t \rightarrow 0} \sqrt{r(t)} N_I^P(t) p_{I0}\end{aligned}\quad (175)$$

For the CTQT element type,  $N_I^g(t)$  is given in Equation 54 and  $N_I^P(t)$  is given in Equation 121. Evaluating the limit portion of Equation 175 with  $t = \sqrt{\frac{r}{L}}$ , where  $r$  is

the position along the element in real space and  $L$  is the length of the element yields

$$\begin{aligned}\lim_{r \rightarrow 0} \sqrt{r} N_0^p(r) &= \sqrt{L} \\ \lim_{r \rightarrow 0} \sqrt{r} N_1^p(r) &= 0 \\ \lim_{r \rightarrow 0} \sqrt{r} N_2^p(r) &= 0\end{aligned}\tag{176}$$

The traction SIF for the CTQT element type are therefore

$$\begin{aligned}K_I &= \sqrt{2\pi L} p_{01} \\ K_{II} &= \sqrt{2\pi L} p_{00}\end{aligned}\tag{177}$$

For the CTQUA element type,  $N_t^q(t)$  is given in Equation 54 and  $N_t^p(t)$  is given in Equation 127. Evaluating the limit portion of Equation 175 yields

$$\begin{aligned}\lim_{t \rightarrow 0} \sqrt{r(t)} N_0^p(t) &= \frac{M}{\sqrt{2}} \\ \lim_{t \rightarrow 0} \sqrt{r(t)} N_1^p(t) &= 0 \\ \lim_{t \rightarrow 0} \sqrt{r(t)} N_2^p(t) &= 0\end{aligned}\tag{178}$$

where

$$M = \left[ (-3x_{00} + 4x_{10} - x_{20})^2 + (-3x_{01} + 4x_{11} - x_{21})^2 \right]^{\frac{1}{4}}\tag{179}$$

Note that for evenly spaced nodes  $M$  reduces to  $\sqrt{L}$  where  $L$  is the length of the

element. The traction SIF for the CTQT element type are therefore

$$K_I = \sqrt{\pi} M p_{01} \quad (180)$$

$$K_{II} = \sqrt{\pi} M p_{00}$$

For the CTOVR element type,  $N_1^g(t)$  is given in Equation 130 and  $N_l^p(t)$  is given in Equation 137. Evaluating the limit portion of Equation 175 yields

$$\begin{aligned} \lim_{t \rightarrow 0} \sqrt{r(t)} N_0^p(t) &= \frac{M}{\sqrt{2}} \\ \lim_{t \rightarrow 0} \sqrt{r(t)} N_1^p(t) &= 0 \\ \lim_{t \rightarrow 0} \sqrt{r(t)} N_2^p(t) &= 0 \end{aligned} \quad (181)$$

where  $M$  is as defined above. The traction SIF for the CTQT element type are therefore

$$K_I = \sqrt{\pi} M p_{01} \quad (182)$$

$$K_{II} = \sqrt{\pi} M p_{00}$$

# Chapter VI

## THREE DIMENSIONAL BOUNDARY ELEMENTS

The noncrack tip three dimensional shape functions and their use in the boundary element method will be examined in this chapter. The variation of the geometry, displacements, and tractions over an element will form an interpolating surface patch in two parametric coordinates. As with the two dimensional shape functions, all of these elements will have an isoparametric formulation.

### Derivation

Most surface patches fall into one of two categories, tensor product surfaces or lofting surfaces (more recently called Coons, blending, or transfinite surfaces). Although both of these types have been in use for many years, a distinction is rarely made between them.

One of the most common examples of tensor product surfaces is the Lagrange form:

$$S(s, t) = \sum_{i=0}^n \sum_{j=0}^m s_i t_j K_i^n(s) L_j^m(t) \quad (183)$$

where  $K_i^n(s)$  and  $L_j^m(t)$  are the Lagrange polynomials (see Equation 47). Some of

the most common three dimensional boundary elements can be derived using this approach: the three-noded triangular element, the six-noded triangular element, and the four-noded rectangular element.

Lofting surfaces have long been used in number of areas including ship design [28]. Coons used a related method for blending four curves to form a surface [16,5]. A Coons approach was employed in 1977 by Brewer to first derive the Overhauser surface patch that had  $C^1$  continuity along all four edges [12]. Hibbs [32] employed a tensor product approach to derive a three dimensional boundary element that he called "Overhauser."

The components that go into the derivation of a Coons-type surface are depicted in Figure 28. The surface itself is a function of both the curves that make up the

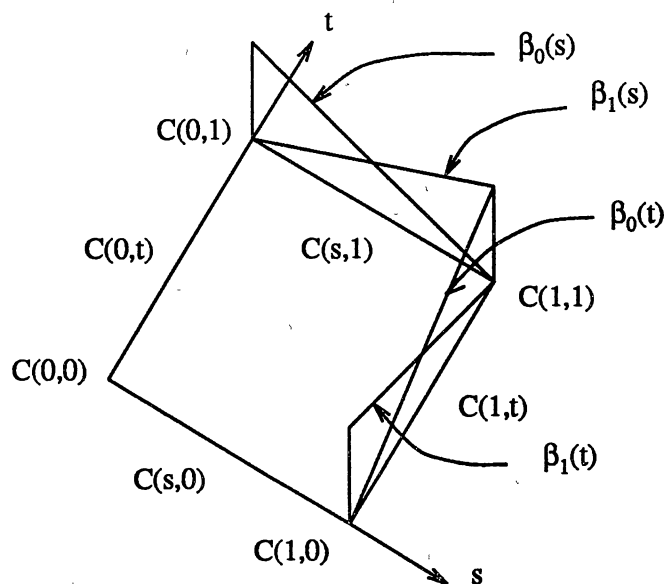


Figure 28. Coons Surface Configuration

edges of the patch  $C(s, t)$  and a set of blending function  $\beta_i(s)$  and  $\beta_i(t)$  and is given in Equation 184:

$$\begin{aligned}
 S(s, t) = & C(0, t)\beta_0(s) + C(1, t)\beta_1(s) \\
 & + C(s, 0)\beta_0(t) + C(s, 1)\beta_1(t) \\
 & - C(0, 0)\beta_0(s)\beta_0(t) - C(0, 1)\beta_0(s)\beta_1(t) \\
 & - C(1, 0)\beta_1(s)\beta_0(t) - C(1, 1)\beta_1(s)\beta_1(t)
 \end{aligned} \tag{184}$$

The edge curves are the two dimensional boundary element shape functions derived in Chapters IV and V, while the blending functions are typically linear Lagrangian or cubic Hermite shape functions. The surface patch  $S(s, t)$  may then be factored into three dimensional shape functions such that

$$\begin{aligned}
 x_j(s, t) &= N_l^g(s, t) x_{lj} \\
 u_j(s, t) &= N_l^u(s, t) u_{lj} \\
 p_j(s, t) &= N_l^p(s, t) p_{lj}
 \end{aligned} \tag{185}$$

where  $N_l^g(s, t)$  are the geometry shape functions corresponding to node  $l$  on the element and  $x_{lj}$  is the coordinate in direction  $j$  of node  $l$  of the element. The displacement shape functions  $N_l^u(s, t)$  and the traction shape functions  $N_l^p(s, t)$  are both equal to the geometry shape functions for the noncrack tip elements.

The Coons approach can be used to derive many three dimensional boundary elements including the Overhauser-type elements, the eight-node "serendipity" quadratic quadrilateral, and the twelve-node "serendipity" cubic quadrilateral. The

derivation of the “serendipity” elements is much more straightforward than the one that is typically presented (for example, see Reference [70]).

### Rectangular Linear (RLIN) Element

One of the simplest three dimensional boundary elements is the rectangular linear element (often called the four noded quadrilateral). The Rectangular LINEar element type will be abbreviated RLIN and its geometry is given in Figure 29. Both of the parameters  $s$  and  $t$  vary from 0 to 1.

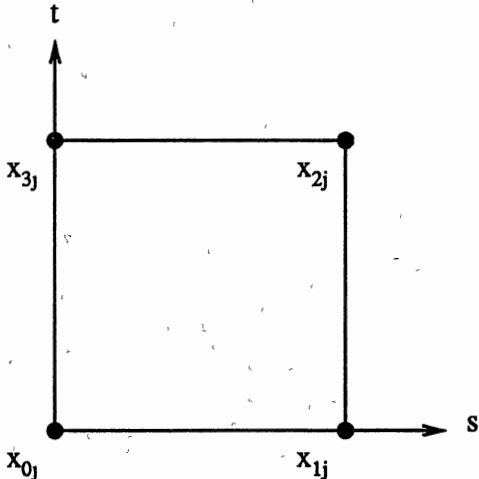


Figure 29. RLIN Element Geometry

The RLIN element may be derived using a Lagrangian tensor product approach (Equation 183) with the linear Lagrangian shape functions (Equation 52). The RLIN shape functions are given in Equation 186.  $N_0(s,t)$  is plotted in Figure 30. The other shape functions are so similar in appearance to  $N_0(s,t)$  (i.e.,  $N_1(1,0) = 1$ ,



$N_2(1, 1) = 1$ , and  $N_3(0, 1) = 1$ ) that they are not shown for brevity.

$$N_0(s, t) = (s - 1)(t - 1)$$

$$N_1(s, t) = s(1 - t)$$

$$N_2(s, t) = st$$

$$N_3(s, t) = t(1 - s)$$

(186)

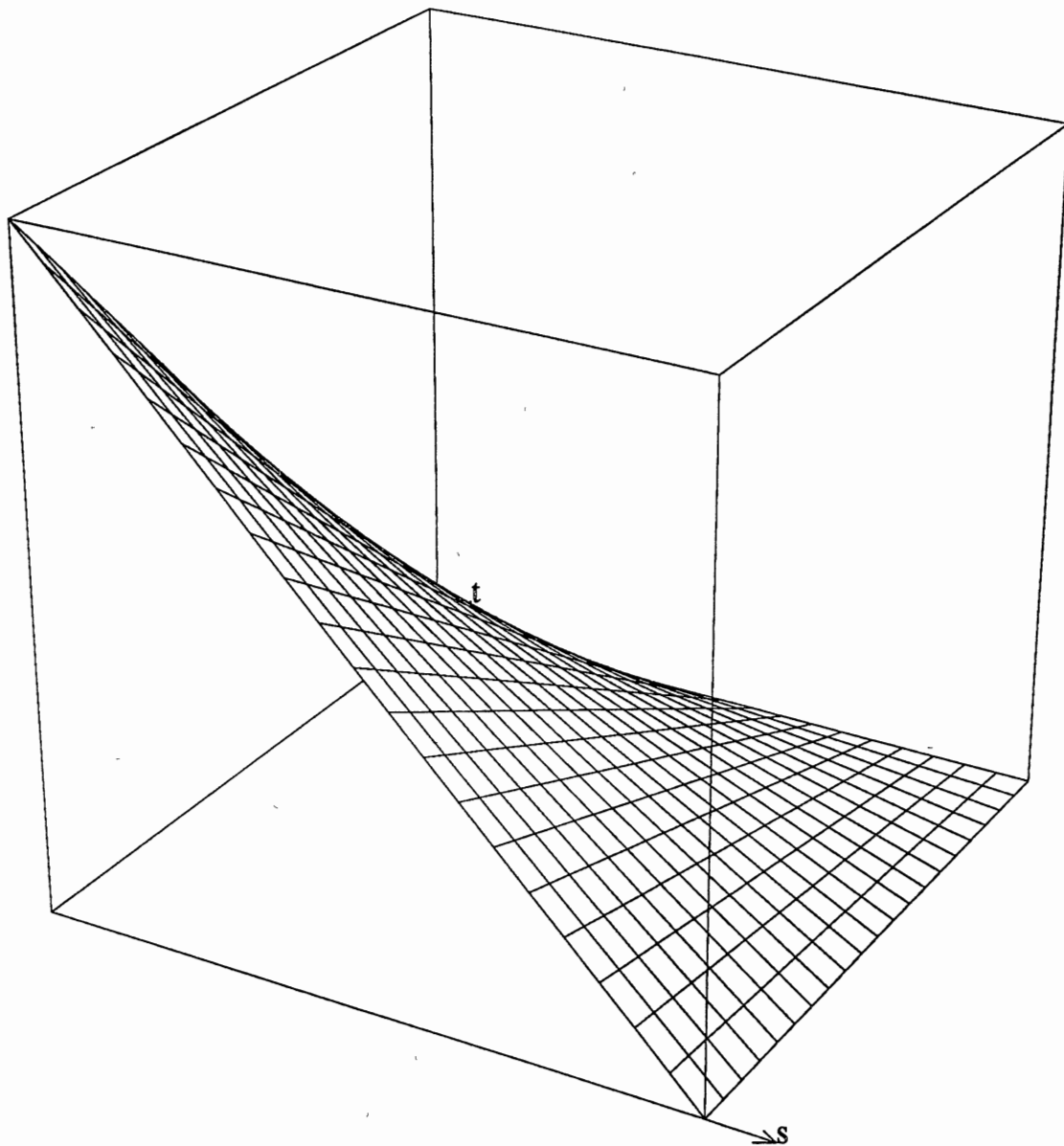


Figure 30. RLIN  $N_0$  Shape Function

## Rectangular Quadratic (RQUA) Element

The simplest three dimensional boundary element that is useful for elastostatics problems that involve bending is the rectangular quadratic element. The Rectangular QUAdratic element type will be abbreviated RQUA and its geometry is given in Figure 31. Both of the parameters  $s$  and  $t$  vary from 0 to 1.

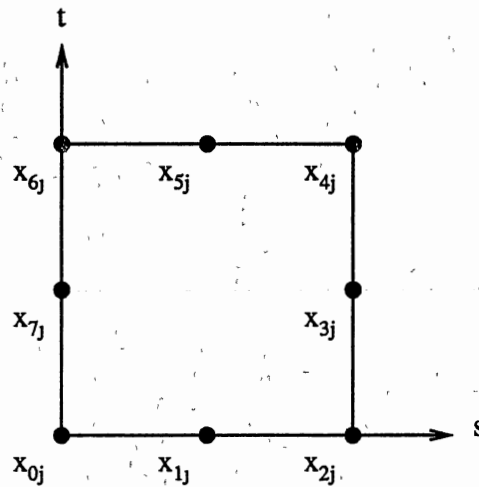


Figure 31. RQUA Element Geometry

The RQUA shape functions may be derived using the Coons surface approach with the linear Lagrangian blending functions

$$\beta_0(t) = 1 - t \tag{187}$$

$$\beta_1(t) = t$$

and the edges of the patch made up of Lagrangian quadratic shape functions (Equation 54). Substituting into the various  $C(s, t)$

$$\begin{aligned}
C(s, 0) &= x_{2j}s(2s - 1) + x_{0j}(s - 1)(2s - 1) - 4x_{1j}(s - 1)s \\
C(s, 1) &= x_{4j}s(2s - 1) + x_{6j}(s - 1)(2s - 1) - 4x_{5j}(s - 1)s \\
C(0, t) &= x_{6j}t(2t - 1) + x_{0j}(t - 1)(2t - 1) - 4x_{7j}(t - 1)t \\
C(1, t) &= x_{4j}t(2t - 1) + x_{2j}(t - 1)(2t - 1) - 4x_{3j}(t - 1)t \\
C(0, 0) &= x_{0j} \\
C(0, 1) &= x_{6j} \\
C(1, 0) &= x_{2j} \\
C(1, 1) &= x_{4j}
\end{aligned} \tag{188}$$

Substituting into Equation 184 yields the equation for the surface patch

$$\begin{aligned}
S(s, t) &= (1 - s)(x_{6j}t(2t - 1) + x_{0j}(t - 1)(2t - 1) - 4x_{7j}(t - 1)t) \\
&+ s(x_{4j}t(2t - 1) + x_{2j}(t - 1)(2t - 1) - 4x_{3j}(t - 1)t) \\
&+ (x_{4j}s(2s - 1) + x_{6j}(s - 1)(2s - 1) - 4x_{5j}(s - 1)s)t \\
&- x_{4j}st - x_{6j}(1 - s)t + (x_{2j}s(2s - 1) + x_{0j}(s - 1)(2s - 1) \\
&- 4x_{1j}(s - 1)s)(1 - t) - x_{2j}s(1 - t) - x_{0j}(1 - s)(1 - t)
\end{aligned} \tag{189}$$

Factoring out the coefficients of the  $x_i$ , gives the RQUA shape functions in Equation 190:

$$\begin{aligned}
 N_0(s, t) &= -(s-1)(t-1)(2(t+s)-1) \\
 N_1(s, t) &= 4(s-1)s(t-1) \\
 N_2(s, t) &= s(t-1)(2t-2s+1) \\
 N_3(s, t) &= -4s(t-1)t \\
 N_4(s, t) &= st(2(t+s)-3) \\
 N_5(s, t) &= -4(s-1)st \\
 N_6(s, t) &= -(s-1)t(2t-2s-1) \\
 N_7(s, t) &= 4(s-1)(t-1)t
 \end{aligned} \tag{190}$$

Plots of  $N_0(s, t)$  and  $N_1(s, t)$  are given in Figures 32 and 33 respectively, The other plots are similar and are omitted.

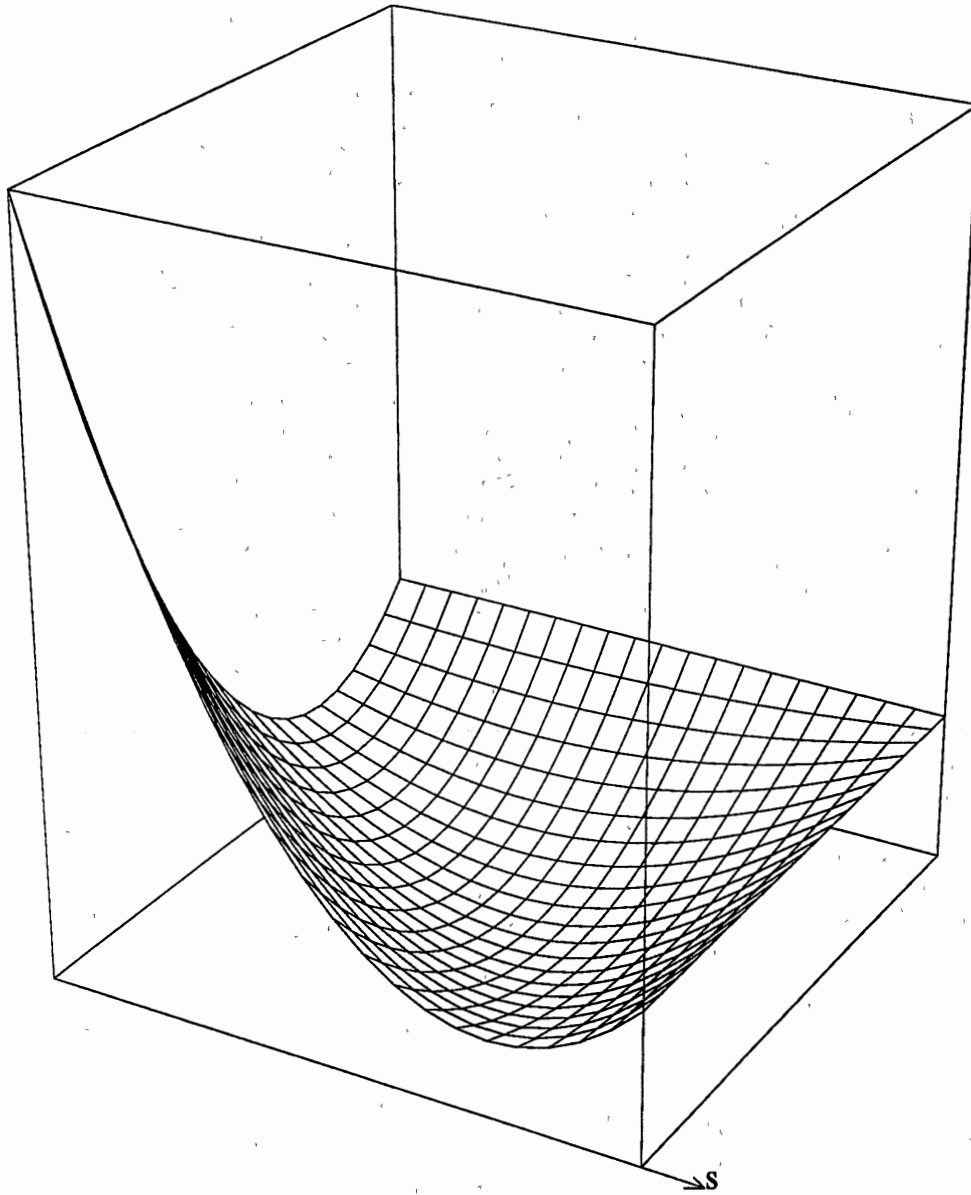


Figure 32. RQUA  $N_0$  Shape Function

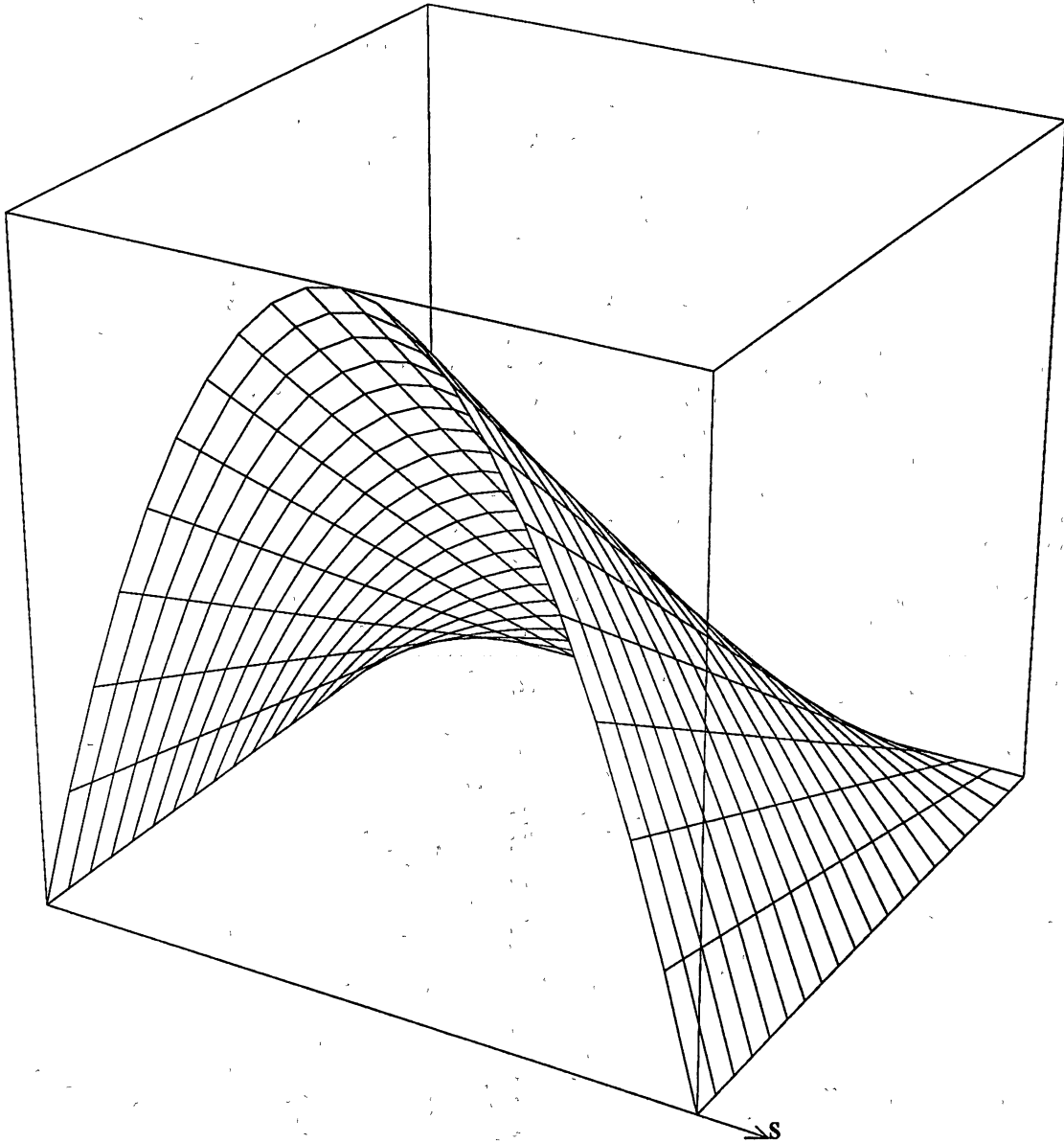


Figure 33. RQUA  $N_1$  Shape Function

## Rectangular Cubic (RCUB) Element

The rectangular cubic element is the most highest order boundary element in common use for elastostatics. The Rectangular CUBic element type will be abbreviated RCUB and its geometry is given in Figure 34. Both of the parameters  $s$  and  $t$  vary from 0 to 1.

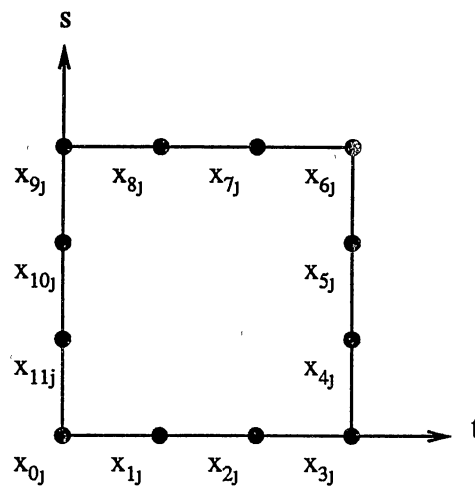


Figure 34. RCUB Element Geometry

The RCUB shape functions may be derived using the Coons surface approach with the linear Lagrangian blending functions

$$\begin{aligned}\beta_0(t) &= 1 - t \\ \beta_1(t) &= t\end{aligned}\tag{191}$$



and the edges of the patch made up of Lagrangian cubic shape functions (Equation 54). Substituting into Equation 184 and factoring out the coefficients of the  $x_i$ , yields the RCUB shape functions in Equation 192:

$$\begin{aligned}
N_0(s, t) &= \frac{(s-1)(t-1)((3t-2)(3t-1) + 9(s-1)s)}{2} \\
N_1(s, t) &= \frac{-9(s-1)s(3s-2)(t-1)}{2} \\
N_2(s, t) &= \frac{9(s-1)s(3s-1)(t-1)}{2} \\
N_3(s, t) &= \frac{-s(t-1)((3t-2)(3t-1) + 9(s-1)s)}{2} \\
N_4(s, t) &= \frac{9s(t-1)t(3t-2)}{2} \\
N_5(s, t) &= \frac{-9s(t-1)t(3t-1)}{2} \\
N_6(s, t) &= \frac{st((3t-2)(3t-1) + 9(s-1)s)}{2} \\
N_7(s, t) &= \frac{-9(s-1)s(3s-1)t}{2} \\
N_8(s, t) &= \frac{9(s-1)s(3s-2)t}{2} \\
N_9(s, t) &= \frac{-(s-1)t((3t-2)(3t-1) + 9(s-1)s)}{2} \\
N_{10}(s, t) &= \frac{9(s-1)(t-1)t(3t-1)}{2} \\
N_{11}(s, t) &= \frac{-9(s-1)(t-1)t(3t-2)}{2}
\end{aligned} \tag{192}$$

Plots of  $N_0(s, t)$  and  $N_0(s, t)$  are given in Figures 35 and 36, respectively. The plots of the other shape functions are similar and are omitted for brevity.

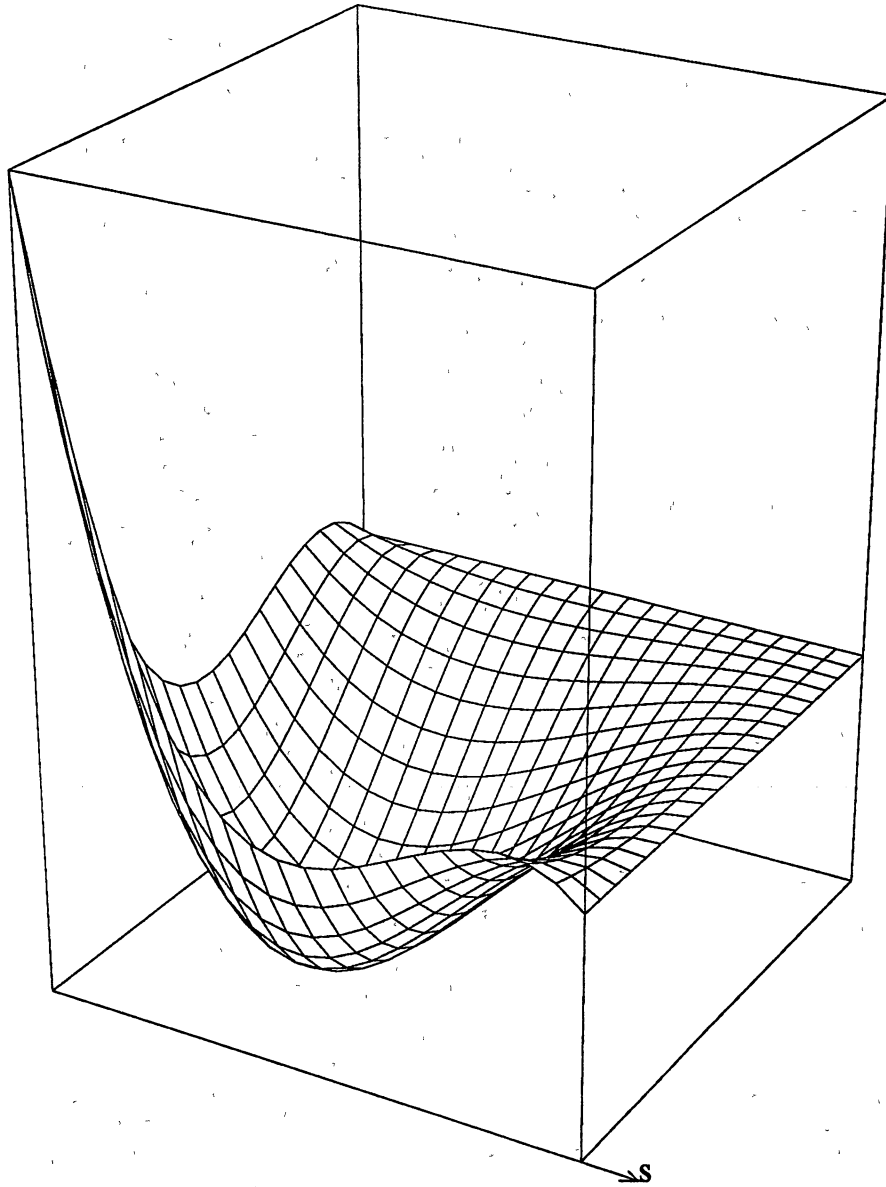


Figure 35. RCUB  $N_0$  Shape Function

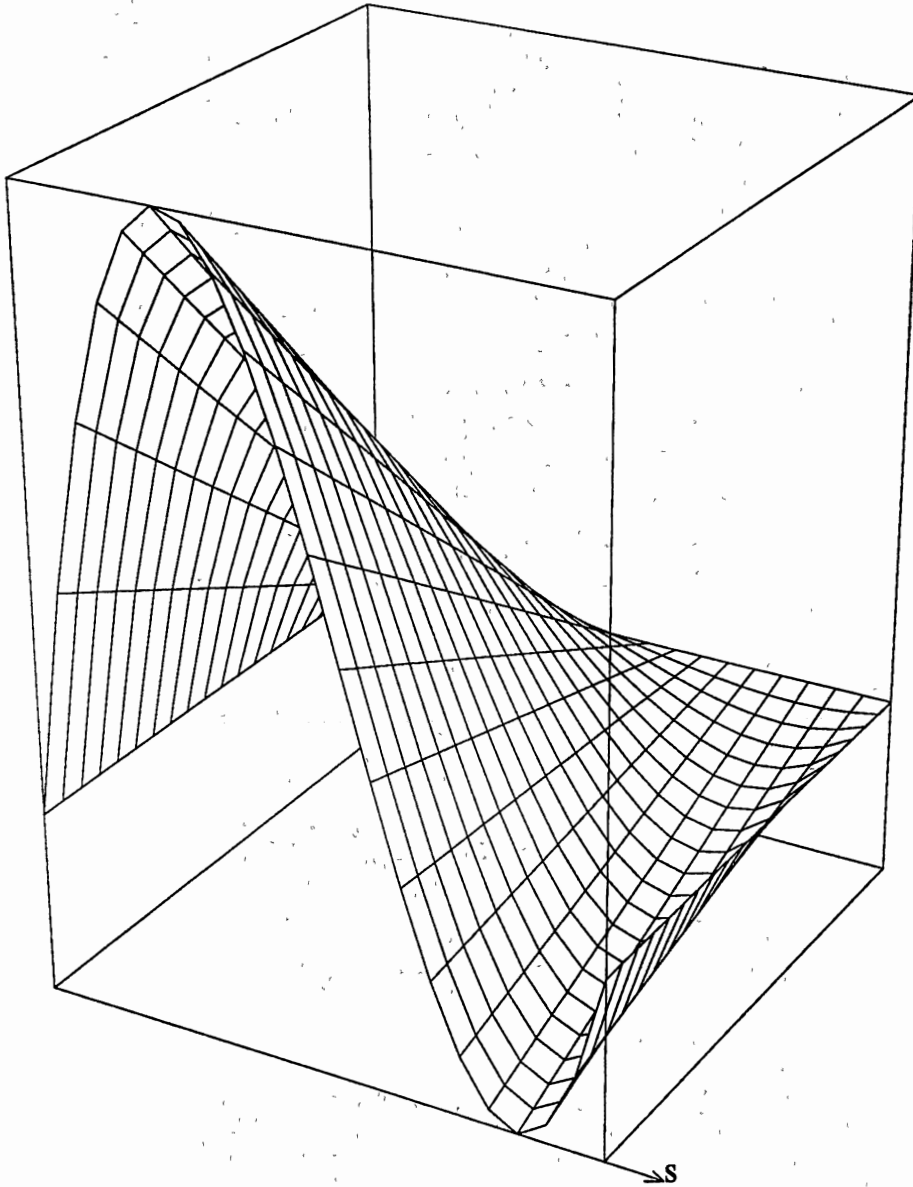


Figure 36. RCUB  $N_1$  Shape Function

## Rectangular Overhauser

### (ROVR) Element

The Rectangular OVerhauser element type will be abbreviated ROVR. It is the same as the Overhauser surface patch described in Reference [12] and its geometry is illustrated in Figure 37. Both of the parameters  $s$  and  $t$  vary from 0 to 1. The

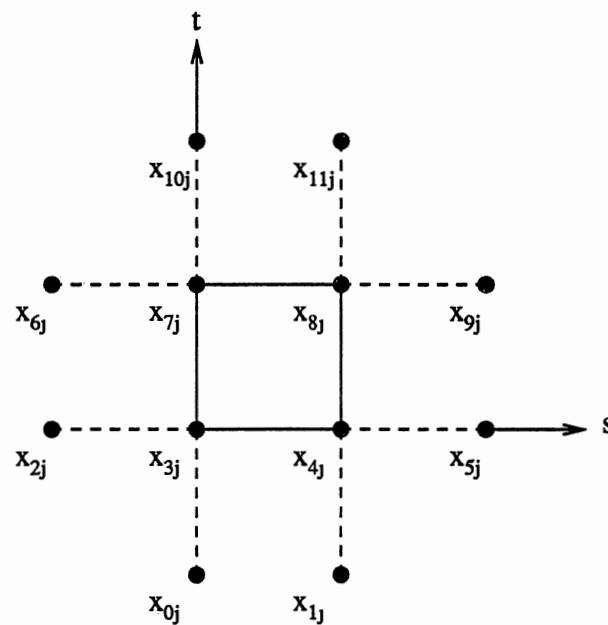


Figure 37. ROVR Element Geometry

ROVR shape functions may be derived using the Coons surface approach with the cubic Hermite polynomial blending functions

$$\beta_0(t) = 1 - 3t^2 + 2t^3 \quad (193)$$

$$\beta_1(t) = 3t^2 - 2t^3$$

and both of the edge curves are OVER curves. Substituting into Equation 184 and factoring out the coefficients of the  $x_{li}$ , yields the ROVR shape functions in Equation 194.  $N_0(s, t)$  is plotted in Figure 38 and  $N_3(s, t)$  in Figure 39. The other shape function plots are similar and are omitted for brevity.

$$\begin{aligned}
N_0(s, t) &= \frac{-(s-1)^2(2s+1)(t-1)^2t}{2} \\
N_1(s, t) &= \frac{s^2(2s-3)(t-1)^2t}{2} \\
N_2(s, t) &= \frac{-(s-1)^2s(t-1)^2(2t+1)}{2} \\
N_3(s, t) &= \frac{(s-1)(t-1)t((4s^2-3s-3)t-3s^2+2s+2)-3s^2+2s+2}{2} \\
N_4(s, t) &= \frac{-s(t-1)t((4s^2-5s-2)t-3s^2+4s+1)-3s^2+4s+1}{2} \\
N_5(s, t) &= \frac{(s-1)s^2(t-1)^2(2t+1)}{2} \\
N_6(s, t) &= \frac{(s-1)^2st^2(2t-3)}{2} \\
N_7(s, t) &= \frac{-(s-1)t((4s^2-3s-3)t-5s^2+4s+4)-(s-1)(2s+1)}{2} \\
N_8(s, t) &= \frac{st(t((4s^2-5s-2)t-5s^2+6s+3)-s(2s-3))}{2} \\
N_9(s, t) &= \frac{-(s-1)s^2t^2(2t-3)}{2} \\
N_{10}(s, t) &= \frac{(s-1)^2(2s+1)(t-1)t^2}{2} \\
N_{11}(s, t) &= \frac{-s^2(2s-3)(t-1)t^2}{2}
\end{aligned} \tag{194}$$

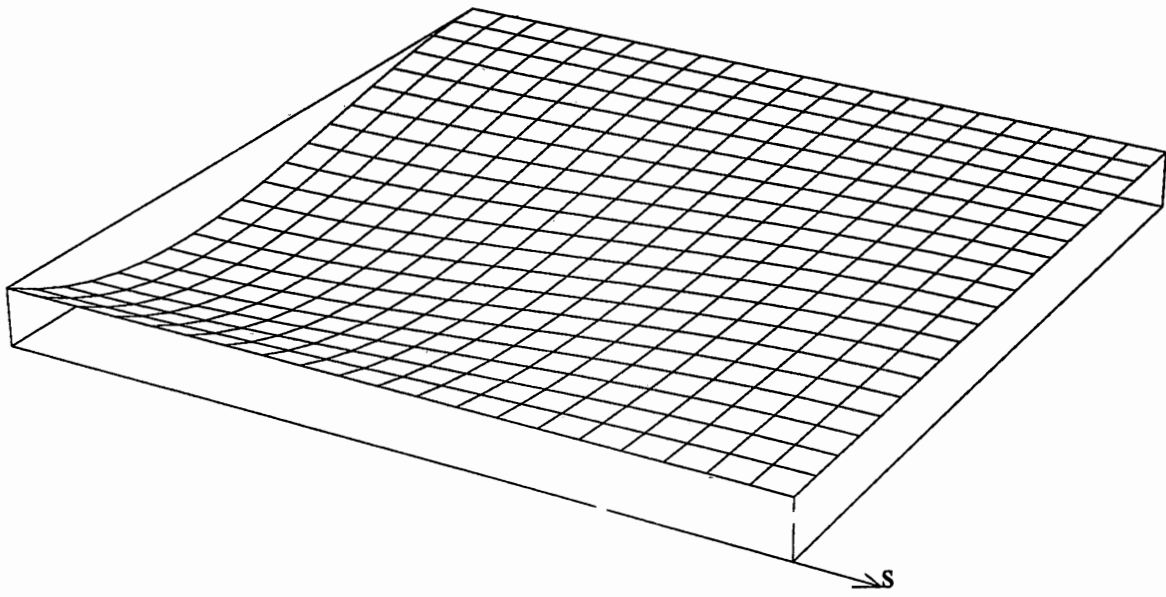


Figure 38. ROVR  $N_0$  Shape Function

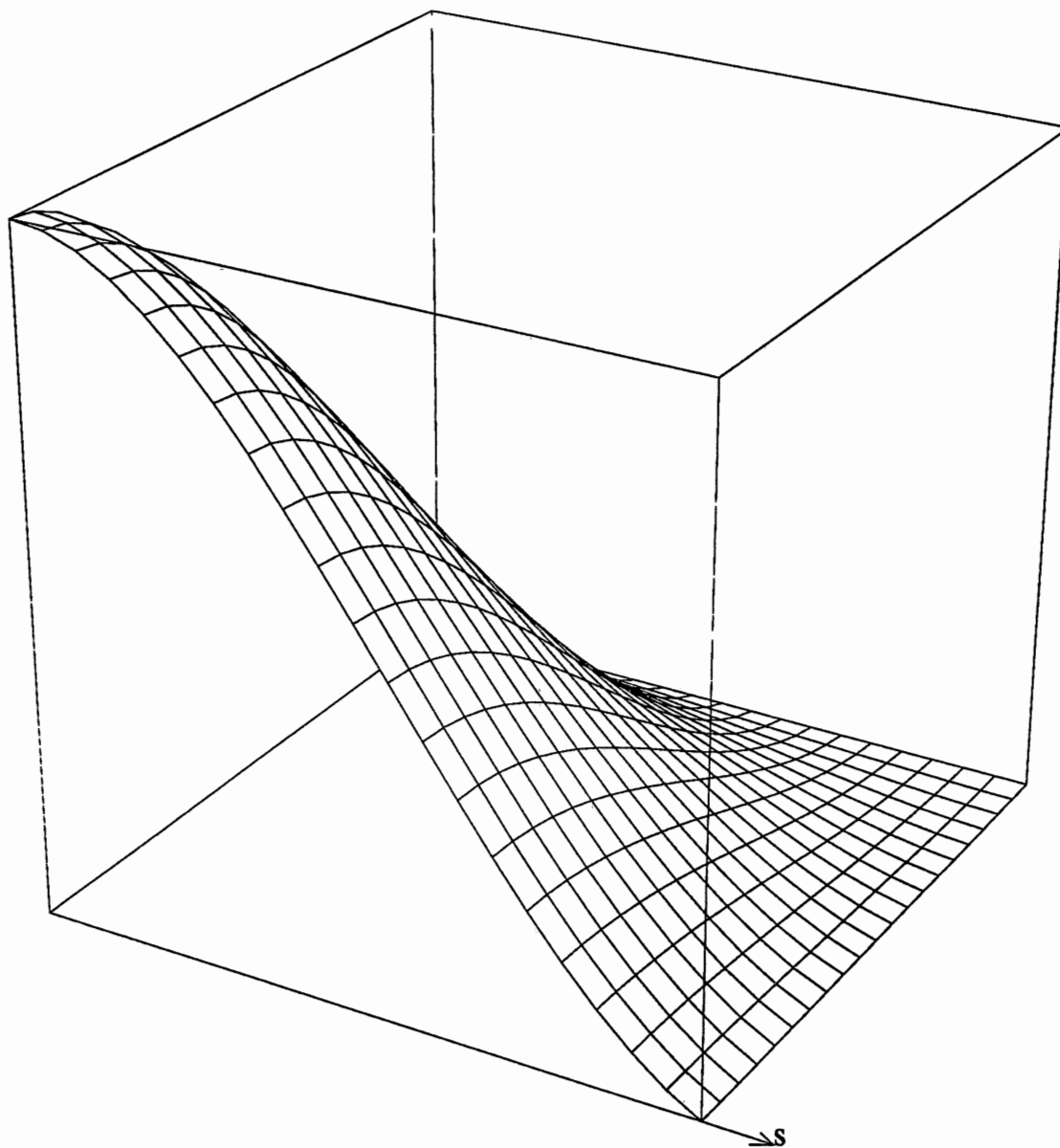


Figure 39. ROVR  $N_3$  Shape Function

## Rectangular Side Overhauser

### (ROVRS) Element

The Rectangular Side Overhauser element type will be abbreviated ROVRS. It is an entirely new element whose purpose is to fit along a side where the overlapping ROVR element would be inappropriate. In a computer graphics application, a corner type Overhauser element would be made by moving one of the overlapping ROVR nodes onto the surface patch proper. However, this approach is not applicable to the boundary element method, since the singular integrations when the overlapped node is a source node would be incorrect. The ROVRS element geometry is pictured in Figure 40. Both of the parameters  $s$  and  $t$  vary from 0 to 1.

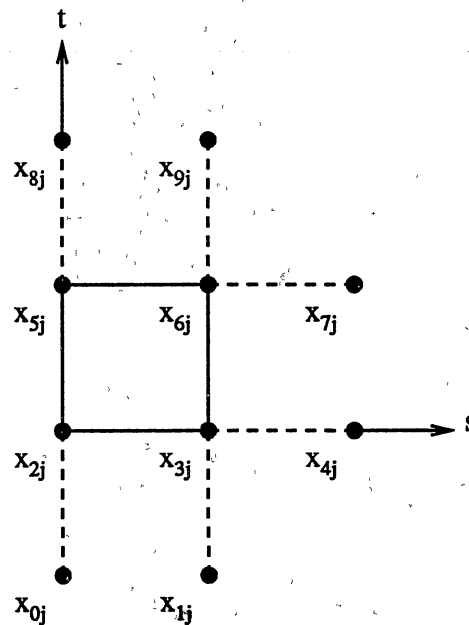


Figure 40. ROVRS Element Geometry



The ROVRS element is derived using the Coons surface approach (Equation 184) where  $\beta_j(t)$  is given by Equation 193,  $C(0, t)$  and  $C(1, t)$  by the OVER shape functions, and  $C(s, 0)$  and  $C(s, 1)$  by the OVRL shape functions. The resultant ROVRS shape functions are given in Equation 195.  $N_2(s, t)$  is presented in Figure 41. The other shape functions are similar to  $N_2(s, t)$  as shown and  $N_0(s, t)$  for the ROVR element.

$$\begin{aligned}
N_0(s, t) &= \frac{-(s-1)^2(2s+1)(t-1)^2t}{2} \\
N_1(s, t) &= \frac{s^2(2s-3)(t-1)^2t}{2} \\
N_2(s, t) &= \frac{-(s-1)(t-1)(t((2s^2-3s+3)t+s-2)+s-2)}{2} \\
N_3(s, t) &= \frac{s(t-1)(t((2s^2-7s+8)t+2s-4)+2s-4)}{2} \\
N_4(s, t) &= \frac{(s-1)s(t-1)^2(2t+1)}{2} \\
N_5(s, t) &= \frac{(s-1)t(t((2s^2-3s+3)t-4s^2+5s-4)+(s-1)(2s+1))}{2} \\
N_6(s, t) &= \frac{-st(t((2s^2-7s+8)t-4(s^2-3s+3))+s(2s-3))}{2} \\
N_7(s, t) &= \frac{-(s-1)st^2(2t-3)}{2} \\
N_8(s, t) &= \frac{(s-1)^2(2s+1)(t-1)t^2}{2} \\
N_9(s, t) &= \frac{-s^2(2s-3)(t-1)t^2}{2}
\end{aligned} \tag{195}$$

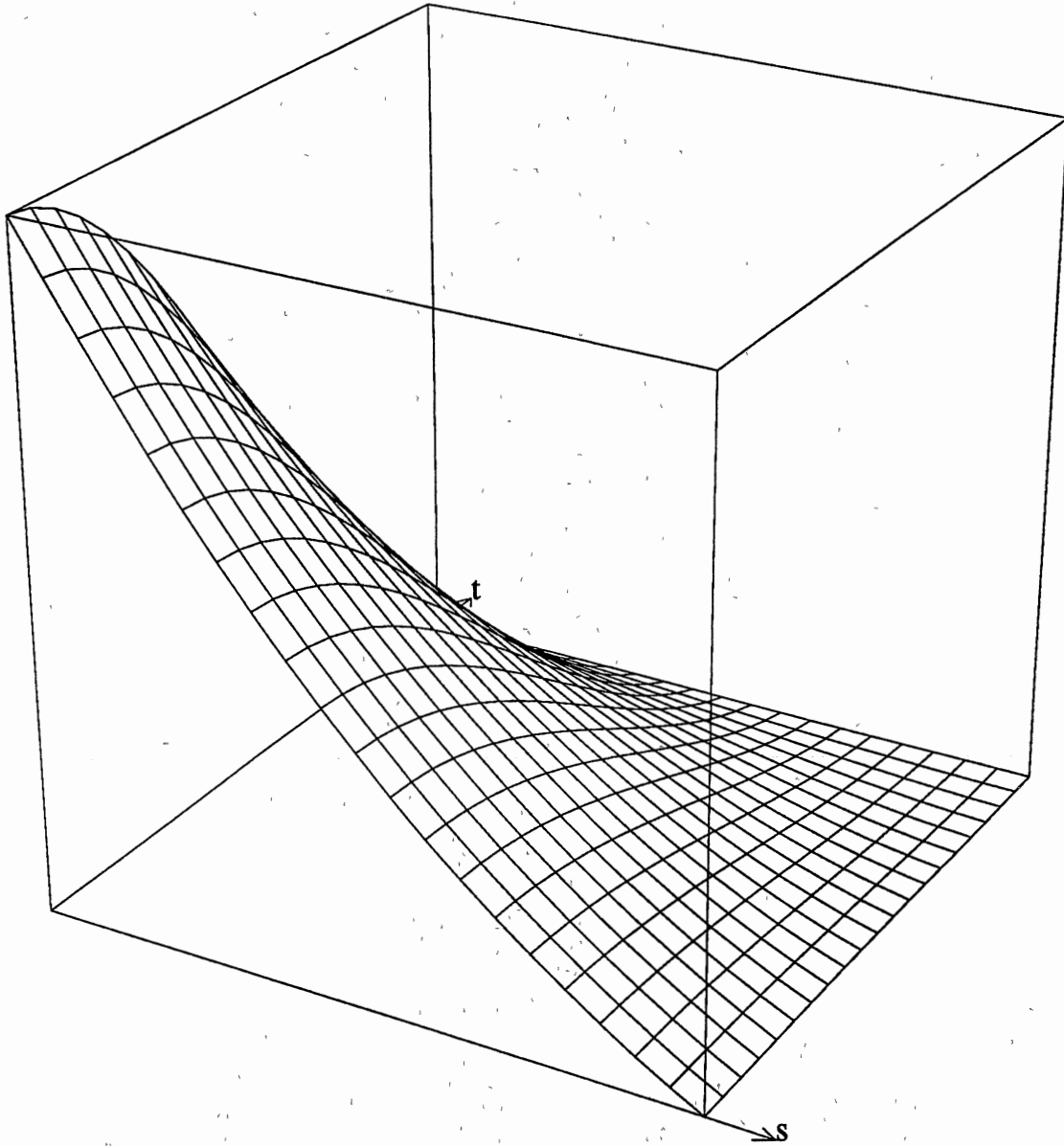


Figure 41. ROVRS  $N_2$  Shape Function

## Rectangular Corner Overhauser

### (ROVRC) Element

The Rectangular Corner OVerhauser element type will be abbreviated ROVRC.

It is an entirely new element whose purpose is to fit in a corner where the overlapping ROVR or ROVRS element would be inappropriate. The ROVRC element geometry is illustrated in Figure 42. Both of the parameters  $s$  and  $t$  vary from 0 to 1.

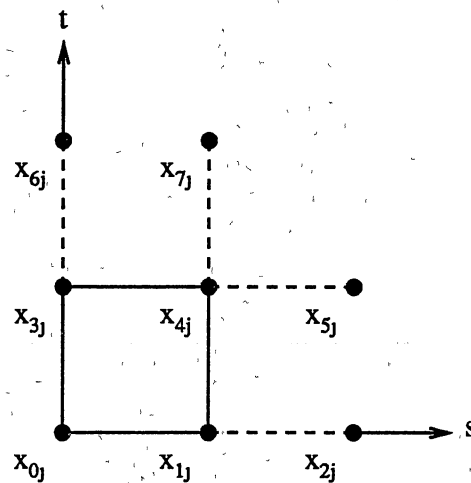


Figure 42. ROVRC Element Geometry

The ROVRC element is derived using the Coons surface approach (Equation 184) where  $\beta_j(t)$  is given by Equation 193 and  $C(s, t)$  by the OVRL shape functions. The resultant ROVRC shape functions are given in Equation 196.  $N_0(s, t)$  is pictured in Figure 43. The other shape functions are similar to  $N_0(s, t)$  presented and  $N_0(s, t)$

for the ROVR element.

$$\begin{aligned}
N_0(s, t) &= \frac{-(s-1)(t-1)(t(2s((4s-3)t-3s+2)+1)+s-2)}{2} \\
N_1(s, t) &= \frac{s(t-1)(t(8(s-1)^2t-(2s-1)(3s-4))+2s-4)}{2} \\
N_2(s, t) &= \frac{(s-1)s(t-1)^2(2t+1)}{2} \\
N_3(s, t) &= \frac{(s-1)t(t(s(2(4s-3)t-16s+11)+2)+4(s-1)(2s+1))}{2} \\
N_4(s, t) &= -st(t(4(s-1)^2t-8s^2+15s-6)+2s(2s-3)) \\
N_5(s, t) &= \frac{-(s-1)st^2(2t-3)}{2} \\
N_6(s, t) &= \frac{(s-1)^2(2s+1)(t-1)t}{2} \\
N_7(s, t) &= \frac{-s^2(2s-3)(t-1)t}{2}
\end{aligned} \tag{196}$$

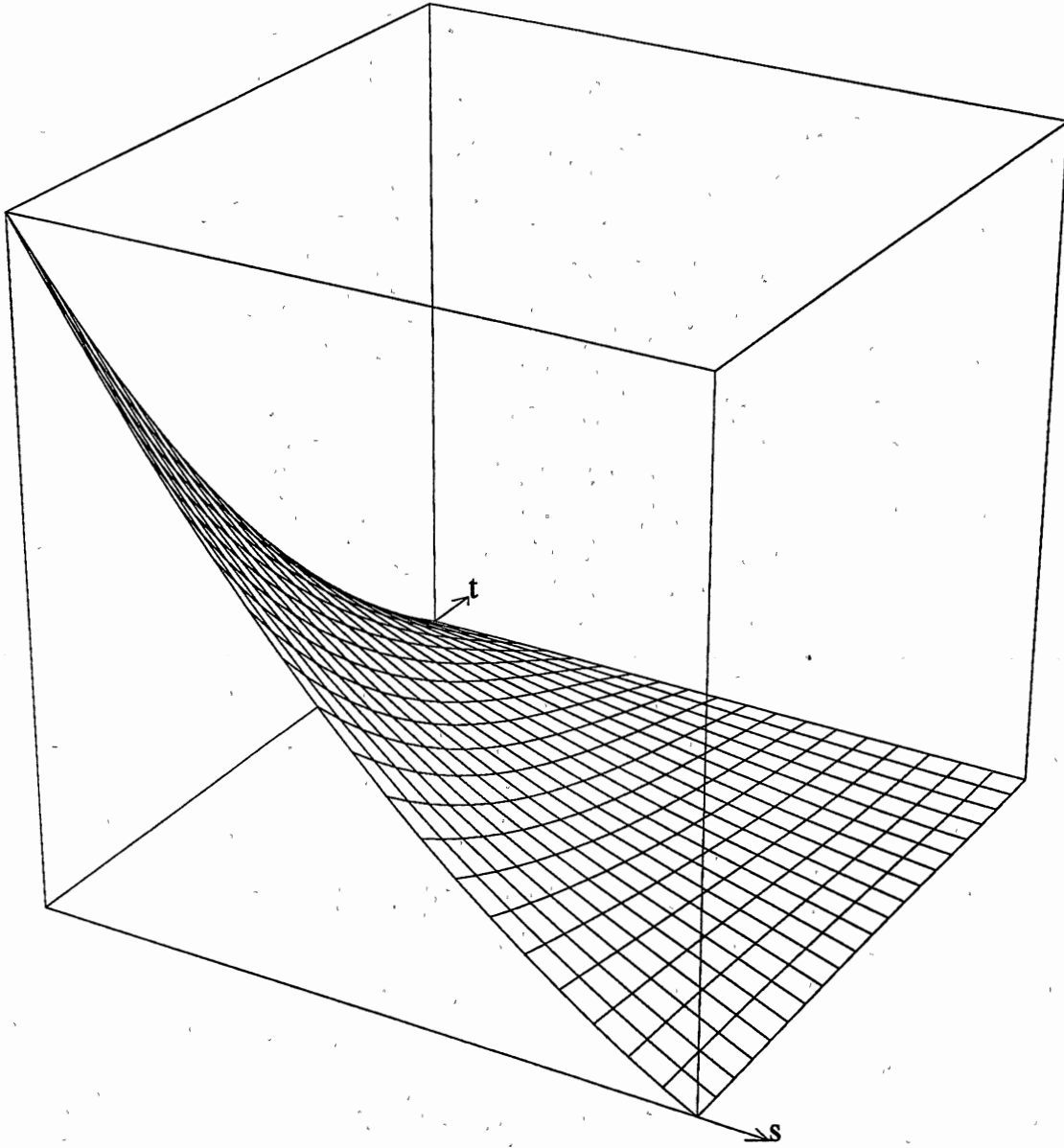


Figure 43. ROVRC  $N_0$  Shape Function

## Rectangular Corner Overhauser Variant (ROVRCV) Element

The Rectangular Corner OVerhauser Variant element type will be abbreviated ROVRCV. It is an entirely new element whose purpose is primarily the same as the ROVRC element; however, it is used in the crack tip context where the geometry of the problem would cause the ROVRC element's normal to point in the wrong direction. The ROVRCV element geometry is pictured in Figure 44. Both of the parameters  $s$  and  $t$  vary from 0 to 1.

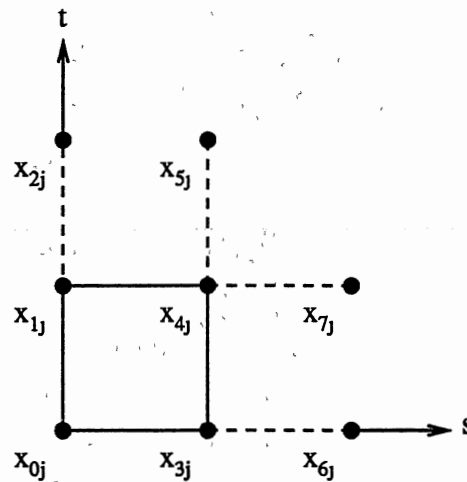


Figure 44. ROVRCV Element Geometry

The ROVRCV element is derived using the Coons surface approach (Equation 184) where  $\beta_j(t)$  is given by Equation 193 and  $C(s, t)$  by the OVRL shape functions. The resultant ROVRCV shape functions are shown in Equation 196. The

shape functions look the same as those for the ROVRC element.

$$\begin{aligned}
 N_0(s, t) &= \frac{-(s-1)(t-1)(t(2s((4s-3)t-3s+2)+1)+s-2)}{2} \\
 N_1(s, t) &= \frac{(s-1)t(t(s(2(4s-3)t-16s+11)+2)+4(s-1)(2s+1))}{2} \\
 N_2(s, t) &= \frac{(s-1)^2(2s+1)(t-1)t}{2} \\
 N_3(s, t) &= \frac{s(t-1)(t(8(s-1)^2t-(2s-1)(3s-4))+2s-4)}{2} \\
 N_4(s, t) &= -st(t(4(s-1)^2t-8s^2+15s-6)+2s(2s-3)) \\
 N_5(s, t) &= \frac{-s^2(2s-3)(t-1)t}{2} \\
 N_6(s, t) &= \frac{(s-1)s(t-1)^2(2t+1)}{2} \\
 N_7(s, t) &= \frac{-(s-1)st^2(2t-3)}{2}
 \end{aligned} \tag{197}$$

## Integration

The integrations that need to be performed over a single boundary element are

$$H_{ijl}^e(\zeta, \eta) = \iint_{\Gamma^e} p_{ij}^*(\zeta, \eta) N_l^u(\eta) d\Gamma^e \quad (198)$$

$$G_{ijl}^e(\zeta, \eta) = \iint_{\Gamma^e} u_{ij}^*(\zeta, \eta) N_l^p(\eta) d\Gamma^e \quad (199)$$

These integrals are evaluated in the local coordinate system of the element. This may be accomplished with the Jacobian transformation

$$d\Gamma^e = J(s, t) ds dt \quad (200)$$

$$J(s, t) = \sqrt{g_i g_i} \quad (201)$$

$$\begin{aligned} g_0 &= \frac{\partial x_1}{\partial s} \frac{\partial x_2}{\partial t} - \frac{\partial x_2}{\partial s} \frac{\partial x_1}{\partial t} \\ g_1 &= \frac{\partial x_2}{\partial s} \frac{\partial x_0}{\partial t} - \frac{\partial x_0}{\partial s} \frac{\partial x_2}{\partial t} \\ g_2 &= \frac{\partial x_0}{\partial s} \frac{\partial x_1}{\partial t} - \frac{\partial x_1}{\partial s} \frac{\partial x_0}{\partial t} \end{aligned} \quad (202)$$

where  $s$  and  $t$  are the local parametric coordinates which both vary from 0 to 1 along the element. The normal to the element is calculated by

$$n_i = \frac{g_i}{J(s, t)} \quad (203)$$



Substituting

$$H_{i,j,l}^e(\zeta, s, t) = \int_0^1 \int_0^1 p_{i,j}^*(r_j(\zeta, s, t)) N_l^u(s, t) J(s, t) ds dt \quad (204)$$

$$G_{i,j,l}^e(\zeta, s, t) = \int_0^1 \int_0^1 u_{i,j}^*(r_j(\zeta, s, t)) N_l^p(s, t) J(s, t) ds dt \quad (205)$$

where the  $\zeta$  shows that the fundamental solution is also a function of the source node position. The radius vector is calculated by

$$r_j(\zeta, s, t) = x_j(s, t) - x_j(\zeta) \quad (206)$$

$$x_j(s, t) = N_l^g(s, t) x_{lj} \quad (207)$$

These integrations can be performed using standard product rule Gaussian quadrature formulas [58]. The product rule is basically a one dimensional quadrature in both the  $s$  and  $t$  directions

$$H_{i,j,l}^e(\zeta, s, t) \approx \sum_{a=1}^Q \sum_{b=1}^Q p_{i,j}^*(r_j(\zeta, s_a, t_b)) N_l^u(s_a, t_b) J(s_a, t_b) w_a w_b \quad (208)$$

$$G_{i,j,l}^e(\zeta, s, t) \approx \sum_{a=1}^Q \sum_{b=1}^Q u_{i,j}^*(r_j(\zeta, s_a, t_b)) N_l^p(s_a, t_b) J(s_a, t_b) w_a w_b \quad (209)$$

where  $s_a$  and  $t_b$  are the quadrature points,  $w_a$  and  $w_b$  are the quadrature weights, and  $Q$  is the number of quadrature points and weights.

## Singular Integration

If the source node belongs to the element which is being integrated, then the three dimensional fundamental solution becomes singular when  $r(\zeta, s, t) = 0$  (i.e., when  $x_j(s, t) = x_j(\zeta)$  the source node and field node are the same). Equation 204 then has a singularity on the order of

$$H_{ijl}^e(\zeta, s, t) = O\left(\iint \frac{1}{r(\zeta, s, t)} N_l^u(s, t) J(s, t) ds dt\right) \quad (210)$$

The shape functions which do not correspond to the source node are zero at the singular point, thereby canceling the singularity in the denominator. The shape function which corresponds to the source node has a value of one at the singular point and the singularity is not canceled. Because this term can be calculated using the rigid body motion equation (Equation 29), it is not needed. Equation 205 has a singular integrand on the order of

$$G_{ijl}^e(\zeta, s, t) = O\left(\iint \left[\frac{1}{r(\zeta, s, t)} + \frac{r_i(s, t)r_j(s, t)}{r^3(\zeta, s, t)}\right] N_l^p(s, t) J(s, t) ds dt\right) \quad (211)$$

and it must be calculated. The key is to find a transformation such that the singularity is eliminated. One such transformation is the triangle to square mapping (Figure 45); this maps one node (typically the singular one) of a triangle, to a line on the square. This is done by “doubling up” the shape functions for the square with the node that is to be mapped (i.e., node  $x_1$ , with shape functions  $N_1$  and  $N_2$ ). For

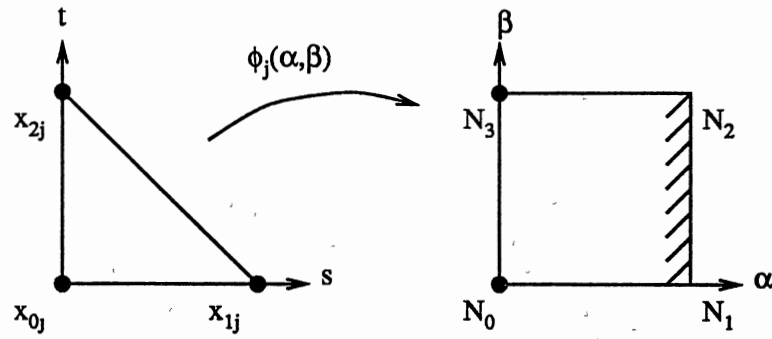


Figure 45. Triangle to Square Transformation

example, in Figure 45

$$(s, t) = \phi_j(\alpha, \beta) = N_0(\alpha, \beta)x_{0j} + N_3(\alpha, \beta)x_{2j} + [N_1(\alpha, \beta) + N_2(\alpha, \beta)]x_{1j} \quad (212)$$

where, the  $N_j(\alpha, \beta)$  are the RLIN shape functions as follows

$$\begin{aligned} N_0(\alpha, \beta) &= (\alpha - 1)(\beta - 1) \\ N_1(\alpha, \beta) &= \alpha(1 - \beta) \\ N_2(\alpha, \beta) &= \alpha\beta \\ N_3(\alpha, \beta) &= \beta(1 - \alpha) \end{aligned} \quad (213)$$

and

$$\begin{aligned} x_{0j} &= \langle 0 \quad 0 \rangle \\ x_{1j} &= \langle 1 \quad 0 \rangle \\ x_{2j} &= \langle 0 \quad 1 \rangle \end{aligned} \quad (214)$$

then

$$\begin{aligned} s &= N_1(\alpha, \beta) + N_2(\alpha, \beta) = \alpha \\ t &= N_3(\alpha, \beta) = \beta(1 - \alpha) \end{aligned} \quad (215)$$

The Jacobian  $J(\alpha, \beta)$  may then be calculated as follows

$$J(\alpha, \beta) = \begin{vmatrix} \frac{\partial s}{\partial \alpha} & \frac{\partial s}{\partial \beta} \\ \frac{\partial t}{\partial \alpha} & \frac{\partial t}{\partial \beta} \end{vmatrix} = \begin{vmatrix} 1 & 0 \\ -\beta & 1 - \alpha \end{vmatrix} = 1 - \alpha \quad (216)$$

For the triangle, Equation 211 becomes

$$G_{ijl}^e(\zeta, s, t) = O \left( \int_0^1 \int_0^{1-s} \left[ \frac{1}{r(\zeta, s, t)} + \frac{r_i(s, t)r_j(s, t)}{r^3(\zeta, s, t)} \right] N_l^p(s, t) J(s, t) ds dt \right) \quad (217)$$

Employing the triangle to square mapping

$$G_{ijl}^e(\zeta, ()) = O \left( \int_0^1 \int_0^1 \left[ \frac{1}{r(\zeta, ())} + \frac{r_i()r_j()}{r^3(\zeta, ())} \right] N_l^p() J() (1 - \alpha) d\alpha d\beta \right) \quad (218)$$

where  $() = (s(\alpha, \beta), t(\alpha, \beta))$ . A  $(1 - \alpha)$  may be factored out of  $r()$ ,  $r_i()$  and  $r_j()$  such that

$$\begin{aligned} r() &= (1 - \alpha) \bar{r}() \\ r_i() &= (1 - \alpha) \bar{r}_i() \\ r_j() &= (1 - \alpha) \bar{r}_j() \end{aligned} \quad (219)$$

Substituting and canceling common factors yields

$$G_{ijl}^e(\zeta, ()) = O \left( \int_0^1 \int_0^1 \left[ \frac{1}{\bar{r}(\zeta, ())} + \frac{\bar{r}_i()\bar{r}_j()}{\bar{r}^3(\zeta, ())} \right] N_l^p() J() d\alpha d\beta \right) \quad (220)$$

which is no longer singular. Note that  $N()$  goes to a nonzero value at the singular node so that the integrands are singular and not just indeterminate. This same procedure may be applied to any shape element as long as it can be subdivided into triangular pieces. The RLIN element may be subdivided into two triangular pieces, each of which may be mapped to squares as shown in Figure 46. Performing the

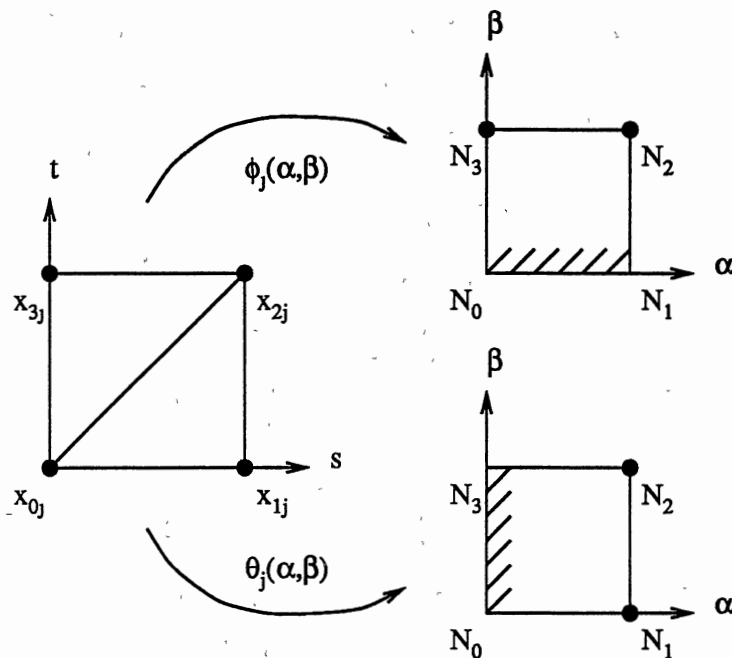


Figure 46. RLIN Singular Integration With Source at Node  $x_{0j}$

triangle to square mapping when the source is at node  $x_{0j}$ , yields for  $\phi_j(\alpha, \beta)$  and  $\theta_j(\alpha, \beta)$ , respectively:

$$\begin{aligned} s &= \alpha\beta & t &= \beta & J(\alpha, \beta) &= \beta \\ s &= \alpha & t &= \alpha\beta & J(\alpha, \beta) &= \alpha \end{aligned} \tag{221}$$

When the source is at node  $x_{1j}$ , the transformations are

$$\begin{aligned} s &= \alpha & t &= -(\alpha - 1)\beta & J(\alpha, \beta) &= 1 - \alpha \\ s &= (\alpha - 1)\beta + 1 & t &= \beta & J(\alpha, \beta) &= \beta \end{aligned} \quad (222)$$

When the source is at node  $x_{2j}$ , the transformations are

$$\begin{aligned} s &= \alpha - (\alpha - 1)\beta & t &= \beta & J(\alpha, \beta) &= 1 - \beta \\ s &= \alpha & t &= \alpha - (\alpha - 1)\beta & J(\alpha, \beta) &= 1 - \alpha \end{aligned} \quad (223)$$

When the source is at node  $x_{3j}$ , the transformations are

$$\begin{aligned} s &= \alpha & t &= \alpha(\beta - 1) + 1 & J(\alpha, \beta) &= \alpha \\ s &= -\alpha(\beta - 1) & t &= \beta & J(\alpha, \beta) &= 1 - \beta \end{aligned} \quad (224)$$

The transformations used for the RLIN element may also be used for the ROVR, ROVRS, and ROVRC elements.

The RQUA element may be subdivided into three triangular pieces that may be transformed into squares as shown in Figure 47. Performing the triangle to square mapping when the source is at node  $x_{7j}$ , yields for  $\phi_j(\alpha, \beta)$ ,  $\theta_j(\alpha, \beta)$ , and  $\psi_j(\alpha, \beta)$ , respectively

$$\begin{aligned} s &= \alpha\beta & t &= \frac{(\beta + 1)}{2} & J(\alpha, \beta) &= \frac{\beta}{2} \\ s &= \alpha & t &= \frac{(\alpha(2\beta - 1) + 1)}{2} & J(\alpha, \beta) &= \alpha \\ s &= -\alpha(\beta - 1) & t &= \frac{\beta}{2} & J(\alpha, \beta) &= \frac{-(\beta - 1)}{2} \end{aligned} \quad (225)$$

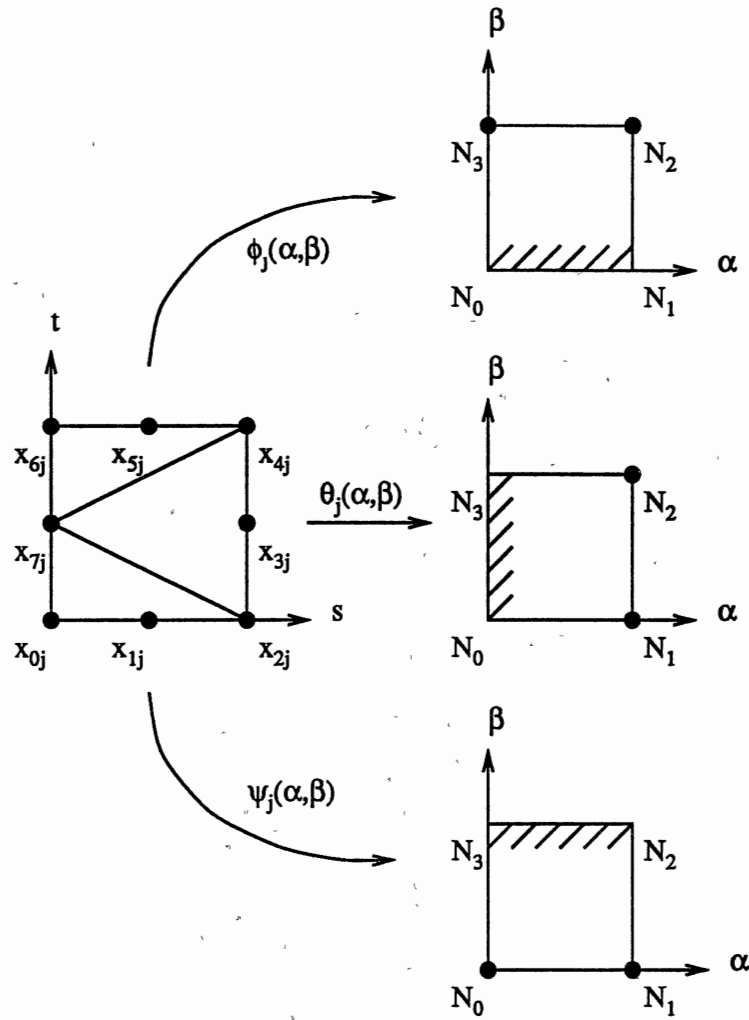


Figure 47. RQUA Singular Integration With Source at Node  $x_{7j}$

When the source is at node  $x_{1j}$ , the transformations are

$$\begin{aligned}
 s &= \frac{\alpha}{2} & t &= -(\alpha - 1)\beta & J(\alpha, \beta) &= \frac{-(\alpha - 1)}{2} \\
 s &= \frac{((2\alpha - 1)\beta + 1)}{2} & t &= \beta & J(\alpha, \beta) &= \beta \\
 s &= \frac{(\alpha + 1)}{2} & t &= \alpha\beta & J(\alpha, \beta) &= \frac{\alpha}{2}
 \end{aligned} \tag{226}$$

When the source is at node  $x_{3j}$ , the transformations are

$$\begin{aligned}
 s &= \alpha - (\alpha - 1)\beta & t &= \frac{\beta}{2} & J(\alpha, \beta) &= \frac{-(\beta - 1)}{2} \\
 s &= \alpha & t &= \frac{-(2(\alpha - 1)\beta - \alpha)}{2} & J(\alpha, \beta) &= 1 - \alpha \\
 s &= (\alpha - 1)\beta + 1 & t &= \frac{(\beta + 1)}{2} & J(\alpha, \beta) &= \frac{\beta}{2}
 \end{aligned} \tag{227}$$

When the source is at node  $x_{5j}$ , the transformations are

$$\begin{aligned}
 s &= \frac{(\alpha + 1)}{2} & t &= \alpha(\beta - 1) + 1 & J(\alpha, \beta) &= \frac{\alpha}{2} \\
 s &= \frac{-((2\alpha - 1)\beta - 2\alpha)}{2} & t &= \beta & J(\alpha, \beta) &= 1 - \beta \\
 s &= \frac{\alpha}{2} & t &= \alpha - (\alpha - 1)\beta & J(\alpha, \beta) &= \frac{-(\alpha - 1)}{2}
 \end{aligned} \tag{228}$$

When the source node is at a corner, the same transformations that were applied to the RLIN element are applied here.

The RCUB element is subdivided into three triangular pieces, similar to the RQUA element. The corner nodes are transformed the same as for the RLIN element.

When the source is at node  $x_{1j}$ , the transformations are

$$\begin{aligned}
 s &= \frac{\alpha}{3} & t &= -(\alpha - 1)\beta & J(\alpha, \beta) &= \frac{-(\alpha - 1)}{3} \\
 s &= \frac{((3\alpha - 1)\beta + 1)}{3} & t &= \beta & J(\alpha, \beta) &= \beta \\
 s &= \frac{(2\alpha + 1)}{3} & t &= \alpha\beta & J(\alpha, \beta) &= \frac{2\alpha}{3}
 \end{aligned} \tag{229}$$



When the source is at node  $x_{2j}$ , the transformations are

$$\begin{aligned}
 s &= \frac{2\alpha}{3} & t &= -(\alpha - 1)\beta & J(\alpha, \beta) &= \frac{-2(\alpha - 1)}{3} \\
 s &= \frac{((3\alpha - 2)\beta + 2)}{3} & t &= \beta & J(\alpha, \beta) &= \beta \\
 s &= \frac{(\alpha + 2)}{3} & t &= \alpha\beta & J(\alpha, \beta) &= \frac{\alpha}{3}
 \end{aligned} \tag{230}$$

When the source is at node  $x_{4j}$ , the transformations are

$$\begin{aligned}
 s &= \alpha - (\alpha - 1)\beta & t &= \frac{\beta}{3} & J(\alpha, \beta) &= \frac{-(\beta - 1)}{3} \\
 s &= \alpha & t &= \frac{-(3(\alpha - 1)\beta - \alpha)}{3} & J(\alpha, \beta) &= 1 - \alpha \\
 s &= (\alpha - 1)\beta + 1 & t &= \frac{(2\beta + 1)}{3} & J(\alpha, \beta) &= \frac{2\beta}{3}
 \end{aligned} \tag{231}$$

When the source is at node  $x_{5j}$ , the transformations are

$$\begin{aligned}
 s &= \alpha - (\alpha - 1)\beta & t &= \frac{2\beta}{3} & J(\alpha, \beta) &= \frac{-2(\beta - 1)}{3} \\
 s &= \alpha & t &= \frac{-(3(\alpha - 1)\beta - 2\alpha)}{3} & J(\alpha, \beta) &= 1 - \alpha \\
 s &= (\alpha - 1)\beta + 1 & t &= \frac{(\beta + 2)}{3} & J(\alpha, \beta) &= \frac{\beta}{3}
 \end{aligned} \tag{232}$$

When the source is at node  $x_{7j}$ , the transformations are

$$\begin{aligned}
 s &= \frac{(\alpha + 2)}{3} & t &= \alpha(\beta - 1) + 1 & J(\alpha, \beta) &= \frac{\alpha}{3} \\
 s &= \frac{-((3\alpha - 2)\beta - 3\alpha)}{3} & t &= \beta & J(\alpha, \beta) &= 1 - \beta \\
 s &= \frac{2\alpha}{3} & t &= \alpha - (\alpha - 1)\beta & J(\alpha, \beta) &= \frac{-2(\alpha - 1)}{3}
 \end{aligned} \tag{233}$$

When the source is at node  $x_8$ , the transformations are

$$\begin{aligned}
 s &= \frac{(2\alpha + 1)}{3} & t &= \alpha(\beta - 1) + 1 & J(\alpha, \beta) &= \frac{2\alpha}{3} \\
 s &= \frac{-((3\alpha - 1)\beta - 3\alpha)}{3} & t &= \beta & J(\alpha, \beta) &= 1 - \beta \\
 s &= \frac{\alpha}{3} & t &= \alpha - (\alpha - 1)\beta & J(\alpha, \beta) &= \frac{-(\alpha - 1)}{3}
 \end{aligned} \tag{234}$$

When the source is at node  $x_{10}$ , the transformations are

$$\begin{aligned}
 s &= \alpha\beta & t &= \frac{(\beta + 2)}{3} & J(\alpha, \beta) &= \frac{\beta}{3} \\
 s &= \alpha & t &= \frac{(\alpha(3\beta - 2) + 2)}{3} & J(\alpha, \beta) &= \alpha \\
 s &= -\alpha(\beta - 1) & t &= \frac{2\beta}{3} & J(\alpha, \beta) &= \frac{-2(\beta - 1)}{3}
 \end{aligned} \tag{235}$$

Finally, when the source is at node  $x_{11}$ , the transformations are

$$\begin{aligned}
 s &= \alpha\beta & t &= \frac{(2\beta + 1)}{3} & J(\alpha, \beta) &= \frac{2\beta}{3} \\
 s &= \alpha & t &= \frac{(\alpha(3\beta - 1) + 1)}{3} & J(\alpha, \beta) &= \alpha \\
 s &= -\alpha(\beta - 1) & t &= \frac{\beta}{3} & J(\alpha, \beta) &= \frac{-(\beta - 1)}{3}
 \end{aligned} \tag{236}$$

# Chapter VII

## THREE DIMENSIONAL CRACK TIP BOUNDARY ELEMENTS

The three dimensional crack tip Overhauser elements, methods for integration, and methods for stress intensity factor calculation will be examined in this chapter.

### Derivation

All of the three dimensional Overhauser crack tip elements will be derived using the Coons approach outlined in Chapter VI. However, the notation will be changed slightly to emphasize that the curves along adjacent edges may be of different types as shown in Figure 48. The revised Coons surface patch equation is

$$\begin{aligned}
 S(s, t) = & C(0, t)\beta_0(s) + C(1, t)\beta_1(s) \\
 & + D(s, 0)\beta_0(t) + D(s, 1)\beta_1(t) \\
 & - P(0, 0)\beta_0(s)\beta_0(t) - P(0, 1)\beta_0(s)\beta_1(t) \\
 & - P(1, 0)\beta_1(s)\beta_0(t) - P(1, 1)\beta_1(s)\beta_1(t)
 \end{aligned} \tag{237}$$

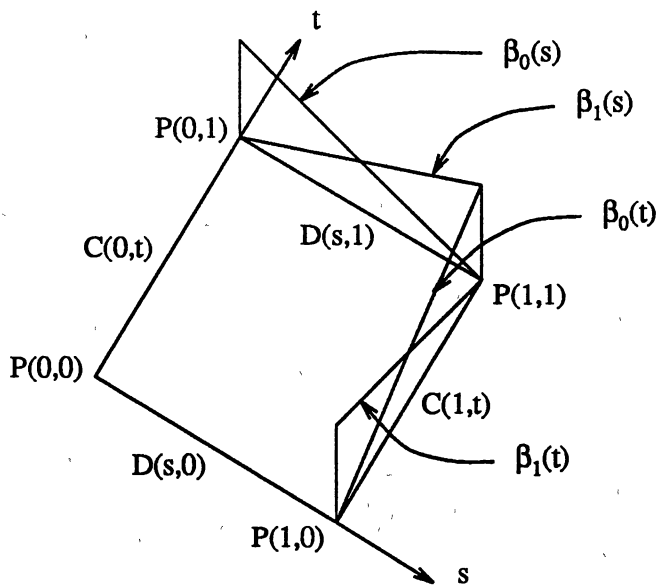


Figure 48. Crack Tip Coons Surface Configuration

where the blending functions are the cubic Hermite polynomials, Equation 193, repeated here for completeness:

$$\begin{aligned}\beta_0(t) &= 1 - 3t^2 + 2t^3 \\ \beta_1(t) &= 3t^2 - 2t^3\end{aligned}\tag{238}$$

Equation 237 is then factored into the geometry, displacement, and traction shape functions as usual.

## Rectangular Side Overhauser Crack Tip (CTROVRS) Element

The Rectangular Side OVerhauser Crack Tip element will be abbreviated CTROVRS. The crack front of the element, as shown in Figure 49 by the thick

line, is placed along the middle of a three dimensional crack. The geometry shape functions are the same as for the ROVRS element given in Equation 195.

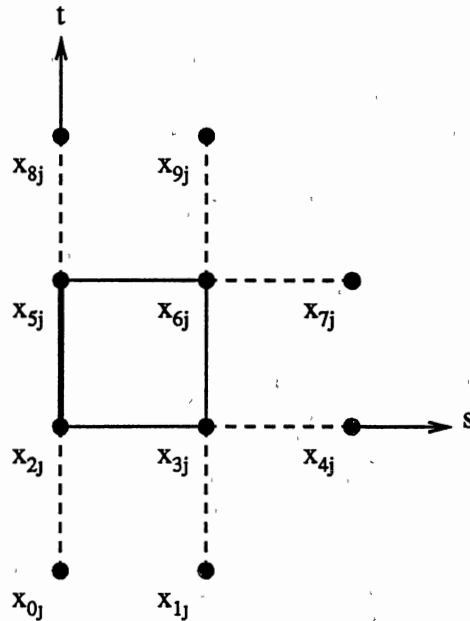


Figure 49. CTROVRS Element Geometry

The displacement shape functions are derived from Equation 237 where  $C(0, t)$  and  $C(1, t)$  are the OVER displacement shape functions,  $D(s, 0)$  and  $D(s, 1)$  are the CTOVR displacement functions, and  $\beta_i(t)$  are given by Equation 238. Upon examination of Equation 237, the CTROVRS displacement shape functions may be

written directly as follows:

$$\begin{aligned}
C_i^u(t) &= N_i^g(t) \\
N_0^g(t) &= \frac{-(t-1)^2 t}{2} \\
N_1^g(t) &= \frac{(t-1)(3t^2 - 2t - 2)}{2} \\
N_2^g(t) &= \frac{-t(3t^2 - 4t - 1)}{2} \\
N_3^g(t) &= \frac{(t-1)t^2}{2}
\end{aligned} \tag{239}$$

$$\begin{aligned}
D_i^u(s) &= N_i^u(t) \\
N_0^u(t) &= \sqrt{t+1}((\sqrt{2}+1)(t+1) + \sqrt{2}+2) - 2(\sqrt{2}+2)(t+1) + 2 \\
N_1^u(t) &= \sqrt{t+1}(-2(\sqrt{2}+1)(t+1) - 2(\sqrt{2}+2)) + (4\sqrt{2}+7)(t+1) - 1 \\
N_2^u(t) &= \sqrt{t+1}((\sqrt{2}+1)(t+1) + \sqrt{2}+2) - (2\sqrt{2}+3)(t+1)
\end{aligned} \tag{240}$$

$$\begin{aligned}
N_0^u(s, t) &= C_0^u(t)\beta_0(s) \\
N_1^u(s, t) &= C_0^u(t)\beta_1(s) \\
N_2^u(s, t) &= D_0^u(s)\beta_0(t) + C_1^u(t)\beta_0(s) - \beta_0(t)\beta_0(s) \\
N_3^u(s, t) &= D_1^u(s)\beta_0(t) + C_1^u(t)\beta_1(s) - \beta_0(t)\beta_1(s) \\
N_4^u(s, t) &= D_2^u(s)\beta_0(t) \\
N_5^u(s, t) &= D_0^u(s)\beta_1(t) + C_2^u(t)\beta_0(s) - \beta_1(t)\beta_0(s) \\
N_6^u(s, t) &= D_1^u(s)\beta_1(t) + C_2^u(t)\beta_1(s) - \beta_1(t)\beta_1(s) \\
N_7^u(s, t) &= D_2^u(s)\beta_1(t) \\
N_8^u(s, t) &= C_3^u(t)\beta_0(s) \\
N_9^u(s, t) &= C_3^u(t)\beta_1(s)
\end{aligned} \tag{241}$$

In general, the CTROVRS displacement shape functions look like the ROVRS geometry shape functions.

The traction shape functions are derived from Equation 237 where  $C(0, t)$  and  $C(1, t)$  are the OVER traction shape functions,  $D(s, 0)$  and  $D(s, 1)$  are the CTOVR traction functions, and  $\beta_i(t)$  are given by Equation 238. Upon examination of Equation 237, the CTROVRS traction shape functions may be written directly as follows:

$$\begin{aligned}
 C_i^p(t) &= N_i^g(t) \\
 N_0^g(t) &= \frac{-(t-1)^2 t}{2} \\
 N_1^g(t) &= \frac{(t-1)(3t^2 - 2t - 2)}{2} \\
 N_2^g(t) &= \frac{-t(3t^2 - 4t - 1)}{2} \\
 N_3^g(t) &= \frac{(t-1)t^2}{2}
 \end{aligned} \tag{242}$$

$$\begin{aligned}
 D_i^p(s) &= N_i^p(t) \\
 N_0^p(t) &= \frac{(\sqrt{t+1}((\sqrt{2}+1)(t+1) + \sqrt{2}+2) - 2(\sqrt{2}+2)(t+1) + 2)}{\sqrt{t}} \\
 N_1^p(t) &= \frac{(\sqrt{t+1}((\sqrt{2}+2)(t+1) + 3(3\sqrt{2}+4)) - (6\sqrt{2}+7)(t+1) - 4\sqrt{2}-7)}{\sqrt{t}} \\
 N_2^p(t) &= \frac{(\sqrt{t+1}((\sqrt{2}+1)(t+1) + \sqrt{2}+2) - (2\sqrt{2}+3)(t+1))}{\sqrt{t}}
 \end{aligned} \tag{243}$$

$$\begin{aligned}
N_0^p(s, t) &= C_0^p(t)\beta_0(s) \\
N_1^p(s, t) &= C_0^p(t)\beta_1(s) \\
N_2^p(s, t) &= D_0^p(s)\beta_0(t) + C_1^p(t)\beta_0(s) - \beta_0(t)\beta_0(s) \\
N_3^p(s, t) &= D_1^p(s)\beta_0(t) + C_1^p(t)\beta_1(s) - \beta_0(t)\beta_1(s) \\
N_4^p(s, t) &= D_2^p(s)\beta_0(t) \\
N_5^p(s, t) &= D_0^p(s)\beta_1(t) + C_2^p(t)\beta_0(s) - \beta_1(t)\beta_0(s) \\
N_6^p(s, t) &= D_1^p(s)\beta_1(t) + C_2^p(t)\beta_1(s) - \beta_1(t)\beta_1(s) \\
N_7^p(s, t) &= D_2^p(s)\beta_1(t) \\
N_8^p(s, t) &= C_3^p(t)\beta_0(s) \\
N_9^p(s, t) &= C_3^p(t)\beta_1(s)
\end{aligned} \tag{244}$$

Plots of  $N_2^p(s, t)$  and  $N_3^p(s, t)$  are given in Figures 50 and 51.

## Rectangular Corner Overhauser Crack Tip (CTROVRC) Element

The Rectangular Corner OVerhauser Crack Tip element will be abbreviated CTROVRC. The crack front of the element, as shown in Figure 52 by the thick line, is placed along the end of a three dimensional crack. The geometry shape functions are the same as for the ROVRC element given in Equation 195.

The displacement shape functions are derived from Equation 237 where  $C(0, t)$  and  $C(1, t)$  are the OVRL geometry shape functions,  $D(s, 0)$  and  $D(s, 1)$  are the CTOVR displacement functions, and  $\beta_i(t)$  are given by Equation 238. Upon examination of Equation 237, the CTROVRC displacement shape functions may be written



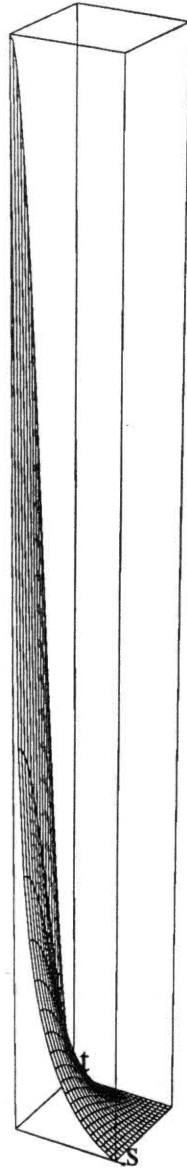


Figure 50. CTROVRS  $N_2^g(s, t)$  Shape Function

directly as follows:

$$\begin{aligned}
 C_i^u(t) &= N_i^g(t) \\
 N_0^g(t) &= \frac{(t-2)(t-1)}{2} \\
 N_1^g(t) &= -(t-2)t \\
 N_2^g(t) &= \frac{(t-1)t}{2}
 \end{aligned}
 \tag{245}$$

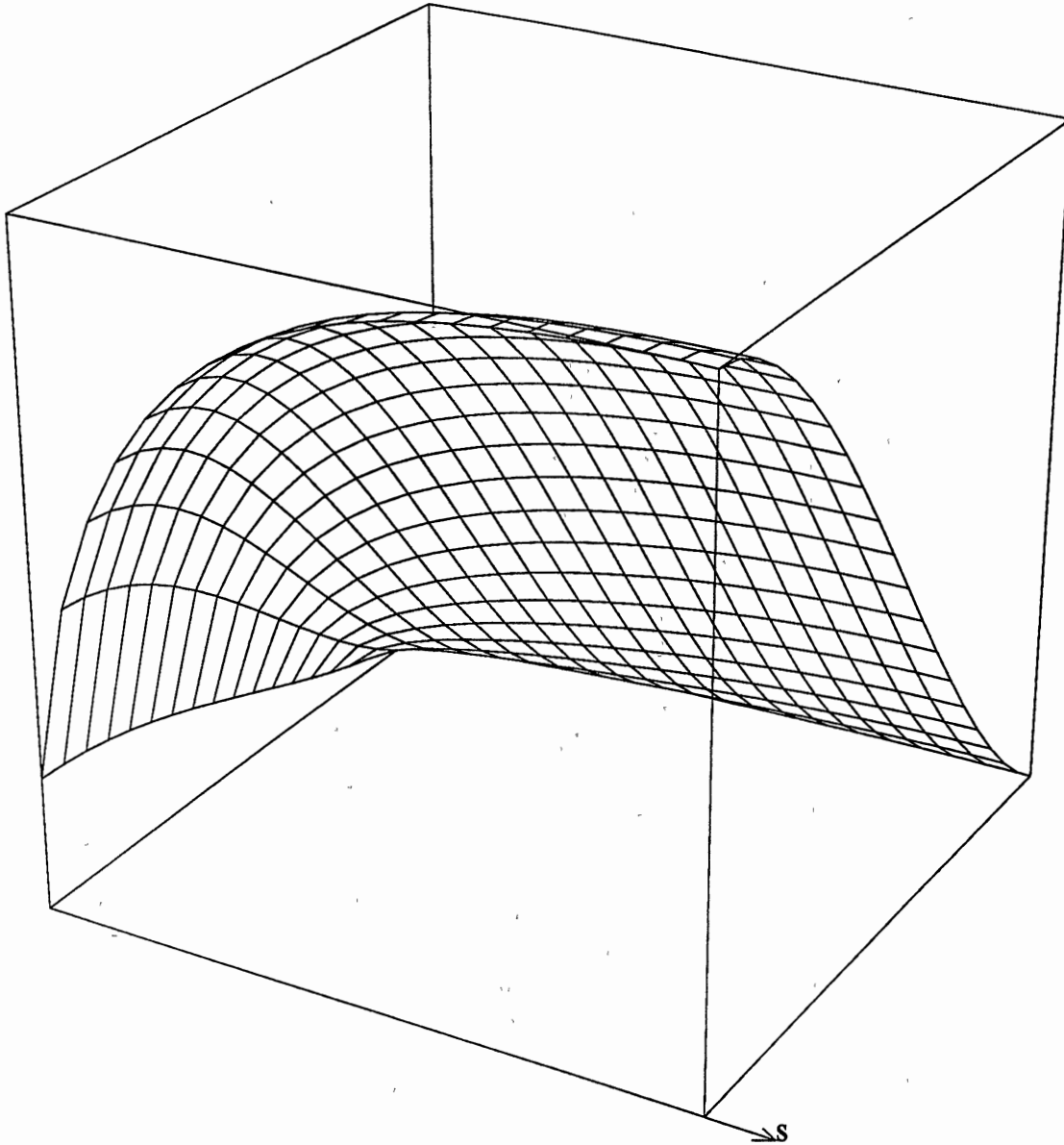


Figure 51. CTROVRS  $N_3^p(s, t)$  Shape Function

$$D_i^u(s) = N_i^u(t)$$

$$N_0^u(t) = \sqrt{t+1}((\sqrt{2}+1)(t+1) + \sqrt{2}+2) - 2(\sqrt{2}+2)(t+1) + 2 \quad (246)$$

$$N_1^u(t) = \sqrt{t+1}(-2(\sqrt{2}+1)(t+1) - 2(\sqrt{2}+2)) + (4\sqrt{2}+7)(t+1) - 1$$

$$N_2^u(t) = \sqrt{t+1}((\sqrt{2}+1)(t+1) + \sqrt{2}+2) - (2\sqrt{2}+3)(t+1)$$

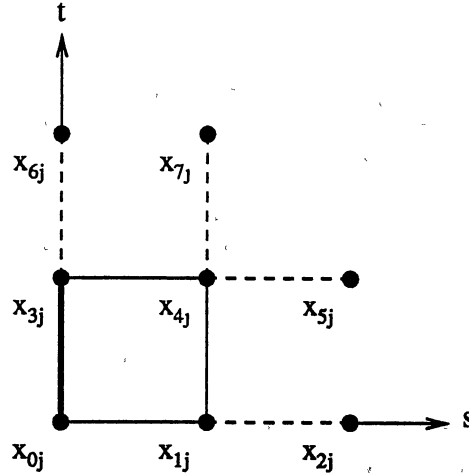


Figure 52. CTROVRC Element Geometry

$$\begin{aligned}
 N_0^u(s, t) &= D_0^u(s)\beta_0(t) + C_0^u(t)\beta_0(s) - \beta_0(t)\beta_0(s) \\
 N_1^u(s, t) &= D_1^u(s)\beta_0(t) + C_0^u(t)\beta_1(s) - \beta_0(t)\beta_1(s) \\
 N_2^u(s, t) &= D_2^u(s)\beta_0(t) \\
 N_3^u(s, t) &= D_0^u(s)\beta_1(t) + C_1^u(t)\beta_0(s) - \beta_1(t)\beta_0(s) \\
 N_4^u(s, t) &= D_1^u(s)\beta_1(t) + C_1^u(t)\beta_1(s) - \beta_1(t)\beta_1(s) \\
 N_5^u(s, t) &= D_2^u(s)\beta_1(t) \\
 N_6^u(s, t) &= C_2^u(t)\beta_0(s) \\
 N_7^u(s, t) &= C_2^u(t)\beta_1(s)
 \end{aligned} \tag{247}$$

In general, the CTROVRC displacement shape functions look like the ROVRC geometry shape functions.

The traction shape functions are derived from Equation 237 where  $C(0, t)$  and  $C(1, t)$  are the OVRL geometry shape functions,  $D(s, 0)$  and  $D(s, 1)$  are the CTOVR

traction functions, and  $\beta_i(t)$  are given by Equation 238. Upon examination of Equation 237, the CTROVRC traction shape functions may be written directly as follows:

$$\begin{aligned}
 C_i^p(t) &= N_i^g(t) \\
 N_0^g(t) &= \frac{(t-2)(t-1)}{2} \\
 N_1^g(t) &= -(t-2)t \\
 N_2^g(t) &= \frac{(t-1)t}{2}
 \end{aligned} \tag{248}$$

$$\begin{aligned}
 D_i^p(s) &= N_i^p(t) \\
 N_0^p(t) &= \frac{(\sqrt{t+1}((\sqrt{2}+1)(t+1) + \sqrt{2}+2) - 2(\sqrt{2}+2)(t+1) + 2)}{\sqrt{t}} \\
 N_1^p(t) &= \frac{(\sqrt{t+1}((\sqrt{2}+2)(t+1) + 3(3\sqrt{2}+4)) - (6\sqrt{2}+7)(t+1) - 4\sqrt{2}-7)}{\sqrt{t}} \\
 N_2^p(t) &= \frac{(\sqrt{t+1}((\sqrt{2}+1)(t+1) + \sqrt{2}+2) - (2\sqrt{2}+3)(t+1))}{\sqrt{t}}
 \end{aligned} \tag{249}$$

$$\begin{aligned}
 N_0^p(s, t) &= D_0^p(s)\beta_0(t) + C_0^p(t)\beta_0(s) - \beta_0(t)\beta_0(s) \\
 N_1^p(s, t) &= D_1^p(s)\beta_0(t) + C_0^p(t)\beta_1(s) - \beta_0(t)\beta_1(s) \\
 N_2^p(s, t) &= D_2^p(s)\beta_0(t) \\
 N_3^p(s, t) &= D_0^p(s)\beta_1(t) + C_1^p(t)\beta_0(s) - \beta_1(t)\beta_0(s) \\
 N_4^p(s, t) &= D_1^p(s)\beta_1(t) + C_1^p(t)\beta_1(s) - \beta_1(t)\beta_1(s) \\
 N_5^p(s, t) &= D_2^p(s)\beta_1(t) \\
 N_6^p(s, t) &= C_2^p(t)\beta_0(s) \\
 N_7^p(s, t) &= C_2^p(t)\beta_1(s)
 \end{aligned} \tag{250}$$

Plots of  $N_0^p(s, t)$  and  $N_1^p(s, t)$  are given in Figures 53 and 54.

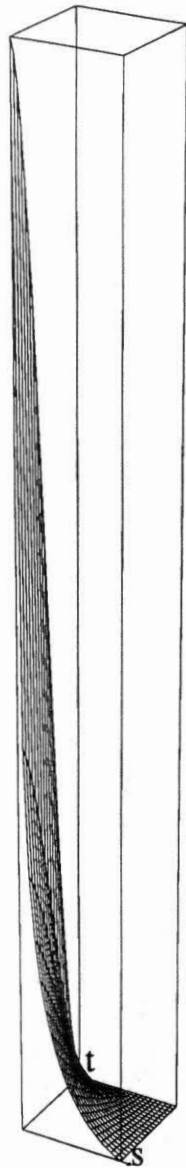


Figure 53. CTROVRC  $N_0^P(s, t)$  Shape Function

## Rectangular Corner Overhauser Crack

### Tip Variant (CTROVRCV) Element

The Rectangular Corner OVerhauser Crack Tip Variant element will be abbreviated CTROVRCV. The crack front of the element, as shown in Figure 55 by

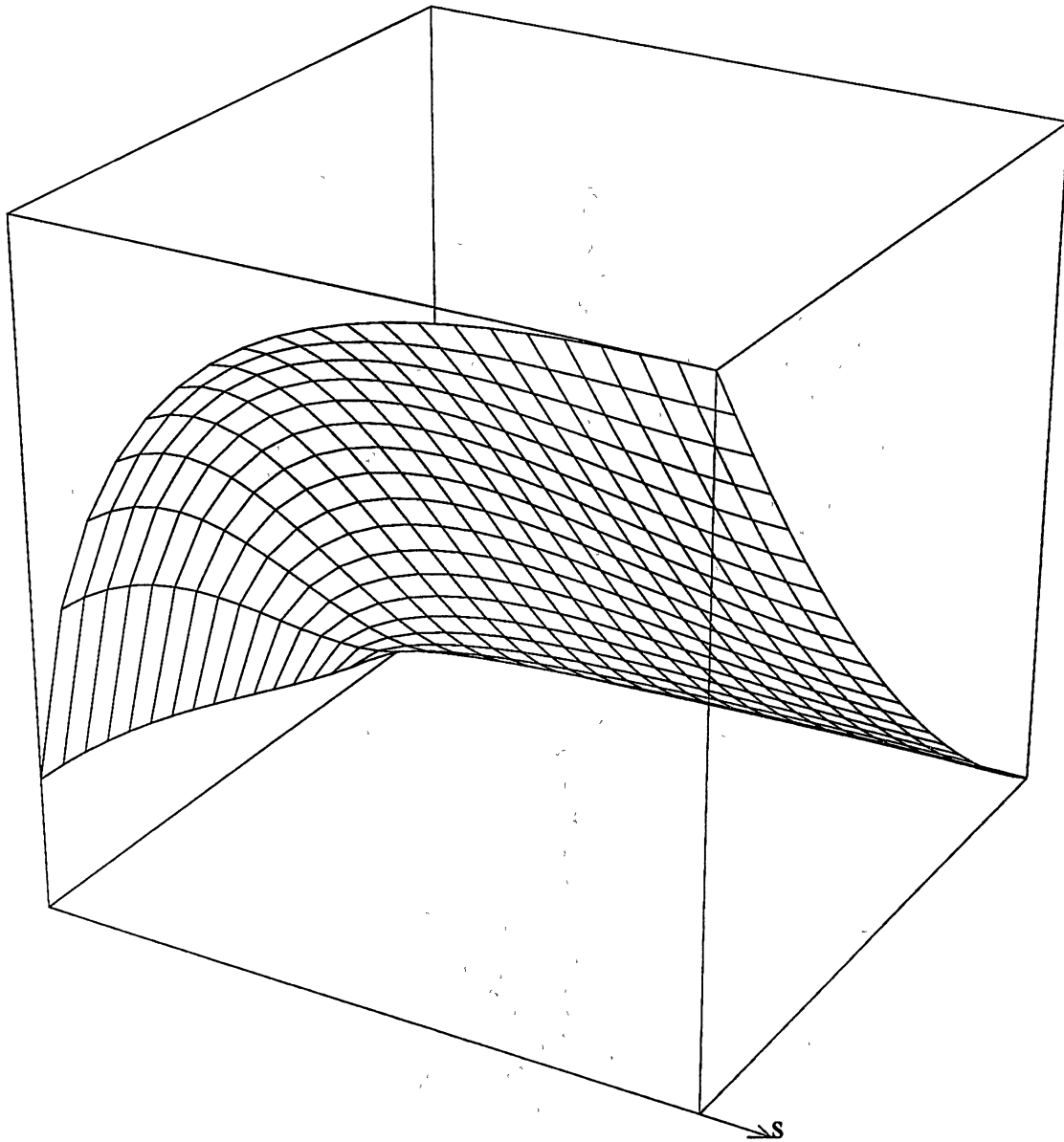


Figure 54. CTROVRC  $N_1^p(s, t)$  Shape Function

the thick line, is placed along the end of a three dimensional crack. This element is useful when the geometry of the problem would cause the CTROVRC element's normal to point in the wrong direction. The geometry shape functions are the same as for the ROVRC element given in Equation 195.

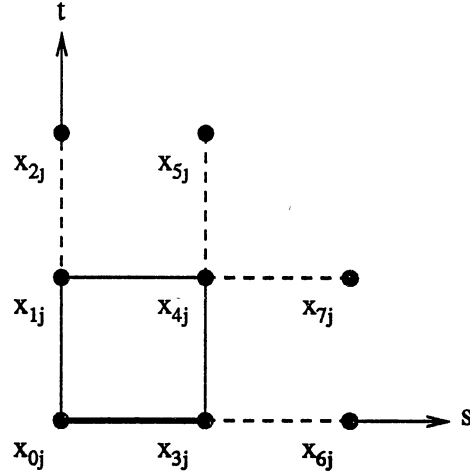


Figure 55. CTROVRCV Element Geometry

The displacement shape functions are derived from Equation 237 where  $C(0, t)$  and  $C(1, t)$  are the OVRL geometry shape functions,  $D(s, 0)$  and  $D(s, 1)$  are the CTOVR displacement functions, and  $\beta_i(t)$  are given by Equation 238. Upon examination of Equation 237, the CTROVRCV displacement shape functions may be written directly as follows:

$$C_i^u(t) = N_i^u(t)$$

$$N_0^u(t) = \sqrt{t+1}((\sqrt{2}+1)(t+1) + \sqrt{2}+2) - 2(\sqrt{2}+2)(t+1) + 2 \quad (251)$$

$$N_1^u(t) = \sqrt{t+1}(-2(\sqrt{2}+1)(t+1) - 2(\sqrt{2}+2)) + (4\sqrt{2}+7)(t+1) - 1$$

$$N_2^u(t) = \sqrt{t+1}((\sqrt{2}+1)(t+1) + \sqrt{2}+2) - (2\sqrt{2}+3)(t+1)$$

$$\begin{aligned}
D_i^u(s) &= N_i^g(t) \\
N_0^g(t) &= \frac{(t-2)(t-1)}{2} \\
N_1^g(t) &= -(t-2)t \\
N_2^g(t) &= \frac{(t-1)t}{2}
\end{aligned} \tag{252}$$

$$\begin{aligned}
N_0^u(s, t) &= D_0^u(s)\beta_0(t) + C_0^u(t)\beta_0(s) - \beta_0(t)\beta_0(s) \\
N_1^u(s, t) &= D_0^u(s)\beta_1(t) + C_1^u(t)\beta_0(s) - \beta_1(t)\beta_0(s) \\
N_2^u(s, t) &= C_2^u(t)\beta_0(s) \\
N_3^u(s, t) &= D_1^u(s)\beta_0(t) + C_0^u(t)\beta_1(s) - \beta_0(t)\beta_1(s) \\
N_4^u(s, t) &= D_1^u(s)\beta_1(t) + C_1^u(t)\beta_1(s) - \beta_1(t)\beta_1(s) \\
N_5^u(s, t) &= C_2^u(t)\beta_1(s) \\
N_6^u(s, t) &= D_2^u(s)\beta_0(t) \\
N_7^u(s, t) &= D_2^u(s)\beta_1(t)
\end{aligned} \tag{253}$$

In general, the CTROVRCV displacement shape functions look like the ROVRCV geometry shape functions.

The traction shape functions are derived from Equation 237 where  $C(0, t)$  and  $C(1, t)$  are the OVRL geometry shape functions,  $D(s, 0)$  and  $D(s, 1)$  are the CTOVR



traction functions, and  $\beta_i(t)$  are given by Equation 238. Upon examination of Equation 237, the CTROVRCV traction shape functions may be written directly as follows:

$$\begin{aligned}
 C_i^p(t) &= N_i^p(t) \\
 N_0^p(t) &= \frac{(\sqrt{t+1}((\sqrt{2}+1)(t+1) + \sqrt{2}+2) - 2(\sqrt{2}+2)(t+1) + 2)}{\sqrt{t}} \\
 N_1^p(t) &= \frac{(\sqrt{t+1}((\sqrt{2}+2)(t+1) + 3(3\sqrt{2}+4)) - (6\sqrt{2}+7)(t+1) - 4\sqrt{2}-7)}{\sqrt{t}} \\
 N_2^p(t) &= \frac{(\sqrt{t+1}((\sqrt{2}+1)(t+1) + \sqrt{2}+2) - (2\sqrt{2}+3)(t+1))}{\sqrt{t}}
 \end{aligned} \tag{254}$$

$$\begin{aligned}
 D_i^p(s) &= N_i^g(t) \\
 N_0^g(t) &= \frac{(t-2)(t-1)}{2} \\
 N_1^g(t) &= -(t-2)t \\
 N_2^g(t) &= \frac{(t-1)t}{2}
 \end{aligned} \tag{255}$$

$$\begin{aligned}
 N_0^p(s, t) &= D_0^p(s)\beta_0(t) + C_0^p(t)\beta_0(s) - \beta_0(t)\beta_0(s) \\
 N_1^p(s, t) &= D_0^p(s)\beta_1(t) + C_1^p(t)\beta_0(s) - \beta_1(t)\beta_0(s) \\
 N_2^p(s, t) &= C_2^p(t)\beta_0(s) \\
 N_3^p(s, t) &= D_1^p(s)\beta_0(t) + C_0^p(t)\beta_1(s) - \beta_0(t)\beta_1(s) \\
 N_4^p(s, t) &= D_1^p(s)\beta_1(t) + C_1^p(t)\beta_1(s) - \beta_1(t)\beta_1(s) \\
 N_5^p(s, t) &= C_2^p(t)\beta_1(s) \\
 N_6^p(s, t) &= D_2^p(s)\beta_0(t) \\
 N_7^p(s, t) &= D_2^p(s)\beta_1(t)
 \end{aligned} \tag{256}$$

Plots of  $N_0^p(s, t)$  and  $N_1^p(s, t)$  are given in Figures 56 and 57.

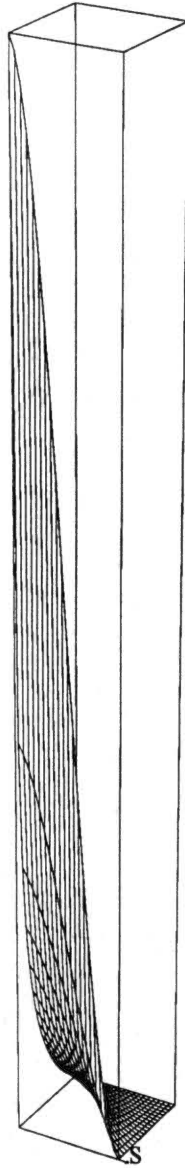


Figure 56. CTROVRCV  $N_0^p(s, t)$  Shape Function

### Integration

The integrations for a three dimensional crack tip boundary element are performed in a manner similar to that of the standard three dimensional boundary element (Chapter VI). However, Equation 205 has a singular integrand on the order of  $\frac{1}{\sqrt{s}}$  as

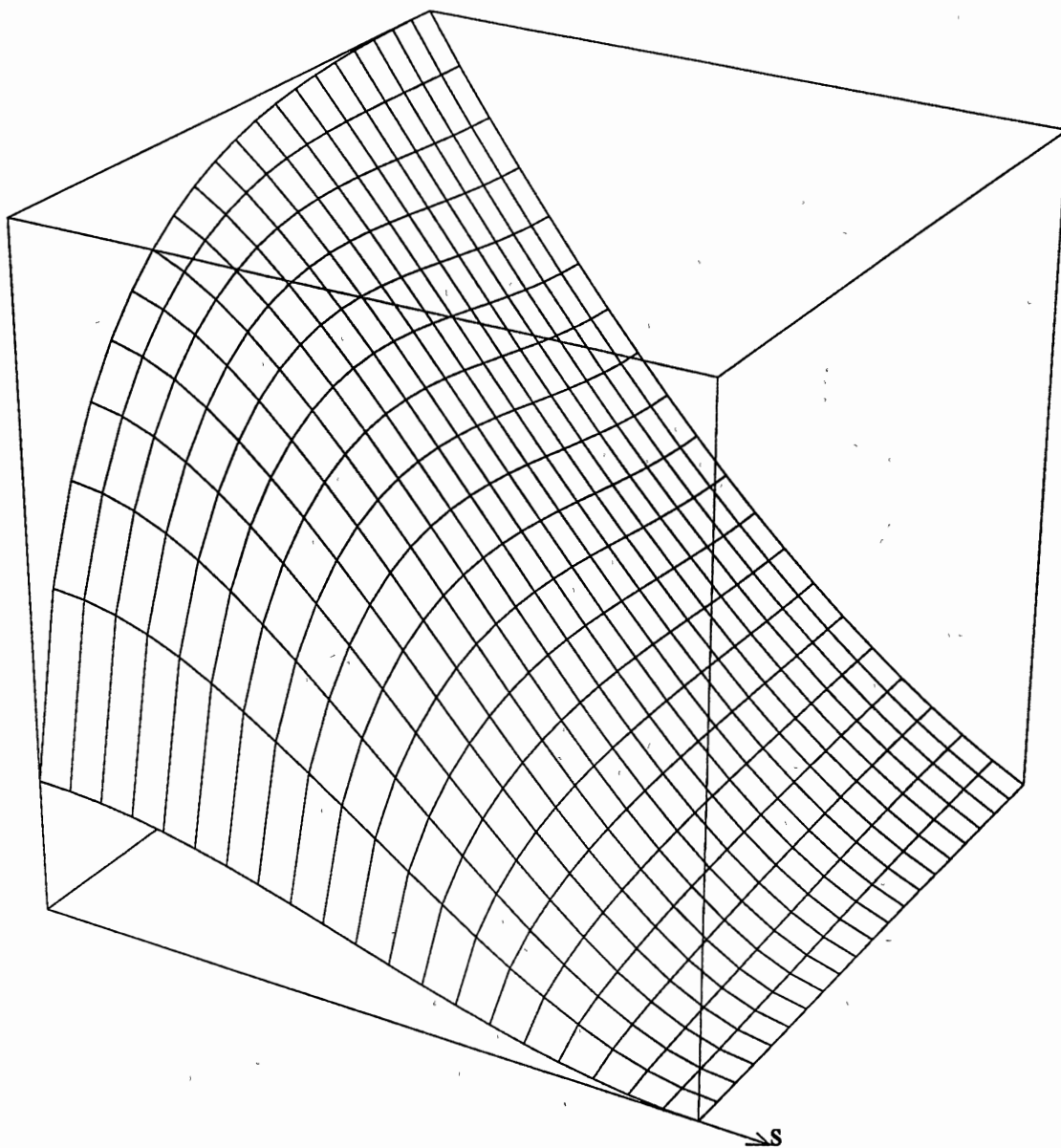


Figure 57. CTROVRCV  $N_1^P(s, t)$  Shape Function

shown:

$$G_{ijl}^e(\zeta, s, t) = O \left( \iint \left[ \frac{1}{r(\zeta, s, t)\sqrt{s}} + \frac{r_i(s, t)r_j(s, t)}{r^3(\zeta, s, t)\sqrt{s}} \right] N_l^P(s, t) J(s, t) ds dt \right) \quad (257)$$

Because the integral exists, the singularity may be eliminated through an appropriate mapping of  $s$ . One such mapping for the CTROVRS and CTROVRC elements is

$$s = \alpha^2 \quad ds = 4\alpha^3 d\alpha \quad (258)$$

The CTROVRCV element has an  $\frac{1}{\sqrt{t}}$  singularity and an appropriate mapping is

$$t = \beta^2 \quad dt = 4\beta^3 d\beta \quad (259)$$

This same mapping may be applied to Equation 204 without detrimental effect.

### Singular Integration

Most of the methods for performing the integration with singular integrands for three dimensional crack tip boundary elements involve an element subdivision into triangles and then a transformation of coordinates to eliminate the singularity. Luchi and Rizzuti [44] use an element subdivision and a cartesian coordinate transformation with elemental parameters ranging from  $-1$  to  $1$ . Jia, Shippy, and Rizzo [36] employ an element subdivision, a cartesian coordinate transformation, and a difficult polar transformation over an element with parameters ranging from  $-1$  to  $1$ . These approaches are not applicable to the Overhauser crack tip elements for a number of reasons: the parameter range is different, all transformations needed are not clear from the information given in those papers, and, most importantly, the Overhauser crack tip elements cannot be “rotated around” to get the integrations from similar

nodes. As an example, in many boundary element codes, the singular integrations for node 1 of the RLIN element are performed by “rotating around” the coordinates in real space for node 1 until they were in the place of node 0 and then performing the singular integrations as if the singular node was at node 0. This approach is very similar to the “reversing” strategy used in Chapter V. A new approach was needed that would address the problems outlined above.

The key idea to the new approach is to use element subdivision and a triangle to square mapping approach. However, instead of using the RLIN shape functions for the square, a different set of quadratic shape functions based on the direction of the  $\frac{1}{\sqrt{t}}$  and the location of the singular node is used for the square. This will become more clear as we look at the details.

The behavior that is desired in the “square” part of the triangle to square transformation is to eliminate the  $\frac{1}{\sqrt{t}}$  singularity. This suggests a transformation of the form  $t = \alpha^2$ . Various combinations of transformations of this type will be used to build up a set of shape functions for the “square” part of the triangle to square transformation. Recall from Chapter VI that the RLIN shape functions were used previously. The quadratic shape functions that will be used in various combinations are shown in Figure 58.

The proper combination of quadratic shape functions was derived by inspection, influenced by the fact that  $s = \alpha^2$  was required since that is the “direction” of the singularity. The quadratic shape functions are depicted in Figure 59. Note that they are symmetric with respect to the line  $\beta = \alpha$  and they are the same on opposite

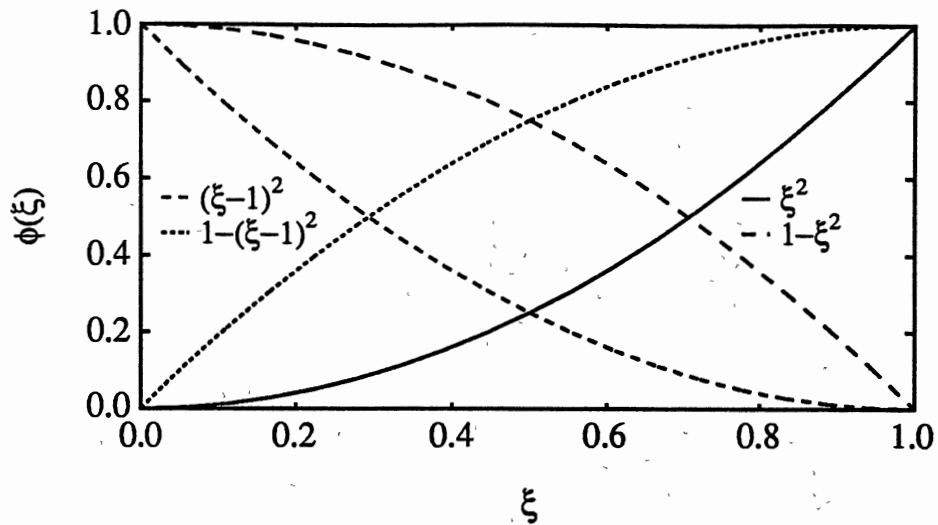


Figure 58. Quadratic Shape Functions for Singular Integration

edges. The “square” shape functions are given in Equation 260 and are valid for the CTROVRS element nodes  $x_{2j}$  and  $x_{6j}$ , the CTROVRC element nodes  $x_{0j}$  and  $x_{4j}$ , and the CTROVRCV element nodes  $x_{0j}$  and  $x_{4j}$ :

$$\begin{aligned}
 N_0(\alpha, \beta) &= (1 - \alpha^2)(1 - \beta^2) \\
 N_1(\alpha, \beta) &= \alpha^2(1 - \beta^2) \\
 N_2(\alpha, \beta) &= \alpha^2\beta^2 \\
 N_3(\alpha, \beta) &= (1 - \alpha^2)\beta^2
 \end{aligned}
 \tag{260}$$

Nodes  $x_{3j}$  and  $x_{5j}$  of the CTROVRS element and nodes  $x_{1j}$  and  $x_{3j}$  of the CTROVRC element require a different set of shape functions. The quadratic shape functions are shown in Figure 60. Note that they are symmetric with respect to the line  $\beta = -\alpha + 1$ . The “square” shape functions are given in Equation 261.

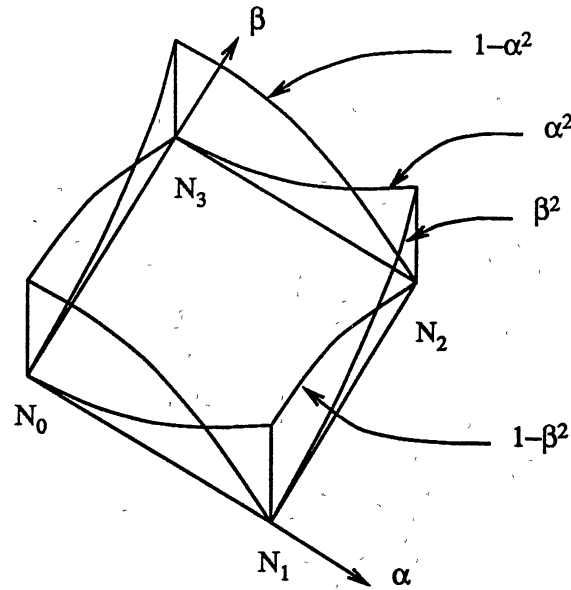


Figure 59. Shape Function Derivation for Triangle to Square Transformation for Crack Tip Overhauser Type Elements

$$\begin{aligned}
 N_0(\alpha, \beta) &= (1 - \alpha^2)(\beta - 1)^2 \\
 N_1(\alpha, \beta) &= \alpha^2(\beta - 1)^2 \\
 N_2(\alpha, \beta) &= \alpha^2(1 - (\beta - 1)^2) \\
 N_3(\alpha, \beta) &= (1 - \alpha^2)(1 - (\beta - 1)^2)
 \end{aligned}
 \tag{261}$$

Nodes  $x_{3j}$  and  $x_{1j}$  of the CTROVRCV element require yet another different set of shape functions because the direction of the singularity is along  $\beta$  not  $\alpha$ . The quadratic shape functions are shown in Figure 61. Note that they are again symmetric with respect to the line  $\beta = -\alpha + 1$ . The "square" shape functions are given in

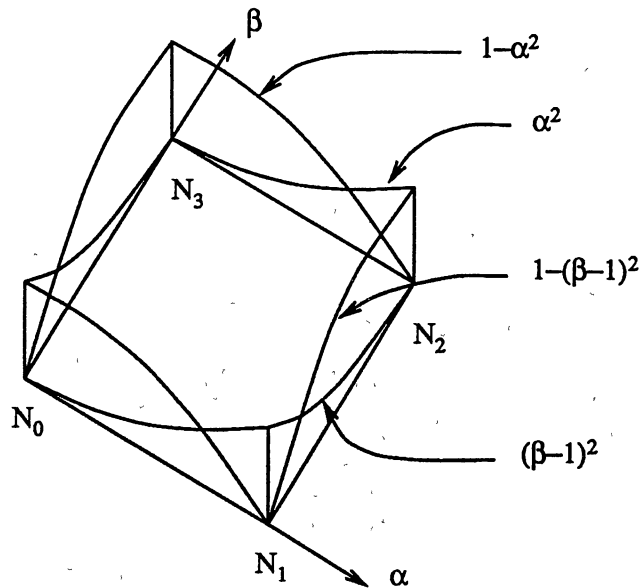


Figure 60. Shape Function Derivation for Triangle to Square Transformation for the CTROVRS and CTROVRC Element

Equation 261.

$$\begin{aligned}
 N_0(\alpha, \beta) &= (\alpha - 1)^2(1 - \beta^2) \\
 N_1(\alpha, \beta) &= (1 - (\alpha - 1)^2)(1 - \beta^2) \\
 N_2(\alpha, \beta) &= (1 - (\alpha - 1)^2)\beta^2 \\
 N_3(\alpha, \beta) &= (\alpha - 1)^2\beta^2
 \end{aligned}
 \tag{262}$$

The next step is to perform the subdivision of the elements into triangles and perform the triangle to square transformation as outlined in Chapter VI. The results for the CTROVRS and CTROVRC elements are summarized in the following equations. The transformations for the CTROVRS element node  $x_{2j}$  and the CTROVRC



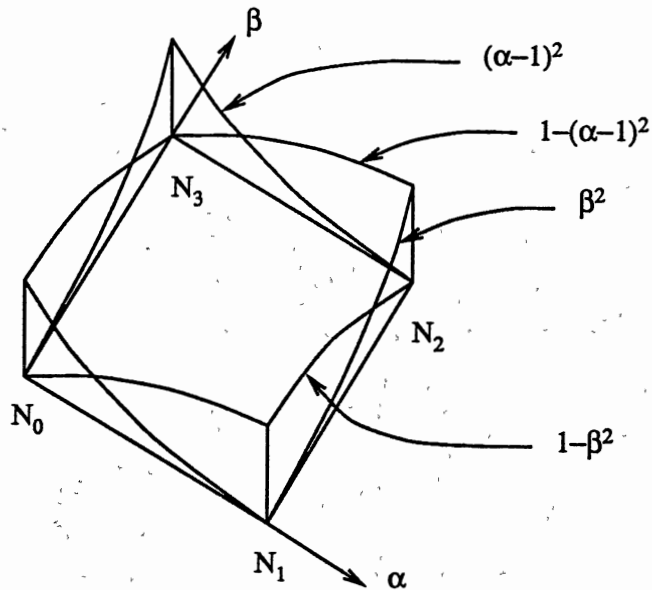


Figure 61. Shape Function Derivation for Triangle to Square Transformation for the CTROVRCV Element

element node  $x_{0j}$  are

$$s = \alpha^2 \beta^2$$

$$t = \beta^2$$

(263)

$$J(\alpha, \beta) = 4\alpha\beta^3$$

and

$$s = \alpha^2$$

$$t = \alpha^2 \beta^2$$

(264)

$$J(\alpha, \beta) = 4\alpha^3 \beta$$

The transformations for the CTROVRS element node  $x_{3j}$  and the CTROVRC element

node  $x_1$ , are

$$\begin{aligned}
 s &= \alpha^2 \\
 t &= (\alpha - 1)(\alpha + 1)(\beta - 2)\beta \\
 J(\alpha, \beta) &= 4(\alpha - 1)\alpha(\alpha + 1)(\beta - 1)
 \end{aligned} \tag{265}$$

and

$$\begin{aligned}
 s &= 1 - (\alpha - 1)(\alpha + 1)(\beta - 2)\beta \\
 t &= -(\beta - 2)\beta \\
 J(\alpha, \beta) &= 4\alpha(\beta - 2)(\beta - 1)\beta
 \end{aligned} \tag{266}$$

The transformations for the CTROVRS element node  $x_6$ , and the CTROVRC element node  $x_4$ , are

$$\begin{aligned}
 s &= \alpha^2 - (\alpha - 1)(\alpha + 1)\beta^2 \\
 t &= \beta^2 \\
 J(\alpha, \beta) &= -4\alpha(\beta - 1)\beta(\beta + 1)
 \end{aligned} \tag{267}$$

and

$$\begin{aligned}
 s &= \alpha^2 \\
 t &= \alpha^2 - (\alpha - 1)(\alpha + 1)\beta^2 \\
 J(\alpha, \beta) &= -4(\alpha - 1)\alpha(\alpha + 1)\beta
 \end{aligned} \tag{268}$$

The transformations for the CTROVRS element node  $x_5$ , and the CTROVRC element node  $x_3$ , are

$$\begin{aligned}
 s &= \alpha^2 \\
 t &= -(\alpha(\beta - 1) - 1)(\alpha(\beta - 1) + 1) \\
 J(\alpha, \beta) &= -4\alpha^3(\beta - 1)
 \end{aligned} \tag{269}$$

and

$$\begin{aligned}
 s &= \alpha^2(\beta - 1)^2 \\
 t &= -(\beta - 2)\beta \\
 J(\alpha, \beta) &= -4\alpha(\beta - 1)^3
 \end{aligned} \tag{270}$$

The results for the CTROVRCV element are summarized in the following equations. The transformations for the CTROVRCV element node  $x_0$ , are

$$\begin{aligned}
 s &= \alpha^2\beta^2 \\
 t &= \beta^2 \\
 J(\alpha, \beta) &= 4\alpha\beta^3
 \end{aligned} \tag{271}$$

and

$$\begin{aligned}
 s &= \alpha^2 \\
 t &= \alpha^2\beta^2 \\
 J(\alpha, \beta) &= 4\alpha^3\beta
 \end{aligned} \tag{272}$$

The transformations for the CTROVRCV element node  $x_{3j}$  are

$$\begin{aligned}
 s &= -(\alpha - 2)\alpha \\
 t &= (\alpha - 1)^2\beta^2 \\
 J(\alpha, \beta) &= -4(\alpha - 1)^3\beta
 \end{aligned} \tag{273}$$

and

$$\begin{aligned}
 s &= -((\alpha - 1)\beta - 1)((\alpha - 1)\beta + 1) \\
 t &= \beta^2 \\
 J(\alpha, \beta) &= -4(\alpha - 1)\beta^3
 \end{aligned} \tag{274}$$

The transformations for the CTROVRCV element node  $x_4$ , are

$$\begin{aligned}
 s &= \alpha^2 - (\alpha - 1)(\alpha + 1)\beta^2 \\
 t &= \beta^2 \\
 J(\alpha, \beta) &= -4\alpha(\beta - 1)\beta(\beta + 1)
 \end{aligned} \tag{275}$$

and

$$\begin{aligned}
 s &= \alpha^2 \\
 t &= \alpha^2 - (\alpha - 1)(\alpha + 1)\beta^2 \\
 J(\alpha, \beta) &= -4(\alpha - 1)\alpha(\alpha + 1)\beta
 \end{aligned} \tag{276}$$

The transformations for the CTROVRCV element node  $x_1$ , are

$$\begin{aligned}
 s &= -(\alpha - 2)\alpha \\
 t &= 1 - (\alpha - 2)\alpha(\beta - 1)(\beta + 1) \\
 J(\alpha, \beta) &= 4(\alpha - 2)(\alpha - 1)\alpha\beta
 \end{aligned} \tag{277}$$

and

$$\begin{aligned}
 s &= (\alpha - 2)\alpha(\beta - 1)(\beta + 1) \\
 t &= \beta^2 \\
 J(\alpha, \beta) &= 4(\alpha - 1)(\beta - 1)\beta(\beta + 1)
 \end{aligned} \tag{278}$$

## Stress Intensity Factor Calculation

The three dimensional Mode I, symmetric, flat crack, stress intensity factors for three dimensional Overhauser-type boundary elements are those that use crack tip traction values. The approach is nearly identical to that used with the two dimensional CTOVR elements; only the nodal indices have changed.

The SIF for the CTROVRS element is calculated from the formula

$$K_I = \sqrt{\pi} M p_{22} \quad (279)$$

$$M = \left[ (-3x_{20} + 4x_{30} - x_{40})^2 + (-3x_{21} + 4x_{31} - x_{41})^2 \right]^{\frac{1}{4}}$$

or

$$K_I = \sqrt{\pi} M p_{52} \quad (280)$$

$$M = \left[ (-3x_{50} + 4x_{60} - x_{70})^2 + (-3x_{51} + 4x_{61} - x_{71})^2 \right]^{\frac{1}{4}}$$

The SIF for the CTROVRC element is calculated from the formula

$$K_I = \sqrt{\pi} M p_{02} \quad (281)$$

$$M = \left[ (-3x_{00} + 4x_{10} - x_{20})^2 + (-3x_{01} + 4x_{11} - x_{21})^2 \right]^{\frac{1}{4}}$$

or

$$K_I = \sqrt{\pi} M p_{32} \quad (282)$$

$$M = \left[ (-3x_{30} + 4x_{40} - x_{50})^2 + (-3x_{31} + 4x_{41} - x_{51})^2 \right]^{\frac{1}{4}}$$

Finally, the SIF for the CTROVRCV element is calculated from the formula

$$K_I = \sqrt{\pi} M p_{02} \quad (283)$$

$$M = \left[ (-3x_{00} + 4x_{30} - x_{60})^2 + (-3x_{01} + 4x_{31} - x_{61})^2 \right]^{\frac{1}{4}}$$

or

$$K_I = \sqrt{\pi} M p_{12} \quad (284)$$

$$M = \left[ (-3x_{10} + 4x_{40} - x_{70})^2 + (-3x_{11} + 4x_{41} - x_{71})^2 \right]^{\frac{1}{4}}$$

## Chapter VIII

### EXAMPLE ANALYSES

In order to verify the correctness and usefulness of the new two and three dimensional crack tip Overhauser boundary elements, they will be compared to the results of a number of well known crack tip problems. Some of these problems have analytical solutions while others were obtained numerically. Some boundary element results from other researchers will be included.

#### Double Edge Cracked Plate

The first example, the finite width plate with double edge cracks, has been used by a number of boundary element researchers [8,46,35]. The plate is shown in Figure 62. The model dimensions and material properties are crack length  $a = 1.8$  in, elastic modulus  $E = 5250.0$  ksi, Poisson's ratio  $\nu = 0.20$ , and load stress  $\sigma_0 = 1$  ksi. An approximate analytical solution accurate to 1% has been reported by Bowie [9] as  $K_I = 2.737$  ksi  $\cdot$  in<sup>1/2</sup>.

Taking advantage of the symmetry of the problem, only one-quarter of the plate needs to be discretized as shown in Figure 63. The boundary element mesh consists of a combination of RQUA elements along the top and sides and Overhauser-type elements along the crack. The arrangement of Overhauser-type elements from left to

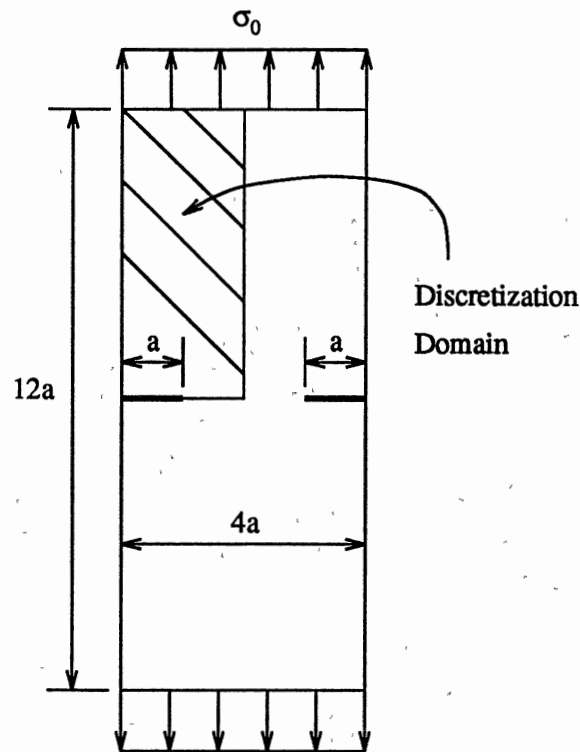


Figure 62. Double Edge Cracked Plate

right is OVRL, OVER, OVER, CTOVRR, CTOVRL, OVER, OVER, and OVR.

The ratio of the length of the crack tip boundary element to the length of the crack  $l/a$  is an important parameter in analyzing the performance of crack tip boundary elements. It is desirable that the SIF values be relatively insensitive to changes in  $l/a$ . It should be noted that, as the form of Equation 179 indicates, the effective length for the CTOVR boundary elements is the distance from node  $x_{0j}$  to  $x_{2j}$ . With this in mind, values for  $K_I$  may be obtained for ratios of  $l/a$  in the range of 0.05 to



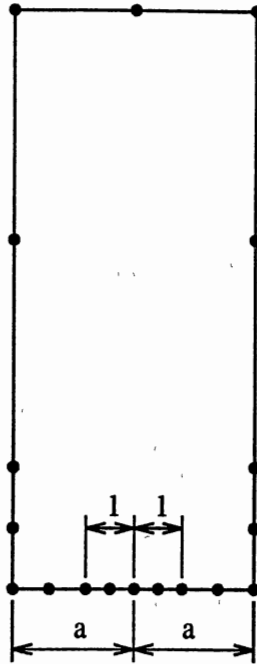


Figure 63. Cracked Plate BEM Mesh

0.9. The percent error is calculated by the formula

$$\text{Percent Error} = \frac{K_{IBEM} - K_I}{K_I} 100 \quad (285)$$

where  $K_I = 2.737 \text{ ksi} \cdot \text{in}^{1/2}$ .

The results for the CTQQ and CTQT elements are plotted in Figure 64. It can be seen that the SIF calculated by the traction method are generally less sensitive to the  $l/a$  ratio.

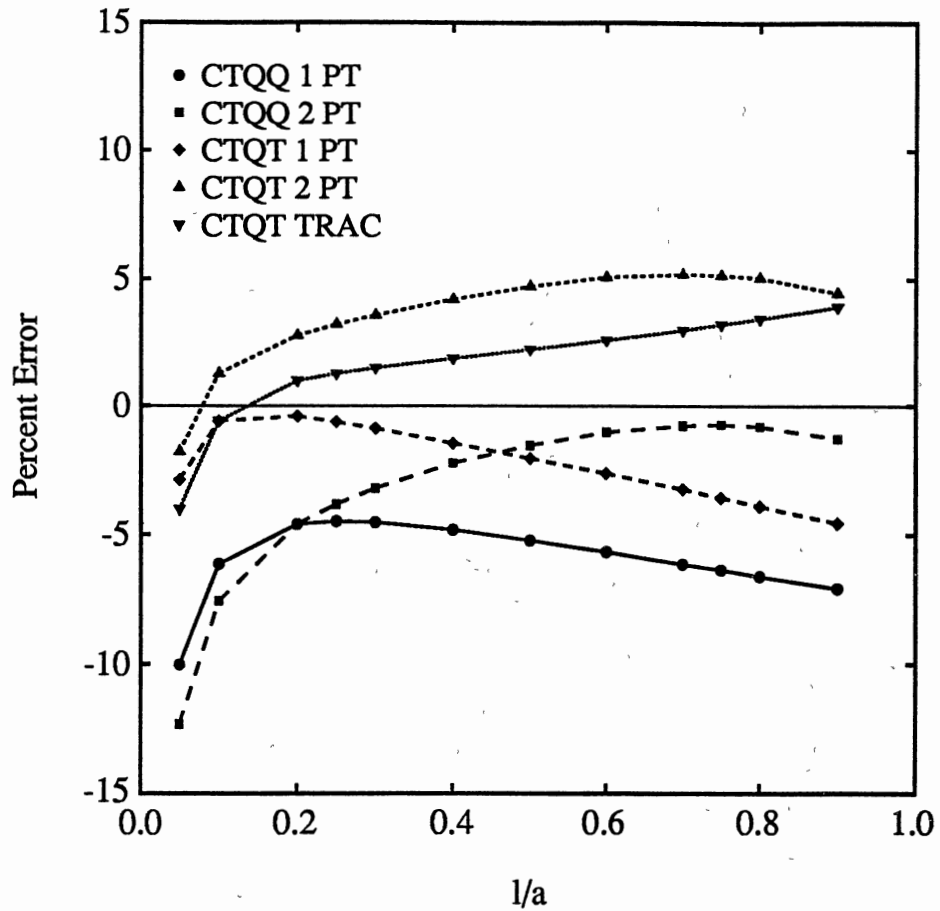


Figure 64. Percent Error in  $K_I$  for Double Edge Cracked Plate With CTQQ and CTQT Elements

The results for the CTQUA element are plotted in Figure 65. Again, the SIF calculated by the traction method are generally less sensitive to the  $l/a$  ratio.

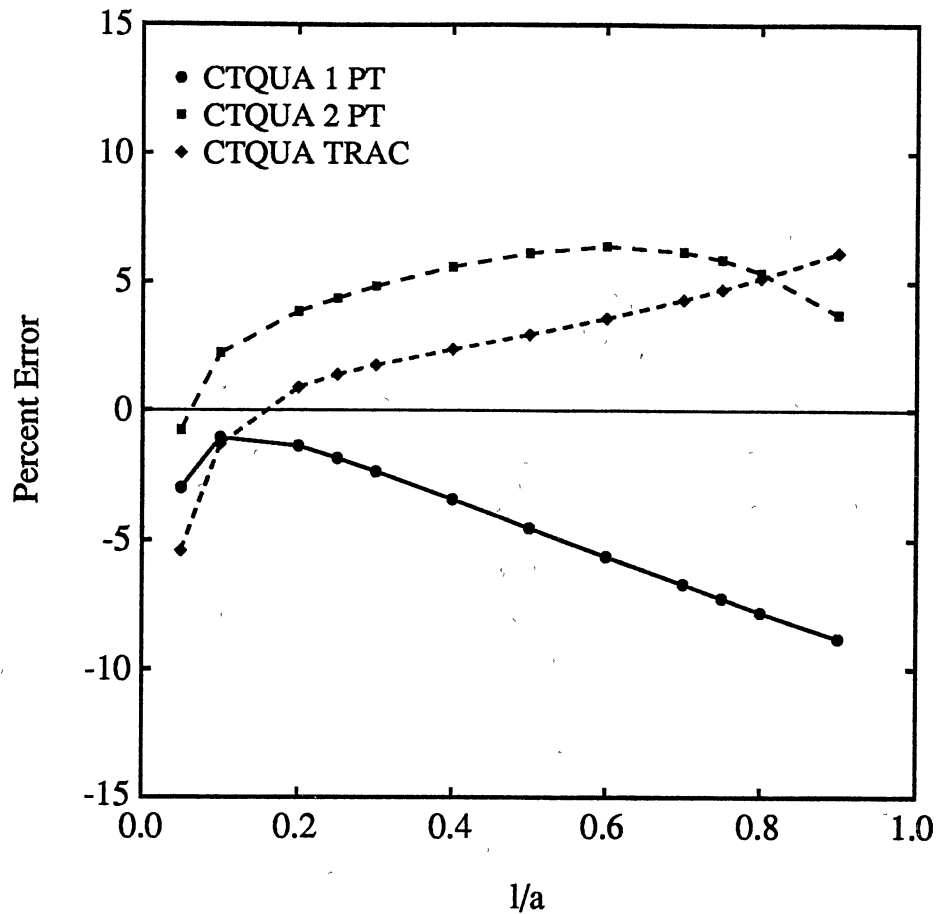


Figure 65. Percent Error in  $K_I$  for Double Edge Cracked Plate With CTQUA Elements

The results for the CTOVR element are plotted in Figure 66. For  $l/a < 0.2$  the SIF are way off. This is due to the parameter in the Overhauser-type element becoming nonmonotonic when two elements that are very different in length are placed next to each other.

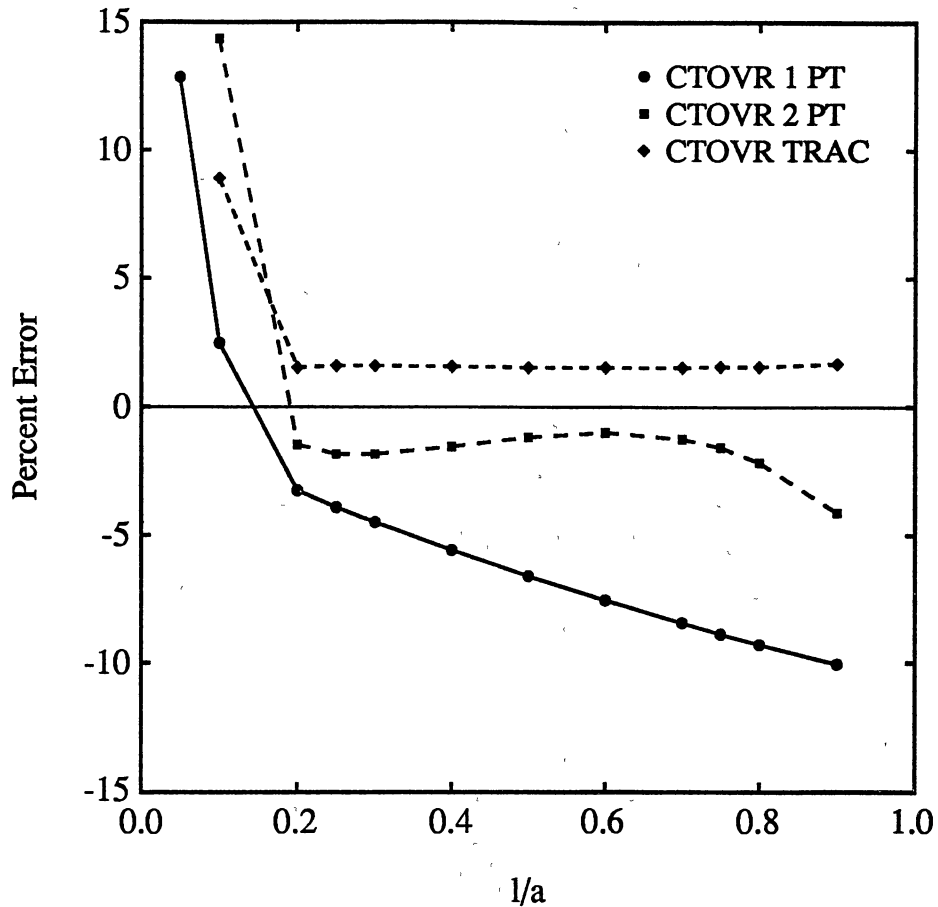


Figure 66. Percent Error in  $K_I$  for Double Edge Cracked Plate With CTOVR Elements

From Figures 64 through 66 it can be seen that the traction method for calculating the SIF is less sensitive to the  $l/a$  ratio. For completeness, a comparison of the SIF calculated by the traction method for the CTQT, CTQUA, and CTOVR elements is given in Figure 67. As shown, for  $l/a \geq 0.2$ , the percent errors are similar; however, the CTOVR element is clearly less sensitive to the  $l/a$  ratio.

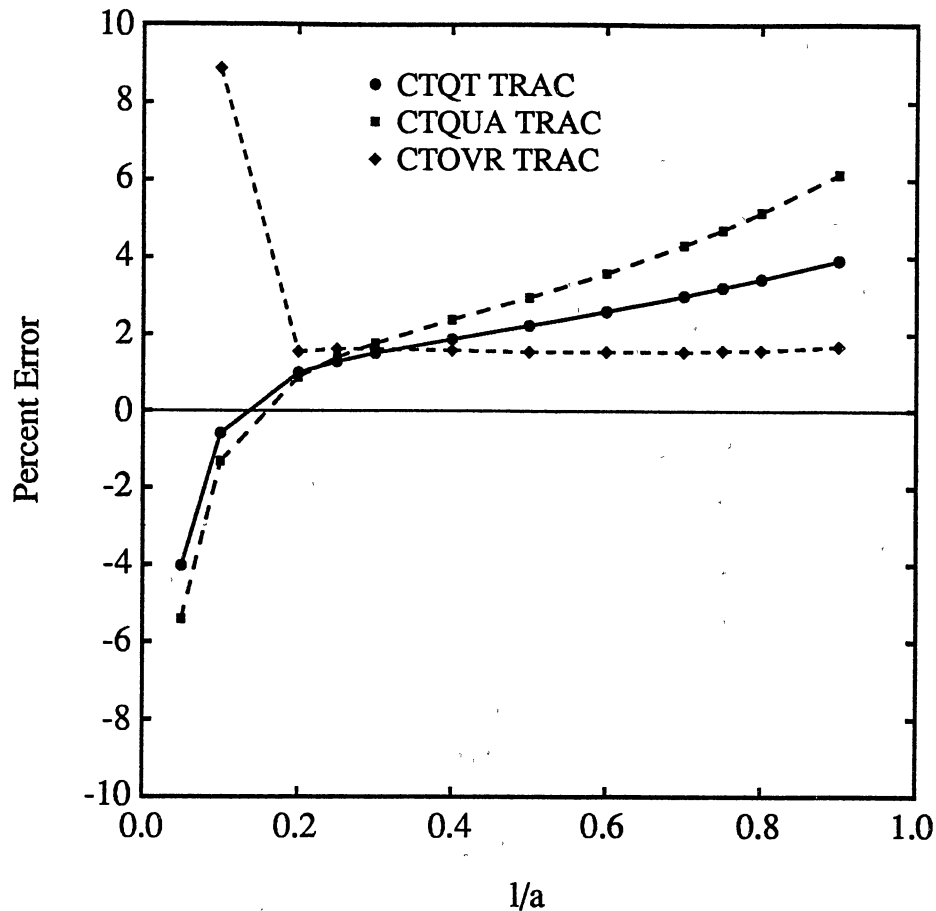


Figure 67. Comparison of Percent Errors in  $K_I$  Calculated by the Traction Method for Double Edge Cracked Plate

### Center Cracked Plate

The finite width center cracked plate, depicted in Figure 68, is very similar to the double edge cracked plate. The same dimensions,  $a = 1.8$  in, material constants,  $E = 5250.0$  ksi and  $\nu = 0.20$ , and loading,  $\sigma_0 = 1$  ksi, are used. Only the boundary conditions on the boundary element mesh (Figure 63) need to be changed. Bowie [9] reports an approximate analytical solution of  $K_I = 2.8298$  that is accurate to 1%.

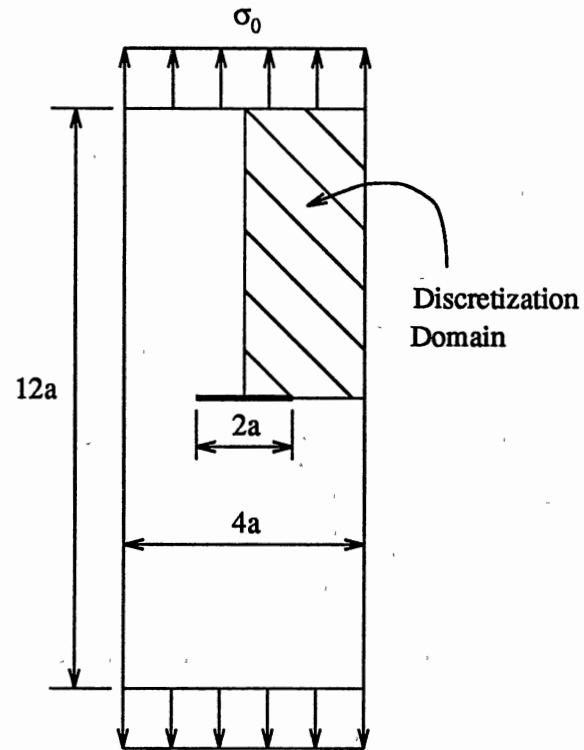


Figure 68. Center Cracked Plate

The percent error is calculated by Equation 285 where  $K_I = 2.8298$ .

The results for the CTQQ and CTQT elements are plotted in Figure 69. It can be seen that the SIF calculated by the traction method are generally less sensitive to the  $l/a$  ratio.

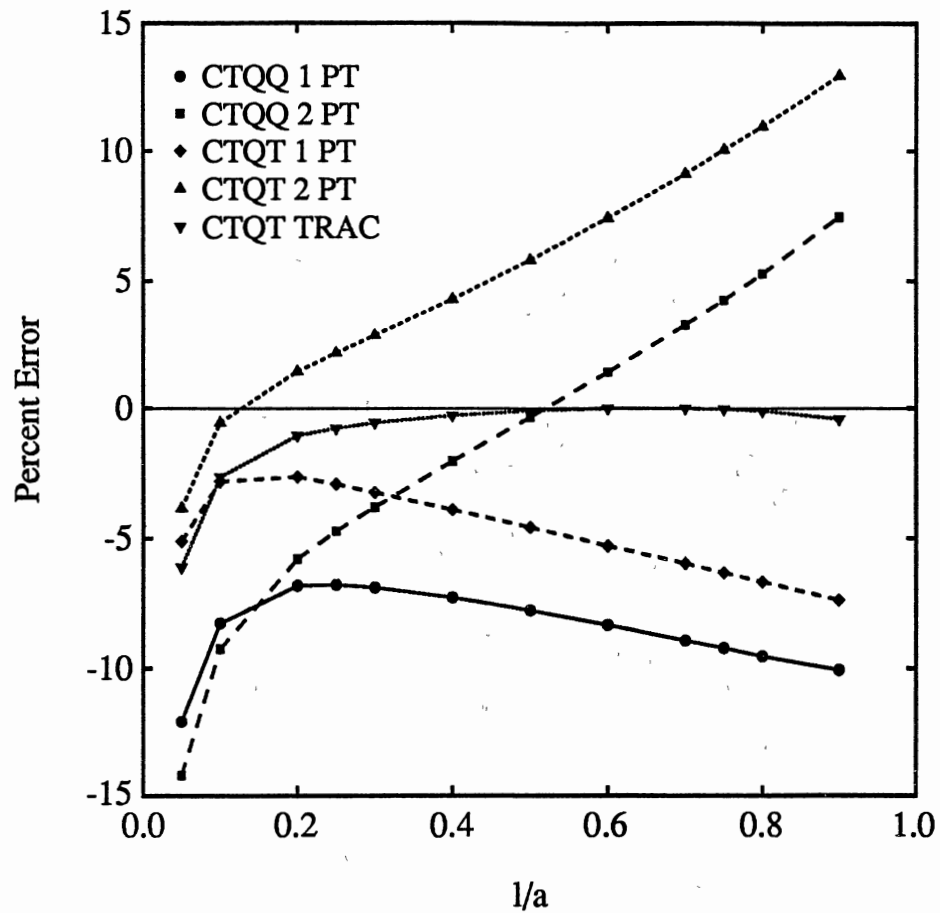


Figure 69. Percent Error in  $K_I$  for Center Cracked Plate With CTQQ and CTQT Elements

The results for the CTQUA element are plotted in Figure 70. Again, the SIF calculated by the traction method are generally less sensitive to the  $l/a$  ratio.

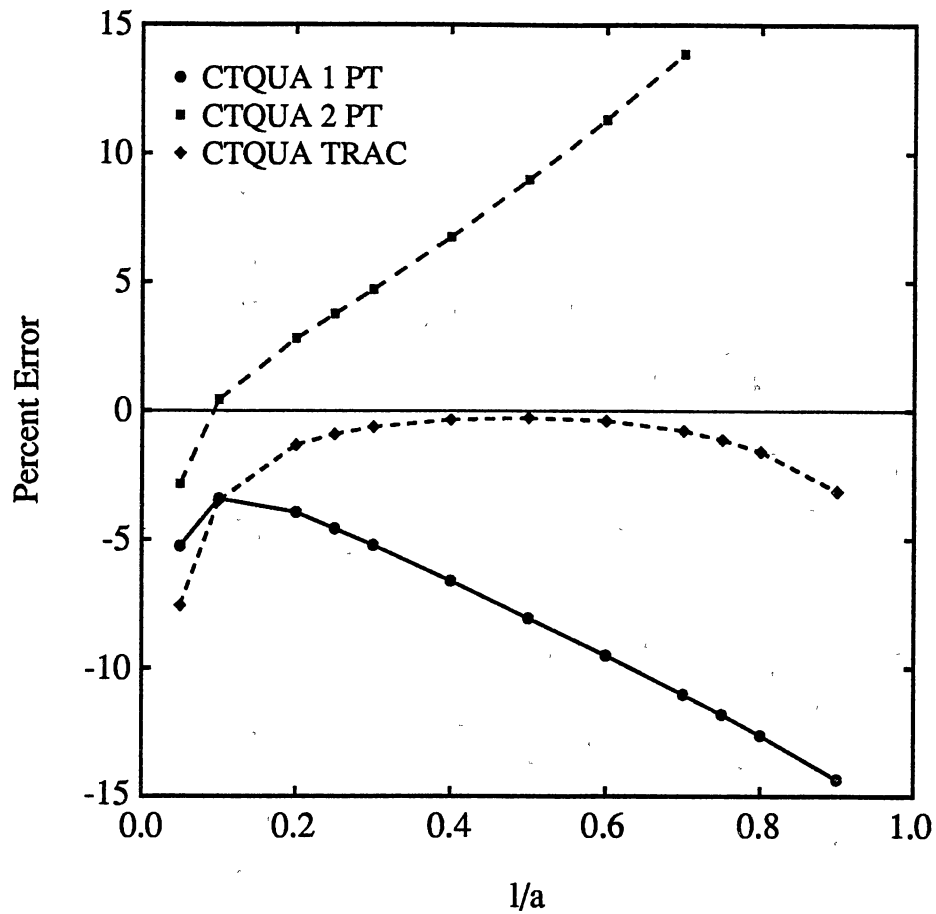


Figure 70. Percent Error in  $K_I$  for Center Cracked Plate With CTQUA Elements

The results for the CTOVR element are plotted in Figure 71. As before, the SIF for  $l/a < 0.2$  are inaccurate. This is due to the parameter in the Overhauser-type element becoming nonmonotonic when two elements that are very different in length are placed next to each other.



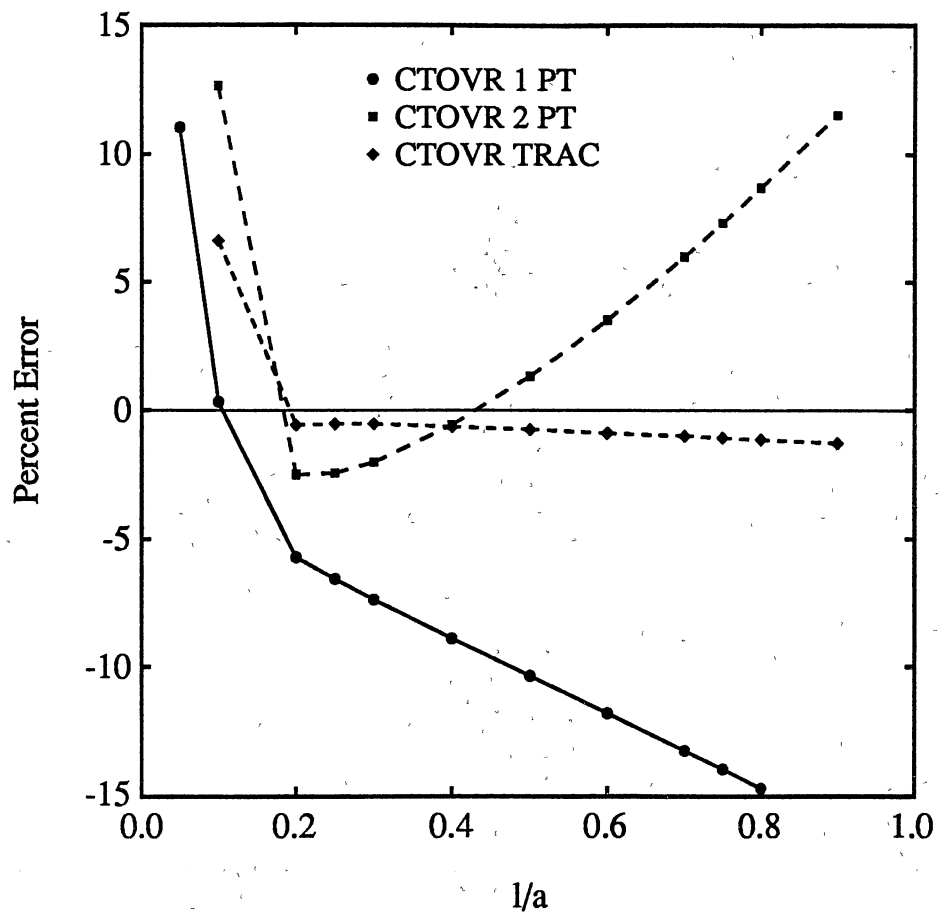


Figure 71. Percent Error in  $K_I$  for Center Cracked Plate With CTOVR Elements

For completeness, a comparison of the SIF calculated by the traction method for the CTQT, CTQUA, and CTOVR elements is given in Figure 72. As shown, for  $l/a \geq 0.2$ , the percent errors are similar; however, the CTOVR element is the least sensitive to the  $l/a$  ratio.

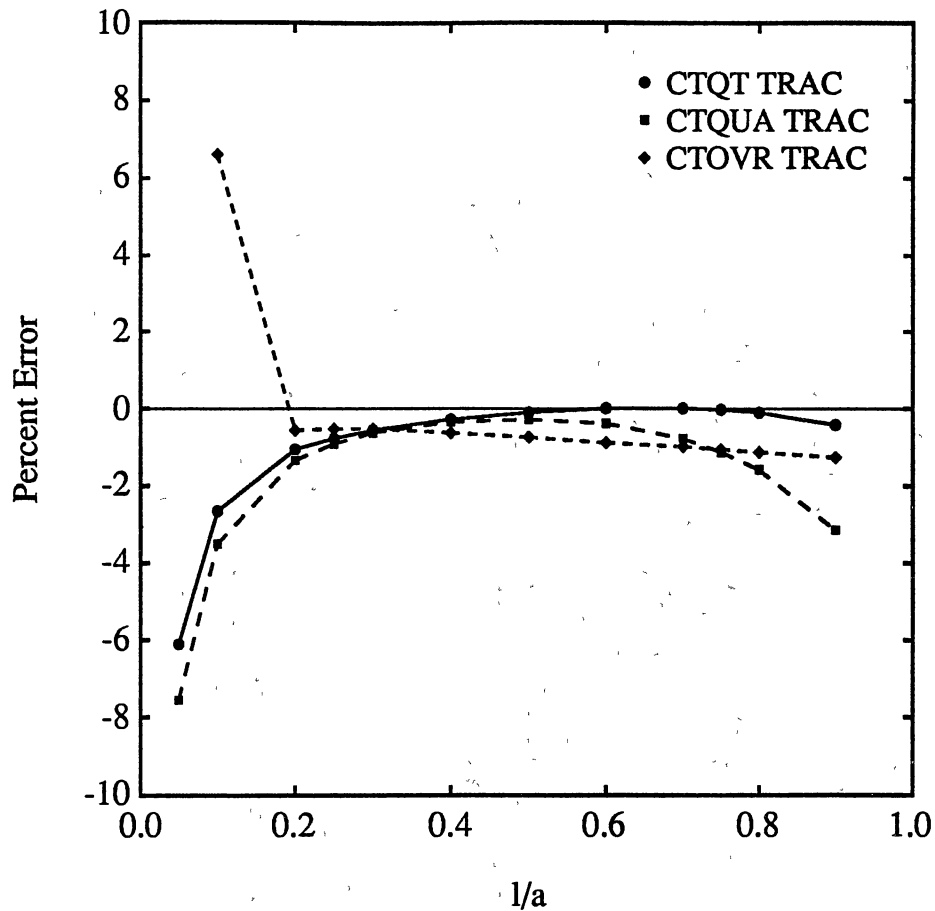


Figure 72. Comparison of Percent Errors in  $K_I$  Calculated by the Traction Method for Center Cracked Plate

### Full Model Center Cracked Plate

This example is the same as the center cracked plate, except that a full size model is made (i.e., no symmetry). The model employs Equation 37 along the interface between the regions and both crack surfaces are modeled. A comparison with results from the previous example for the CTQUA and CTOVR elements where  $l/a = 0.5$  is given in Table 2. As can be seen from the results above, the stress intensity factors

Table 2. Comparison of Selected Results between the Full and Quarter Model Center Cracked Plate

<i>Element Type</i>	<i>Full Model <math>K_I</math> ksi · in<sup>1/2</sup></i>	<i>Quarter Model <math>K_I</math> ksi · in<sup>1/2</sup></i>
CTQUA	2.826	2.822
CTOVR	2.807	2.809

for the quarter model, which uses symmetry, and the full model are very similar indicating the full model approach can be used with confidence.

### Center Slant Crack in an Infinite Domain

The center slant crack in an infinite domain under uniaxial tension was analyzed and is a mixed mode crack problem (i.e., both  $K_I$  and  $K_{II}$  will be calculated). The infinite domain was approximated by a square mesh of length  $20a$  on a side where  $a$  is the half length of the crack as shown in Figure 73. For this example  $a = 1$  in,  $\beta = \pi/4$ ,  $E = 5250$  ksi,  $\nu = 0.20$ ,  $\sigma_0 = 1$  ksi, and  $l/a = 0.5$ . Two regions were employed in the model with the crack at the center of the interface between the regions and 83 nodes. The results are compared to the analytical solution for a slanted crack in an infinite plane:

$$K_I = \sigma_0 \sqrt{\pi a} \sin^2 \beta \quad (286)$$

$$K_{II} = \sigma_0 \sqrt{\pi a} \sin \beta \cos \beta$$

where  $\beta$  is the angle between the load axis and the crack axis. There will be some small error in this model since the model is not truly infinite. A comparison of the stress intensity factors calculated with the traction approach for the CTQUA and

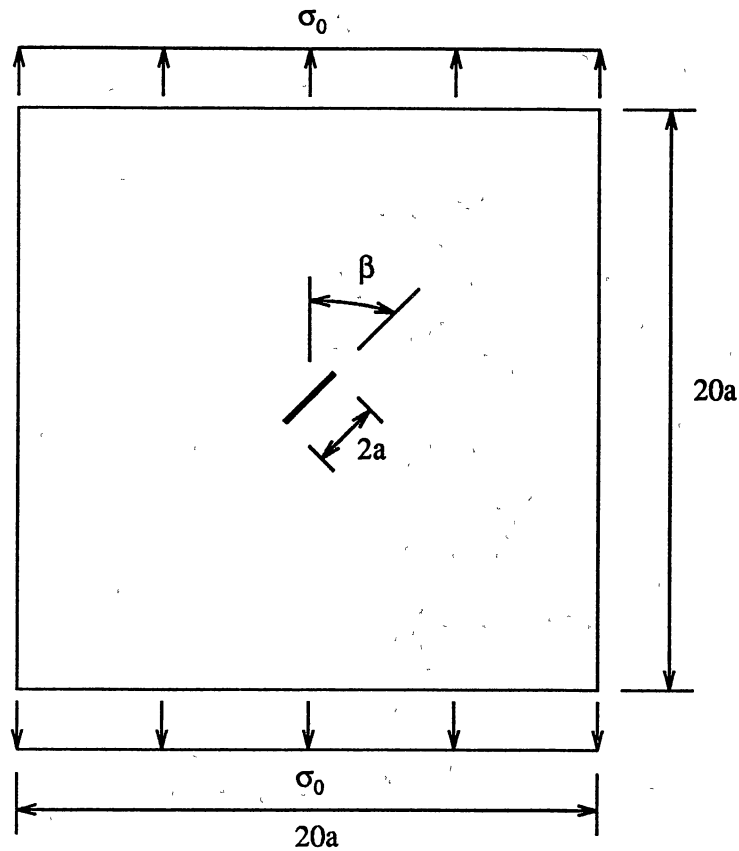


Figure 73. Center Slant Crack in an Infinite Domain

CTOVR elements with the analytical results is given in Table 3. The comparison

Table 3. Comparison of Stress Intensity Factors for the Center Slant Crack in an Infinite Domain

	$K_I$ ksi $\cdot$ in $^{1/2}$	Percent Error	$K_{II}$ ksi $\cdot$ in $^{1/2}$	Percent Error
Analytical	0.8862	—	0.8862	—
CTQUA	0.8876	0.16	0.8660	-2.28
CTOVR	0.8858	-0.04	0.8864	-2.24

shows that this approach yields fairly good results; however, the two element types performances are so close that little can be inferred from them.

## Elliptical Crack in an Infinite Region

A three dimensional example that has been employed by several boundary element researchers [44,36] is the flat elliptical crack in an infinite region under a uniform normal stress at infinity as shown in Figure 74. The infinite region may be divided into a forespace and a backspace using the crack face as a dividing plane. A close up

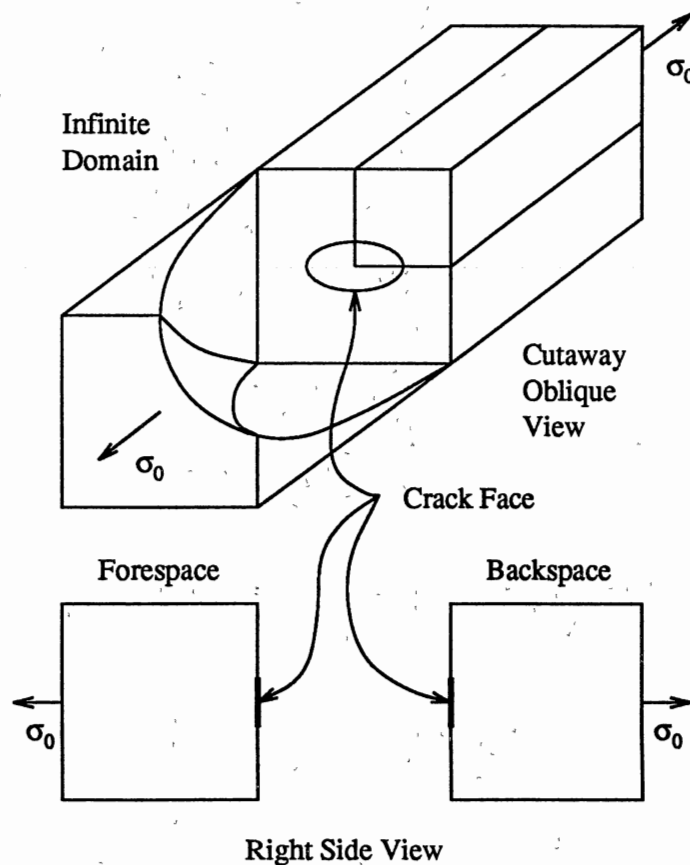


Figure 74. Elliptical Crack in an Infinite Region

of the crack face is shown in Figure 75 where the ratio of the major axis to the minor axis of the ellipse is  $a/b = 2/1$ .

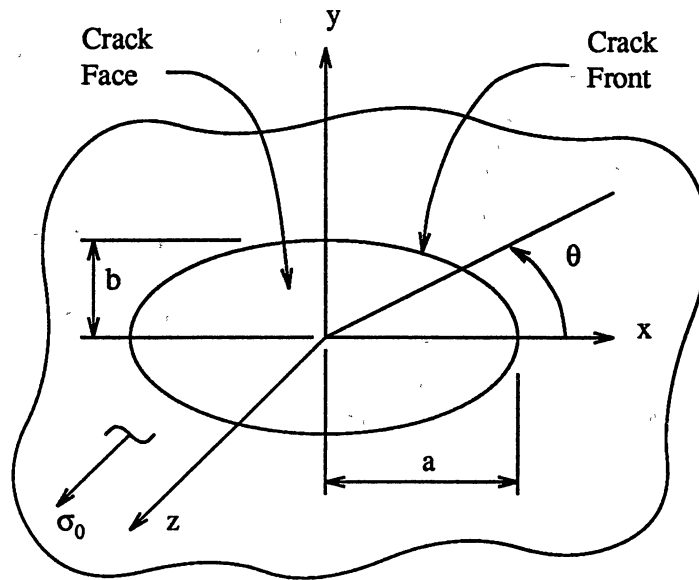


Figure 75. Crack Face Close Up for the Elliptical Crack in an Infinite Region

The crack was modeled with a large finite dimension elliptical cylinder approximating the backspace of the infinite region and the crack itself. Two views of the boundary element mesh are shown in Figures 76 and 77. Only an eighth of the cylinder needs to be modeled because of symmetry and has dimensions of  $7.81b \times 8b \times 40b$ . The large finite size of the cylinder was chosen to minimize the effects of the finite size. The dimension, material properties, and loads of the model are  $a = 2$  in,  $b = 1$  in,  $E = 5250$  ksi,  $\nu = 0.20$ , and  $\sigma_0 = 1$  ksi.

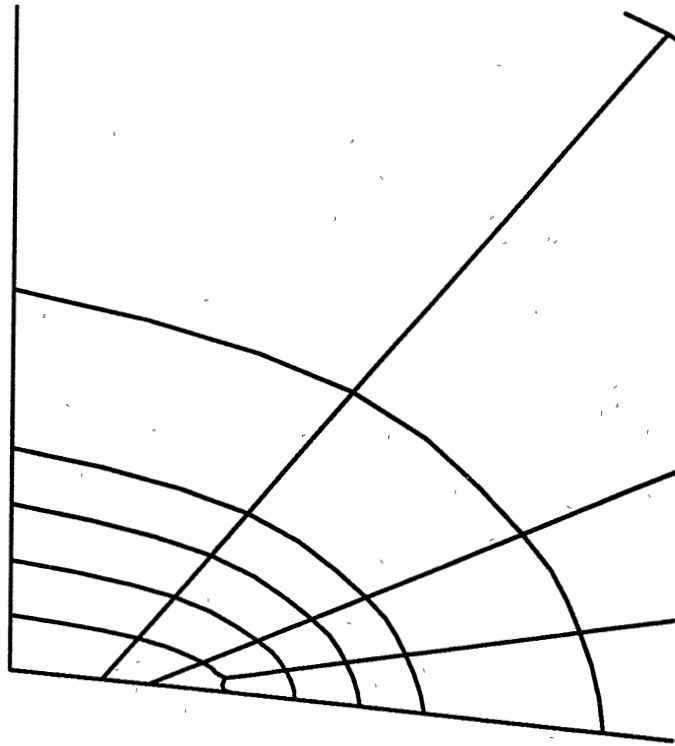


Figure 76. Elliptical Crack BEM Mesh

The analytical solution of this problem was first reported in [38] and is given by

$$K_I = \frac{\sigma\sqrt{\pi b}}{E(m)} \left( \sin^2 \theta + \frac{b^2}{a^2} \cos^2 \theta \right)^{\frac{1}{4}} \quad (287)$$

where  $E(m)$  is the elliptic integral of the second kind

$$m = k^2 = 1 - \frac{b^2}{a^2} \quad (288)$$

$$E(m) = \int_0^{\frac{\pi}{2}} (1 - k^2 \sin^2 \theta)^{\frac{1}{2}} d\theta$$

The percent error in the boundary element solution was calculated by Equation 285.

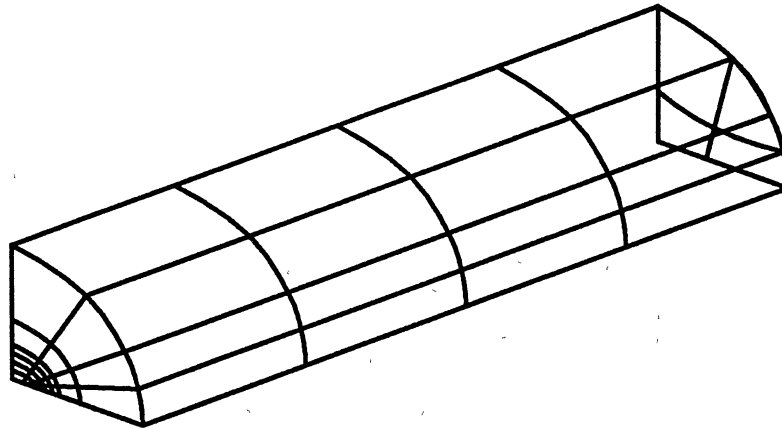


Figure 77. Elliptical Crack Overall BEM Mesh

The results for the three dimensional Overhauser crack tip elements are compared to those given in Reference [44] for a quadratic crack tip boundary element in Figure 78 for various values of the elliptic angle  $\theta$ . As shown in the figure, the Overhauser crack tip elements gave slightly better and more consistent results.

### Compact Tension Specimen

Another common problem is the standard compact tension specimen as specified in ASTM E399-83 [26]. It is depicted in Figure 79. The simplified boundary element model shown in Figure 80 is similar to ones employed in References [43,68]. The effect of the pin holes was disregarded (i.e., the model is sectioned through the centerline of the holes) and a parabolic shear equivalent to the applied force  $P$  was applied to the end faces of the solid model. Symmetry is employed in two directions, explicitly in the  $z$  direction and implicitly in the  $x$  direction by reflecting through the  $y - z$



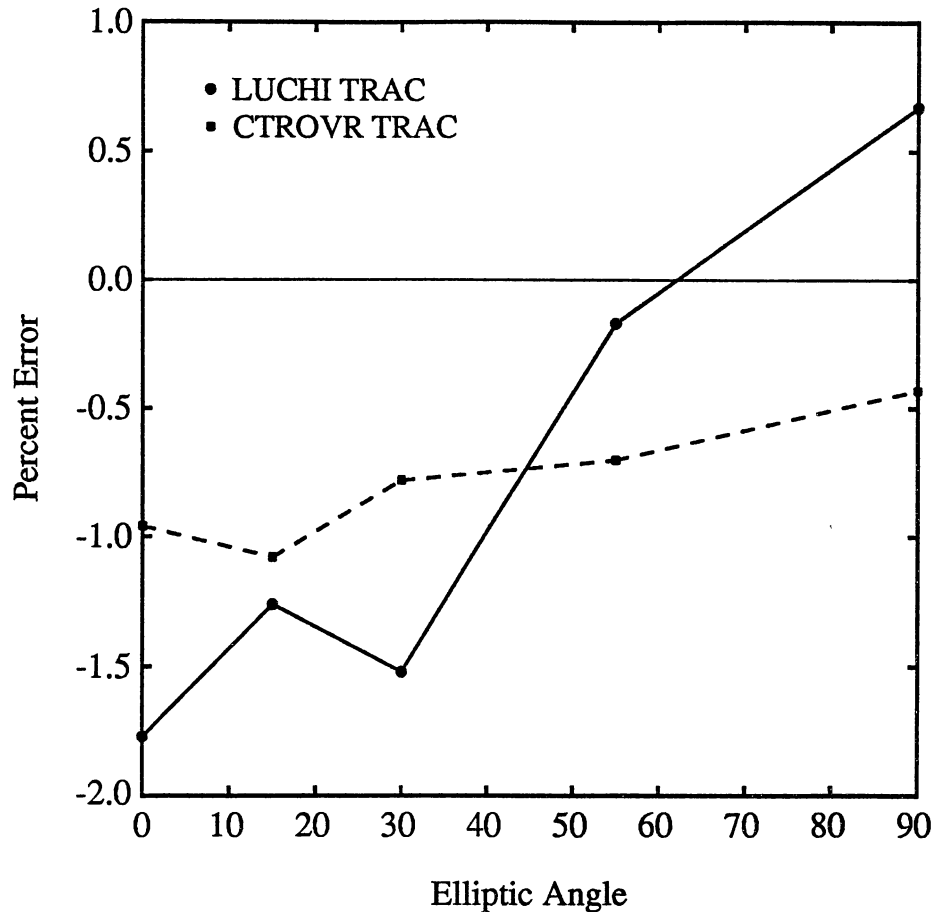


Figure 78. Percent Error in  $K_I$  for the Elliptical Crack in an Infinite Region

plane, yielding a model that is one-quarter of the original specimen. The model's dimensions and material properties are  $a = 1$  in,  $W = 2$  in,  $E = 1$  ksi,  $P = 1$  klf, and  $\nu = 0.30$ .

The boundary element mesh, shown in Figure 81, is composed of both RQUA elements and Overhauser type elements (ROVRC, CTROVRC, and CTROVRCV). It contains a total of 118 nodes and 32 elements.

The problem was run with two sets of boundary conditions, one to simulate plane

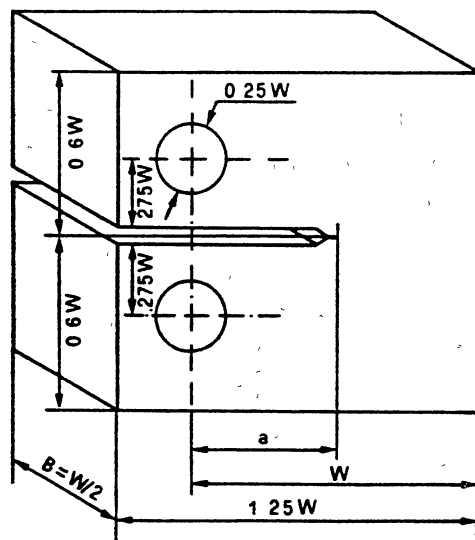


Figure 79. Standard Compact Tension Specimen (after Luchi and Rizzuti, 1987)

strain conditions and the other a full three dimensional problem. The plain strain strain conditions were simulated by constraining the  $x$  direction at  $x = B/2$ . The results may now be compared to the ASTM values as calculated by the formula given in References [57,26].

$$K_I = \frac{P}{B\sqrt{W}} \frac{(2 + \alpha)(0.866 + 4.64\alpha - 13.32\alpha^2 + 14.72\alpha^3 - 5.6\alpha^4)}{(1 - \alpha)^{3/2}} \quad (289)$$

where

$$0.2 \leq \alpha = \frac{a}{W} \leq 1.0 \quad (290)$$

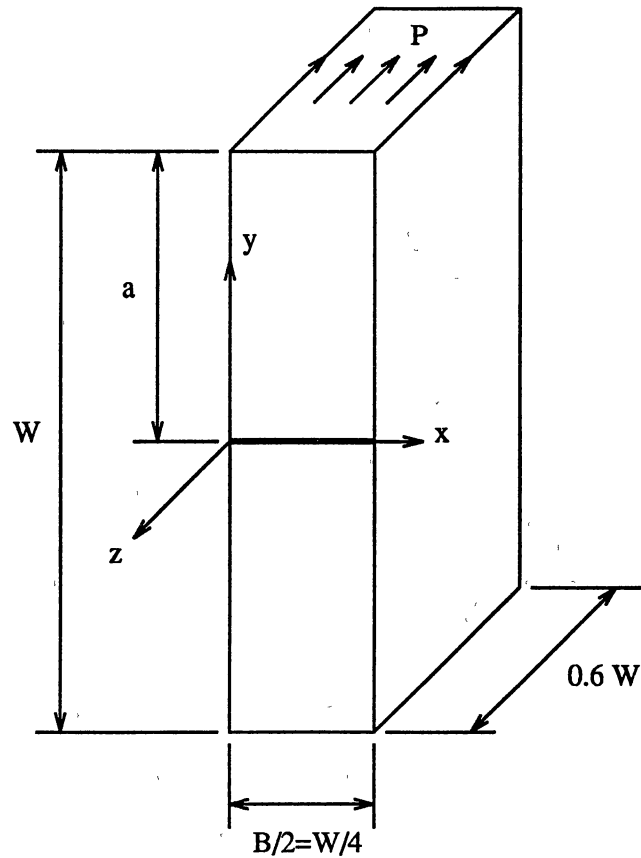


Figure 80. Compact Tension Specimen Model

A comparison of the boundary element results and ASTM values are given in Table 4. As can be seen, the smallest percent error, 0.04, is at  $x = 0$  and increases to a maximum of 0.63 at the free surface. This increase in error is consistent with the results given in Reference [43].

The full three dimensional problem was modeled with the same boundary element mesh, but the boundary condition at  $x = B/2$  was changed to a free surface. The CTROVR results are compared in Figure 82 to the ASTM plane strain formula, boundary element values in Reference [43], and finite element values in Reference

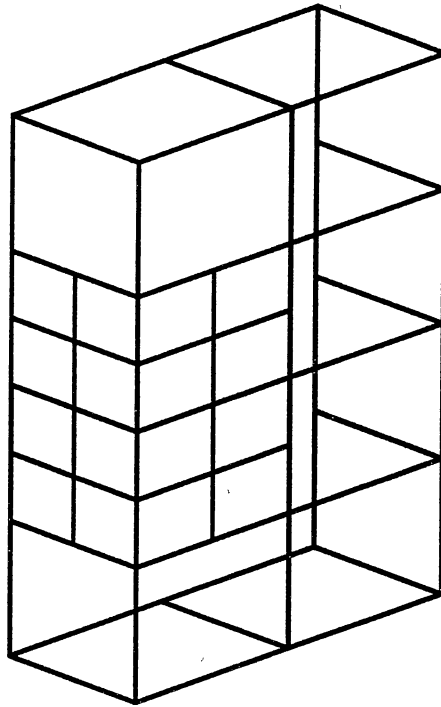


Figure 81. Compact Tension Specimen BEM Mesh

Table 4. Compact Tension Specimen SIF Comparison With the Plane Strain Value of  $K_I = 6.73 \text{ ksi} \cdot \text{in}^{1/2}$

$2x/B$	$K_I \text{ ksi} \cdot \text{in}^{1/2}$	<i>Percent Error</i>
0.0	6.73280	0.04
0.5	6.71776	-0.18
1.0	6.77291	0.63

[68] and are quite similar.

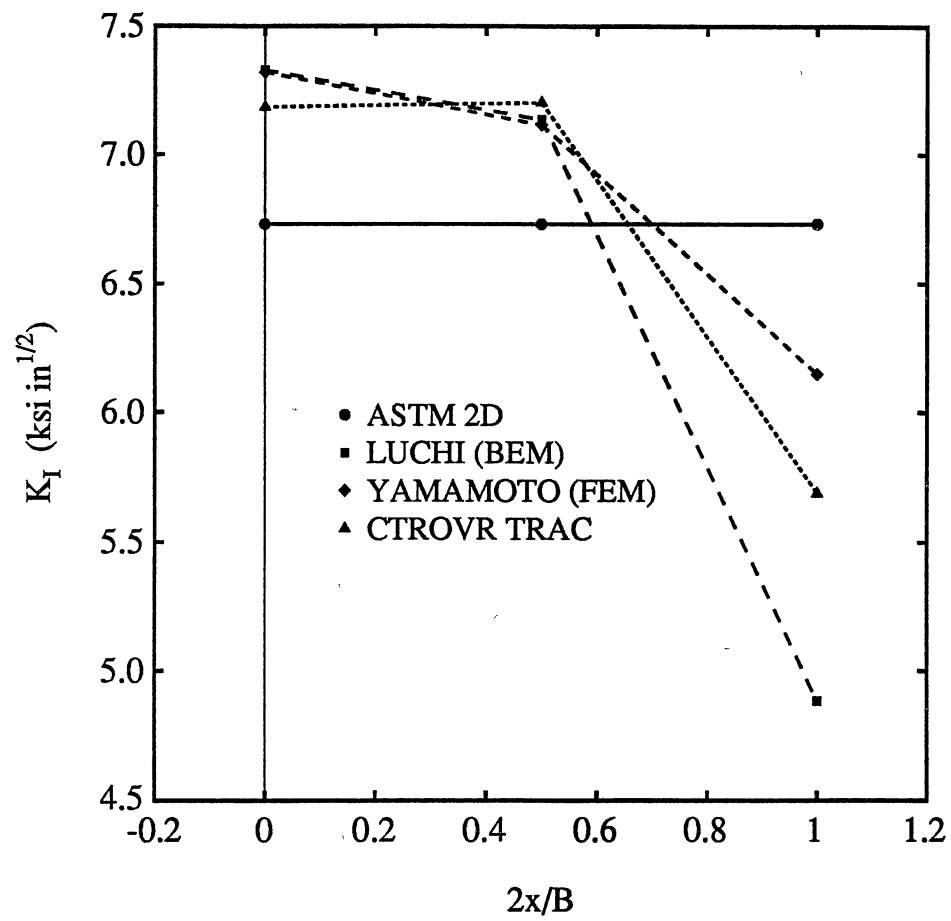


Figure 82. Compact Tension Specimen SIF Variation Along the Crack Front

## Chapter IX

### CONCLUSIONS

Numerical methods, such as the finite element method and the boundary element method, are more convenient in many cases to the various theoretical techniques for the solution of linear elastic fracture mechanics problems with arbitrary geometries and loading conditions. Boundary element methods have some practical and theoretical advantages over finite element methods for linear elastic fracture mechanics problems. One is that only the boundary must be modeled as opposed to the entire domain, i.e., a three dimensional problem may be modeled by a surface and a two dimensional problem by a curve. Another is that the stresses are typically modeled with a lower order polynomial than the displacements, while the boundary element method typically models displacements and tractions with the same order polynomial. Since stress intensity factors may be derived directly from stresses and the boundary element method directly solves for tractions, a more direct link between the problem solution and the stress intensity factors is obtained. A disadvantage of the boundary element method when compared to the finite element method is that the mathematics for describing and implementing the boundary element method are more complex.

The objective of this work was to better represent the geometry of a crack through

the use of  $C^1$  continuous elements in both two and three dimensions and thus enhance the accuracy of the boundary element method in the solution of linear elastic fracture mechanics problems. Since the Overhauser crack tip elements overlap and are  $C^1$  continuous, much of the previous work done in implementing Lagrangian type elements in the boundary element method this area was of little use. The innovations done in support of the objective are listed below.

- The two dimensional crack tip Overhauser elements
- Methods for performing the singular integrations for the two dimensional crack tip Overhauser elements
- A general approach for derivation of stress intensity factors from two dimensional boundary elements that properly model the  $1/\sqrt{r}$  behavior of the tractions
- The use of Coons type surfaces in the derivation of all the three dimensional rectangular element types
- The three dimensional Overhauser elements
- A general transformation approach for performing the three dimensional singular integrations
- The three dimensional crack tip Overhauser elements
- A general transformation approach for performing the three dimensional crack tip singular integrations

The superiority of employing stress intensity factors derived from tractions as opposed to those derived from displacements was demonstrated in the two dimensional examples. In particular, the traction stress intensity factors were much less sensitive to the ratio of the length of the crack tip element to the length of the crack.

The Overhauser-type crack tip elements were more generally accurate than the other element types for the two and three dimensional examples examined. The two dimensional Overhauser crack tip element showed a nearly complete insensitivity to the ratio of the length of the crack tip element to the length of the crack except for extremely small values where the parameter became nonmonotonic. It is believed the more accurate results of the Overhauser crack tip elements are a result of both the  $C^1$  continuity and a better modeling of the near field crack tip stresses. However, percentage errors for all boundary elements that properly model the tractions are fairly close, indicating that the quadratic behavior of these shape functions may be the dominant factor. While all of the Overhauser elements give excellent results, they have a small disadvantage in that the meshes are slightly more difficult to assemble by hand.

The significance of this work lies not only in the fact that the Overhauser elements generally modeled the problems examined more accurately and with a nearly complete insensitivity to the ratio of the length of the crack tip element to the length of the crack, but that the approach taken will make derivation and implementation of new crack tip boundary elements easier. Specifically, the Coons approach to derivation of surface elements and the general transformation approach for performing the three



dimensional singular integrations for standard and crack tip elements are meaningful advances in boundary elements in general and as applied to linear elastic fracture mechanics in particular.

The results of the current study indicate the need for a cubic crack tip boundary element and the proper transformations to find the stress intensity factors for nonflat three dimensional crack tip boundary elements.

## BIBLIOGRAPHY

- [1] M. H. Aliabadi. An enhanced boundary element method for determining fracture parameters. In T. A. Cruse, editor, *Numerical Methods in Fracture Mechanics, Proceedings of the 4th International Conference, San Antonio, Texas, 27-39*. Pineridge Press, 1987.
- [2] P. K. Banerjee and R. Butterfield. *The Boundary Element Method in Engineering Science*. McGraw-Hill, New York, 1981.
- [3] Leslie Banks-Sills. Quarter-Point Singular Elements Revisited. *International Journal of Fracture*, 34:R63-R69, 1987.
- [4] Leslie Banks-Sills and Yaacov Bortman. Reappraisal of the Quarter-Point Quadrilateral Element in Linear Elastic Fracture Mechanics. *International Journal of Fracture*, 25:169-180, 1984.
- [5] Robert E. Barnhill. Representation and Approximation of Surfaces. In John R. Rice, editor, *Mathematical Software III*, 69-120, New York, 1977. Academic Press.
- [6] R. S. Barsoum. On the use of Isoparametric Finite Elements in Linear Fracture Mechanics. *International Journal for Numerical Methods in Engineering*, 10:25-37, 1976.
- [7] P. Bezier. Mathematical and Practical Possibilities of UNISURF. In R. E. Barnhill and R. F. Riesenfeld, editors, *Computer Aided Geometric Design*, 127-152. Academic Press, 1974.
- [8] G. E. Blandford, A. R. Ingraffea, and J. A. Liggett. Two-Dimensional Stress Intensity Factor Computations Using the Boundary Element Method. *International Journal for Numerical Methods in Engineering*, 17:387-404, 1981.
- [9] O. L. Bowie. Rectangular Tensile Sheet with Symmetric Edge Cracks. *ASME Journal of Applied Mechanics*, 31:208-212, 1964.
- [10] C. A. Brebbia and J. Dominguez. *Boundary Elements An Introductory Course*. Computational Mechanics Publications and McGraw-Hill, Southampton and New York, 1989.

- [11] C. A. Brebbia, J. C. F. Telles, and L. C. Wrobel. *Boundary Element Techniques, Theory and Application in Engineering*. Springer-Verlag, Berlin, 1984.
- [12] J. A. Brewer and D. C. Anderson. Visual Interaction with Overhauser Curves and Surfaces. *Computer Graphics*, 11(2):132–137, 1977.
- [13] B. Budiansky and J. R. Rice. Conservation Laws and Energy-Release Rates. *ASME Journal of Applied Mechanics*, 40:201–203, 1973.
- [14] H. F. Bueckner. A novel principle for the computation of stress intensity factors. *Z Angewandte Mathemat. Mechan.*, 50:529–426, 1970.
- [15] S. K. Chan, I. S. Tuba, and W. K. Wilson. On the Finite Element Method in Linear Fracture Mechanics. *Engineering Fracture Mechanics*, 2:1–17, 1970.
- [16] S. A. Coons. *Surfaces for Computer-Aided Design of Space Forms*. MIT Project MAC-TR-41, 1967.
- [17] S. L. Crouch. Solution of Plane Elasticity Problems by the Displacement Discontinuity Method. *International Journal for Numerical Methods in Engineering*, 10:301–343, 1976.
- [18] T. A. Cruse. Application of the Boundary-Integral Equation Method to Three-Dimensional Stress Analysis. *Computers and Structures*, 3:509–527, 1973.
- [19] T. A. Cruse. Mathematical Foundations of the Boundary Integral Equation Methods in Solid Mechanics. Technical Report AFOSR-TR-77-1002, Pratt and Whitney, July 1977. Contract F44620-74-C-0060 NTIS AD-A043-114.
- [20] T. A. Cruse. Two-Dimensional Fracture Mechanics Analysis. *Applied Mathematical Modelling*, 2:287–293, 1978.
- [21] T. A. Cruse. Fracture Mechanics. In D. E. Beskos, editor, *Boundary Element Methods in Mechanics*, 334–365. Elsevier Science Publishers, 1987.
- [22] T. A. Cruse. *Boundary Element Analysis in Computational Fracture Mechanics*. Kluwer Academic Publishers, 101 Philip Drive, Norwell, MA 02061, 1988.
- [23] T. A. Cruse and G. J. Meyers. Three-Dimensional Fracture Mechanics Analysis. *ASCE Journal of the Structural Division*, 103(ST2):309–320, 1977.
- [24] T. A. Cruse and W. Vanburen. Three-Dimensional Elastic Stress Analysis of a Fracture Specimen with an Edge Crack. *International Journal of Fracture Mechanics*, 7:1–15, 1971.
- [25] T. A. Cruse and R. B. Wilson. Boundary Integral Equation Methods for Elastic Fracture Mechanics Analysis - Final Report. Technical Report AFOSR-TR-0355, Pratt and Whitney, November 1977. Contract F44620-74-C-0060 NTIS AD-A051-992.

- [26] ASTM E399-83. Standard Test Method for Plane-Strain Fracture Toughness of Metallic Materials. *Annual Book of ASTM Standards*, 02.02:779–814, 1983.
- [27] N. Fares and V. C. Li. An Indirect Boundary Element Method for 2D Finite/Infinite Regions with Multiple Displacement Discontinuities. *Engineering Fracture Mechanics*, 26:127–141, 1987.
- [28] I. E. Faux and M. J. Pratt. *Computational Geometry for Design and Manufacture*. Ellis Horwood, Chichester, 1979.
- [29] Maria S. Gomez-Lera and Enrique Alarcón. Elastostatics. In Dimitri E. Beskos, editor, *Boundary Element Methods in Mechanics*, 107–189. Elsevier Science Publishers, Amsterdam, The Netherlands, 1987.
- [30] R. D. Henshell and K. G. Shaw. Crack Tip Finite Elements are Unnecessary. *International Journal for Numerical Methods in Engineering*, 9:495–507, 1975.
- [31] H. D. Hibbitt. Some Properties of Singular Isoparametric Elements. *International Journal for Numerical Methods in Engineering*, 11:180–184, 1977.
- [32] Terence T. Hibbs.  $C^1$  Continuous Representations and Advanced Singular Kernel Integrations in the Three Dimensional Boundary Element Method. PhD thesis, Teesside Polytechnic, Middlesbrough, Cleveland UK, 1988.
- [33] M. A. Hussain, J. D. Vasilakis, and S. L. Pu. Quadratic and Cubic Transition Elements. *International Journal for Numerical Methods in Engineering*, 17:1397–1406, 1981.
- [34] G. R. Irwin. Fracture. In *Handbook der Physik*, 551–590. Springer-Verlag, 1958.
- [35] Z. H. Jia, D. J. Shippy, and F. J. Rizzo. On the Computation of Two-Dimensional Stress Intensity Factors Using the Boundary Element Method. *International Journal for Numerical Methods in Engineering*, 26:2739–2753, 1988.
- [36] Z. H. Jia, D. J. Shippy, and F. J. Rizzo. Three-Dimensional Crack Analysis Using Singular Boundary Elements. *International Journal for Numerical Methods in Engineering*, 28:2257–2273, 1989.
- [37] Melvin F. Kanninen and Carl H. Popelar. *Advanced Fracture Mechanics*. Oxford University Press, New York, 1985. 620.1126 K16a.
- [38] M. K. Kassir and G. C. Sih. Three-Dimensional Stress Distribution Around an Elliptic Crack Under Arbitrary Loadings. *ASME Journal of Applied Mechanics*, 33:601–611, 1966.
- [39] K. Kishitani, T. Hirai, and K. Murakami. J Integral Calculations with Boundary Elements. In C. A. Brebbia, T. Futagami, and M. Tanaka, editors, *Boundary Elements, Proceedings of the Fifth International Conference, Hiroshima, Japan*,

- November, 1983, 481–493. Computational Mechanics Publications and Springer-Verlag, 1983.
- [40] J. K. Knowles and E. Sternberg. On a Class of Conservation Laws in Linearized and Finite Elastostatics. *Archive for Rational Mechanics and Analysis*, 44:187–211, 1972.
- [41] Donald E. Knuth. *The Art of Computer Programming, Vol. 2, Seminumerical Algorithms, 2nd Ed.* Addison-Wesley, Reading, MA, 1981.
- [42] M. L. Luchi and A. Poggialini. Computation of 3-Dimensional Stress Intensity Factors Using Special Boundary Elements. In C. A. Brebbia, T. Futagami, and M. Tanaka, editors, *Boundary Elements*, 461–470, Boston and Berlin, 1983. Computational Mechanics Publications and Springer-Verlag.
- [43] M. Laura Luchi and Sergio Rizzuti. Boundary Element Analysis of CT Specimens with Straight and Curved Crack Fronts. *International Journal of Fracture*, 34:23–40, 1987.
- [44] M. Laura Luchi and Sergio Rizzuti. Boundary Elements for Three-Dimensional Elastic Crack Analysis. *International Journal for Numerical Methods in Engineering*, 24:2253–2271, 1987.
- [45] P. P. Lynn and A. R. Ingraffea. Transition Elements to be Used with Quarter-Point Crack-Tip Elements. *International Journal for Numerical Methods in Engineering*, 12:1031–1036, 1978.
- [46] José Martínez and José Domínguez. Short Communication on the Use of Quarter-Point Boundary Elements for Stress Intensity Factor Computations. *International Journal for Numerical Methods in Engineering*, 20:1941–1950, 1984.
- [47] J. C. Mason and R. N. L. Smith. Boundary Integral Equation Methods for a Variety of Curved Crack Problems. In Christopher T. H. Baker and Geoffrey F. Miller, editors, *Treatment of Integral Equations by Numerical Methods*, 239–252, New York, 1982. Academic Press.
- [48] H. Mews. Calculation of Stress Intensity Factors for Various Crack Problems with the Boundary Element Method. In C. A. Brebbia, W. L. Wendland, and G. Kuhn, editors, *Boundary Elements IX, Volume 2: Stress Analysis Applications*, 259–278, Boston and Berlin, 1987. Computational Mechanics Publications and Springer-Verlag.
- [49] S. Mukherjee. *Boundary Element Methods in Creep and Fracture*. Applied Science Publishers, London, 1982.
- [50] V. Murti and S. Valliappan. A Universal Optimum Quarter Point Element. *Engineering Fracture Mechanics*, 25:237–258, 1986.

- [51] A. W. Overhauser. Analytic Definition of Curves and Surfaces by Parabolic Blending. Technical Report SL68-40, Scientific Research Staff Publication, Ford Motor Company, May 1968.
- [52] P. M. Prenter. *Splines and Variational Methods*. John Wiley and Sons, New York, 1975.
- [53] J. R. Rice. A Path Independent Integral and the Approximate Analysis of Strain Concentration by Notches and Cracks. *ASME Journal of Applied Mechanics*, 35:379–386, 1968.
- [54] C. F. Shih, H. G. deLorenzi, and M. D. German. Crack Extension Modeling with Singular Quadratic Isoparametric Elements. *International Journal of Fracture*, 12(4):647–651, 1976.
- [55] R. N. L. Smith. From Rags to Riches? - Developments in the BEM for the Solution of Elastic Fracture Problems. In C. A. Brebbia, editor, *Boundary Elements X, Vol. 3: Stress Analysis*, 155–176, Boston and Berlin, 1988. Computational Mechanics Publications and Springer-Verlag.
- [56] M. D. Snyder and T. A. Cruse. Boundary-integral equation analysis of cracked anisotropic plates. *International Journal of Fracture*, 11(2):315–328, 1975.
- [57] John E. Srawley. Wide Range Stress Intensity Factor Expressions for ASTM E 399 Standard Fracture Toughness Specimens. *International Journal of Fracture*, 12:475–476, 1977.
- [58] A. H. Stroud and D. Secrest. *Gaussian Quadrature Formulae*. Prentice-Hall, Englewood Cliffs, NJ, 1966.
- [59] Ukhwan Sur and Nicholas J. Altiero. An Alternative Integral Equation Approach for Curved and Kinked Cracks. *International Journal of Fracture*, 38:25–41, 1988.
- [60] G. T. Symm. Treatment of Singularities in the Solution of Laplace's Equation by an Integral Equation Method. Technical report, National Physical Laboratory, UK, January 1973.
- [61] C. L. Tan and R. T. Fenner. Elastic Fracture Mechanics Analysis by the Boundary Integral Equation Method. *Proceedings of the Royal Society of London*, A369:243–260, 1979.
- [62] Frank van der Ween. Mixed Mode Fracture Analysis of Rectilinear Anisotropic Plates Using Singular Boundary Elements. *Computers and Structures*, 17(4):469–474, 1983.
- [63] H. G. Walters. Techniques for Boundary Element Analysis in Elastostatic Influenced by Geometric Modeling. Master's thesis, Louisiana State University, Baton Rouge, Louisiana, 1986.

- [64] H. G. Walters, J. C. Ortiz, G. S. Gipson, and J. A. Brewer III. Overhauser Boundary Elements in Potential Theory and Linear Elastostatics. In T. A. Cruse, editor, *Advanced Boundary Element Methods*, 459–464, New York, 1987. Springer-Verlag.
- [65] J. O. Watson. Hermitian Cubic Boundary Elements for Plane Problems of Fracture Mechanics. *Res Mechanica*, 4:23–42, 1982.
- [66] J. O. Watson. Hermitian Cubic and Singular Elements for Plane Strain. In P. K. Banerjee and J. O. Watson, editors, *Developments in Boundary Element Methods 4*, 1–28. Elsevier Applied Science Publishers, London, 1984.
- [67] M. L. Williams. On the Stress Distribution at the Base of a Stationary Crack. *ASME Journal of Applied Mechanics*, 24:109–114, 1957.
- [68] Yoshiyuki Yamamoto and Yoichi Sumi. Stress Intensity Factors for Three-Dimensional Cracks. *International Journal of Fracture*, 14:17–35, 1978.
- [69] Lung-An Ying. A Note on the Singularity and the Strain Energy of Singular Elements. *International Journal for Numerical Methods in Engineering*, 18:31–39, 1982.
- [70] O. C. Zienkiewicz. *The Finite Element Method, Third Ed.* McGraw-Hill, New York, 1977.

2  
VITA

Harold Grayson Walters

Candidate for the Degree of

Doctor of Philosophy

Title: PARAMETRIC CONTINUOUS CRACK TIP BOUNDARY ELEMENTS IN  
LINEAR ELASTIC FRACTURE MECHANICS

Major Field: Civil Engineering

Biographical:

Personal Data: Born in Phoenix, Arizona, July 7, 1962, the son of Harold L. And Pat A. Walters. Married Leigh Pennington Beaulieu in Freeport, Maine, on August 2, 1986.

Education: Graduated for South Natchez Adams High School, Natchez, Mississippi, in May, 1980; received the Bachelor of Science Degree in Mechanical Engineering from Louisiana State University at Baton Rouge in December, 1984; received the Master of Science Degree in Mechanical Engineering from Louisiana State University at Baton Rouge in August, 1986; completed requirements for the Doctor of Philosophy degree at Oklahoma State University in May, 1990.

Experience: Salesman of educational and religious books for Thomas Nelson Publishers at Nashville, Tennessee, from May, 1981, to August, 1981. Supervised nondestructive testing, performed vibration analysis of rotating equipment, performed component redesign, and implemented a vibration analysis computer program for International Paper Company at Natchez, Mississippi at various times from August, 1982, to August, 1985. Instructor for machine design laboratory for Louisiana State University at Baton Rouge, Louisiana from December, 1984 to August, 1986. Instructor, coordinator, and teaching assistant for elementary dynamics lecture and recitation for Oklahoma State University at Stillwater, Oklahoma, from August, 1986 to May, 1990.



Affiliations: ASME, NSPE, OSPE, ACM, Pi Tau Sigma, Tau Beta Pi,  
ACACIA

Honors: National Merit Scholar